Volume 53
Number 6
21 March 2024
Pages 2763–3208

Chem Soc Rev

Chemical Society Reviews

rsc.li/chem-soc-rev

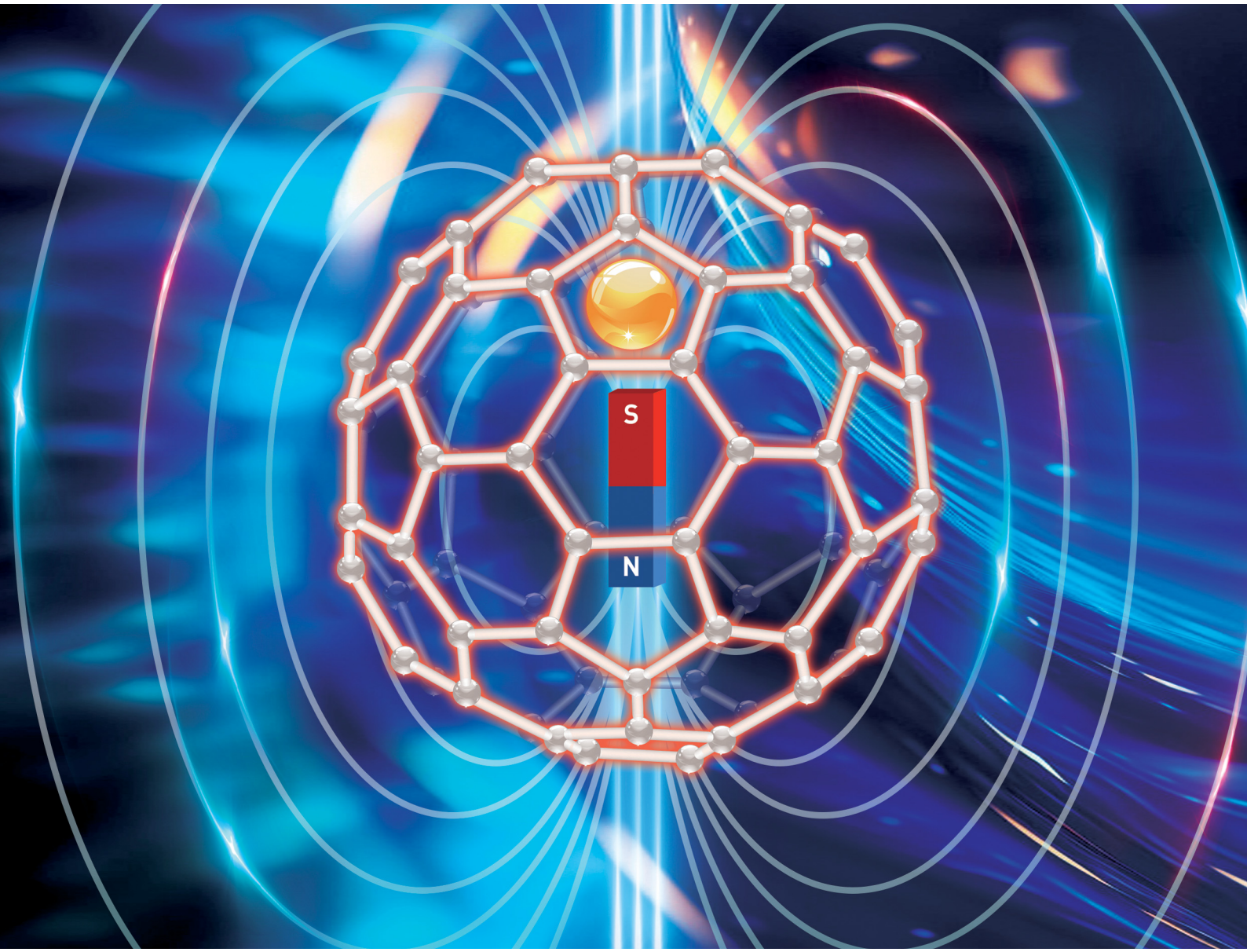

ISSN 0306-0012

ROYAL SOCIETY OF CHEMISTRY

REVIEW ARTICLE
Ziqi Hu and Shangfeng Yang
Endohedral metallofullerene molecular nanomagnets

Chem Soc Rev

REVIEW ARTICLE

View Article Online
View Journal | View Issue

Cite this: *Chem. Soc. Rev.*, 2024, **53**, 2863

Endohedral metallofullerene molecular nanomagnets

Ziqi Hu * and Shangfeng Yang *

Magnetic lanthanide (Ln) metal complexes exhibiting magnetic bistability can behave as molecular nanomagnets, also known as single-molecule magnets (SMMs), suitable for storing magnetic information at the molecular level, thus attracting extensive interest in the quest for high-density information storage and quantum information technologies. Upon encapsulating Ln ion(s) into fullerene cages, endohedral metallofullerenes (EMFs) have been proven as a promising and versatile platform to realize chemically robust SMMs, in which the magnetic properties are able to be readily tailored by altering the configurations of the encapsulated species and the host cages. In this review, we present critical discussions on the molecular structures and magnetic characterizations of EMF-SMMs, with the focus on their peculiar molecular and electronic structures and on the intriguing molecular magnetism arising from such structural uniqueness. In this context, different families of magnetic EMFs are summarized, including mononuclear EMF-SMMs wherein single-ion anisotropy is decisive, dinuclear clusterfullerenes whose magnetism is governed by intramolecular magnetic interaction, and radical-bridged dimetallic EMFs with high-spin ground states that arise from the strong ferromagnetic coupling. We then discuss how molecular assemblies of SMMs can be constructed, in a way that the original SMM behavior is either retained or altered in a controlled manner, thanks to the chemical robustness of EMFs. Finally, on the basis of understanding the structure–magnetic property correlation, we propose design strategies for high-performance EMF-SMMs by engineering ligand fields, electronic structures, magnetic interactions, and molecular vibrations that can couple to the spin states.

Received 13th November 2023

DOI: 10.1039/d3cs00991b

rsc.li/chem-soc-rev

Key Laboratory of Precision and Intelligent Chemistry, Collaborative Innovation Center of Chemistry for Energy Materials (iChEM), Department of Materials Science and Engineering, Anhui Laboratory of Advanced Photon Science and Technology, University of Science and Technology of China, Hefei 230026, China.
E-mail: huziqi@ustc.edu.cn, sfyang@ustc.edu.cn

Ziqi Hu

Ziqi Hu received his bachelor degree from Shandong University (2013) and PhD from Peking University (2018), under the supervision of Prof. Zujin Shi. He then moved to Spain as a postdoctoral fellow in the Institute for Molecular Science (ICMol), University of Valencia, in collaboration with Prof. Eugenio Coronado. In 2023, he joined Prof. Shangfeng Yang's group in the University of Science and Technology of China (USTC) as an associate researcher. Since his PhD studies, he has been fascinated by the structural and magnetic peculiarities of endohedral metallofullerenes towards their applications in single-molecule magnets and molecular spin qubits.

Shangfeng Yang

Shangfeng Yang received his PhD from Hong Kong University of Science and Technology in 2003. He then joined the Leibniz-Institute for Solid State and Materials Research (IFW) Dresden, Germany, as a Humboldt fellow. In December 2007, he joined the University of Science and Technology of China as a full professor in the Hefei National Laboratory for Physical Sciences at Microscale and the Department of Materials Science and Engineering. His research interests include syntheses of fullerene-based nanocarbons and applications in energy conversion and quantum technology. He was the recipient of the National Science Fund for Distinguished Young Scholars and "Hundreds of Talents Programme" of Chinese Academy of Sciences, and elected as Fellow of RSC (FRSC).

1. Introduction

Molecular nanomagnets represented by single-molecule magnets (SMMs) are magnetic molecules that possess bistable magnetic states depending on the alignment of the unpaired electrons and are able to maintain magnetization in the absence of an applied magnetic field.[1] This magnetic bistability at the molecular level and not related to a cooperative effect, concomitant with the intriguing quantum phenomena in the dynamics of their magnetization as well as the feasibility of rational design, atomically precise synthesis and multidimensional organizations, enables SMMs to be promising candidates for applications in high-density information storage,[1] spintronic devices[2] and quantum information technologies.[3,4] Since the discovery of the high-spin manganese cluster $Mn_{12}O_{12}$(acetate)$_{16}$ ($Mn_{12}Ac$) as the first SMM in 1993,[5] the major challenge for SMMs is their fragile magnetic bistability that is present so far only at cryogenic temperatures, and thus a central topic in the field has always been the exploration of methods to increase the blocking temperature (T_B), up to which the SMM behavior can be observed.

The advent of SMMs initially aroused research interests in multinuclear transition metal cluster compounds with the aim to increase the effective energy barrier to magnetization reversal (U_{eff}) by increasing the spin ground state and ligand field splitting exerted by the coordinated ligands. Later, it was found that metal complexes containing a single lanthanide (Ln) ion may serve as SMMs with large U_{eff} in the presence of ligand fields, which stems from the larger magnetic moment and single-ion anisotropy of Ln ions as a result of much stronger spin–orbit coupling (SOC) compared to the transition metal ions.[6–8] This category of Ln-based single-ion magnets (SIMs) constitutes a key part of the whole SMM family and has been receiving much research attention. The fine control of the single-ion anisotropy in SIMs thus becomes feasible through coordination chemistry, for which several design criteria were proposed mainly focusing on the enhancement of ligand fields.[9,10] These synthetic strategies are exemplified, for instance, by introducing cyclopentadienyl (Cp) ligands to ensure an axial anisotropy of a dysprosium metallocene cation $[Dy(Cp^{ttt})_2]^+$ (Cp^{ttt} = 1,2,4-tri-*tert*-butyl Cp), enabling a remarkably high T_B of 60 K at which magnetic hysteresis still persists. Such an extraordinary SMM property has been later improved up to 80 K, exceeding the liquid nitrogen temperature (77 K), by engineering ligand structures to protect spin states from the phonon relaxation bath which is mediated by molecular vibrations.[11,12]

Besides the low T_B that hampers the applications of SMMs, another major obstacle to their practical application in information storage is the prevailing chemical instability of organometallic compounds, which precludes their sublimation in order to obtain organized molecular assemblies on surfaces. Thus, inert ligands that are able to protect magnetic Ln ions are necessary. In this context, encapsulating Ln ion(s) into a chemically stable fullerene cage offers an alternative solution. The as-formed endohedral metallofullerenes (EMFs) feature a unique intramolecular host–guest molecular structure, in which specific metal clusters with previously unseen bonding and electronic configurations are stabilized in a way that could not be fulfilled by conventional synthetic routes.[13,14] Since the discovery of the first EMF-SMMs in a mixed trimetallic nitride clusterfullerene (NCF) $DySc_2N@C_{80}$,[15] EMFs have become a fertile territory in the exploration of high-performance SMMs by providing a rich structural diversity of both the encapsulated species and the host fullerene cages. Apart from metal clusterfullerenes bearing metal clusters in the cage, conventional EMFs based on the encapsulation of single or multiple metal ions only are also found to behave as decent SMMs.[16,17] A recent manifestation demonstrates that a low-coordination monometallic azafullerene $Dy@C_{81}N$ displays a high standardized blocking temperature ($T_{B,100s}$, defined as the temperature of 100 s relaxation time $T(\tau_{100s})$) of 45 K despite a weak ligand field, highlighting the uniqueness of EMFs in which the outstanding SMM performance is ascribed to the quenching of the extra radical on the cage by nitrogen substitution and the very weak coupling of the molecular vibrations to the spin states.[16] Another notable example lies in the discovery of several dimetallic EMF-SMMs $M_2@C_{79}N$ (M = Dy and Tb) and $M_2@C_{80}$-R (R = CF_3 and $PhCH_2$) exhibiting giant coercive field and a high $T_{B,100s}$ of up to 25.2 K for $Tb_2@C_{80}(CH_2Ph)$, where a single-electron metal–metal bond (SEMB) is stabilized to evoke strong magnetic coupling through quenching the unpaired electron on the cage by nitrogen substitution or exohedral derivatization.[18–22] Remarkably, this structural peculiarity is not an exclusive case in EMFs, yet offers a general synthetic insight and can be extended to strongly coupled mixed-valence dilanthanide SMMs $(Cp^{iPr5})_2Ln_2I_3$ (Ln = Dy and Tb) that hold the current record $T_{B,100s}$ value of 72 K.[23]

Exploiting the high chemical and thermal stability of fullerene structures, neutral EMF-SMMs can be readily processed into organized molecular assemblies, such as sub-monolayer deposition on substrates through sublimation or self-assembly.[24–26] This is in striking contrast to most ionic organometallic Ln-SMMs, which are air- and moisture-sensitive and would decompose upon heating or interacting with the substrates. This merit of EMFs allows a step forward in the field of SMMs by facilitating their further integration into spintronic devices, which would be eventually utilized to write in and read out magnetic information. Thus, EMFs are expected to continue to play a crucial role in the future development of SMMs. Moreover, the structural diversity of EMFs shall lead to further synthetic advancements by presenting new structures that in turn contribute to new physical phenomena in molecular magnetism.

In this review, we present an exhaustive review on all types of EMF-SMMs reported to date, including their syntheses, molecular structures, magnetic properties and organizations into molecular assemblies. We pay special attention to the versatile molecular structures of EMFs to unveil their unique structural features in comparison with conventional organometallic compounds, and manage to disclose the correlation between their structures with the magnetic properties. At the end, we propose

design strategies for EMF-SMMs towards improved performance by engineering underlying factors such as ligand fields, electronic structures, magnetic interactions, and molecular vibrations that can couple to the spin states.

2. Syntheses and molecular structures of EMFs

EMFs are typically synthesized by using the Krätschmer–Huffman DC-arc discharge method,[27] in which a metal precursor, in the form of metal alloy or metal oxide, is evaporated together with the graphite anode under a helium atmosphere as a cooling gas. Other gases or solid compounds, such as N_2, NH_3, CH_4 and Prussian blue ($Fe_4[Fe(CN)_6]_3$), can be added as reactive gases and nitrogen sources for the synthesis of a desired EMF.[28–30] The EMF-containing raw soot produced by the DC-arc discharge approach is then extracted using organic solvents, such as CS_2 and *ortho*-dichlorobenzene (*o*-DCB), using a Soxhlet extraction or reflux method to separate soluble fullerene-related compounds from other carbon materials. The final step is to isolate isomerically pure EMFs using multi-stage high-performance liquid chromatography (HPLC). Since the production process takes place at very high temperatures (3000–5000 K), the extracted products include a rich variety of empty fullerenes and endohedral metallofullerenes with different structures of the host cages and the encapsulated species. This makes the HPLC isolation a demanding and time-consuming process, but it is still feasible by employing a combination of different modified HPLC columns. Overall, the yields of EMFs in the purified forms are usually very low (in the order of milligram). Efforts have been devoted to increasing their production yields, resulting in some success in the selective synthesis of particular types of EMFs.[20,29–31]

The accurate structural determination of the isolated EMFs is achieved by single-crystal X-ray crystallography, for which co-crystals are obtained in the presence of nickel octaethylporphyrin (Ni^{II}(OEP))[32] or decapyrrylcorannulene (DPC)[33] hosts to restrict the rotation of the fullerene cages. For additional structural characterization various spectroscopic techniques including ^{13}C NMR, IR and Raman spectroscopies are utilized in aid of DFT calculations. Note that for EMFs containing paramagnetic Ln ions that are of interest for magnetic characterization, it is difficult to record ^{13}C NMR spectra due to spectral broadening caused by such magnetic centers. The detailed discussions on the synthesis, separation and structural characterization of EMFs have been summarized in several recent reviews.[13,14,34–36]

EMFs have versatile molecular structures dependent on the encapsulated species and the outer fullerene cages, and thus the corresponding magnetic properties are tunable upon changing their structures.[13] For the conventional EMFs based on encapsulation of single or multiple metal ions only, mono-, di- and tri-metallofullerenes can be formed by encaging different numbers (one to three) of metal atoms. In this context, mono- and di-EMFs are of particular interest for the magnetic studies in this review due to their structural diversity, whereas examples of tri-EMFs are very limited.[16,17,37] In fact, mono-EMF La@C_{82} dates back to a very early period just after the discovery of the empty fullerene C_{60}.[38,39] It should be noted that the encapsulated metal atoms transfer their valence electrons to the host fullerene cage, which is distinct from the situation of endohedral fullerenes encapsulating only nonmetal elements as exemplified by N@C_{60}.[40] This feature provides another aspect for fine-tuning the magnetic properties of EMFs by altering their electronic structures through nitrogen substitution[41–43] and exohedral functionalization[18,20,44] on the cages.

Alternatively, metal atoms can bond with nonmetal ligands inside fullerene cages to form clusterfullerenes.[14] Starting from a coincidental discovery of the nitride clusterfullerene (NCF) Sc_3N@C_{80},[28] which has a relatively high yield during the DC-arc discharging process that is inferior to only C_{60} and C_{70}, various types of clusterfullerenes have been synthesized including carbide,[45] oxide,[46] sulfide,[29] cyanide[47] clusterfullerenes, *etc.*, where the nonmetal ligands formally possess negative charges such as N^{3-}, C_2^{2-}, O^{2-}, S^{2-}, and CN^-, respectively. From the point of view of magnetic properties, these clusterfullerenes allow the manipulation of the ligand fields exerted on the Ln ions *via* coordination chemistry, thus adding another degree of freedom that can be used for the design of EMF-SMMs.

On the other hand, the structures of fullerene cages hosting encapsulated metal species are diverse not only in cage size but also in cage isomerism. The reported EMFs to date have a cage size ranging very broadly from C_{60} in Li@C_{60} cations to C_{108} in Y_2C_2@C_{108}.[48,49] The large cage family of EMFs, considering numerous isomers for the same cage size involving different connection ways of pentagons and hexagons, is further expanded by breaking the famous isolated-pentagon rule (IPR).[50] Among them, the most notable example is the highly symmetric icosahedral $I_h(7)$-C_{80} due to its exceptional stability after accepting six electrons from the encapsulated species, based on which various EMF-SMMs are constructed.[17,51,52] These rich cage structural features provide the feasibility of engineering ligand fields around metal ions by the control of metal–cage interaction. Furthermore, the configuration of the encapsulated species may be influenced by the structural variation of the cage, in a way that the cluster geometry or the metal–metal distance is changed, which enables the manipulation of ligand fields or magnetic exchange interactions. Molecular structures of representative EMFs of interest for magnetic studies in this review are illustrated in Fig. 1.

3. Magnetic characterization of EMF-SMMs

The majority of SMMs are characterized using the conventional superconducting quantum interference device (SQUID) magnetometers. There are several metrics to evaluate the performance of an SMM. Here we summarize and explain these different metrics, and unify common characterization of the

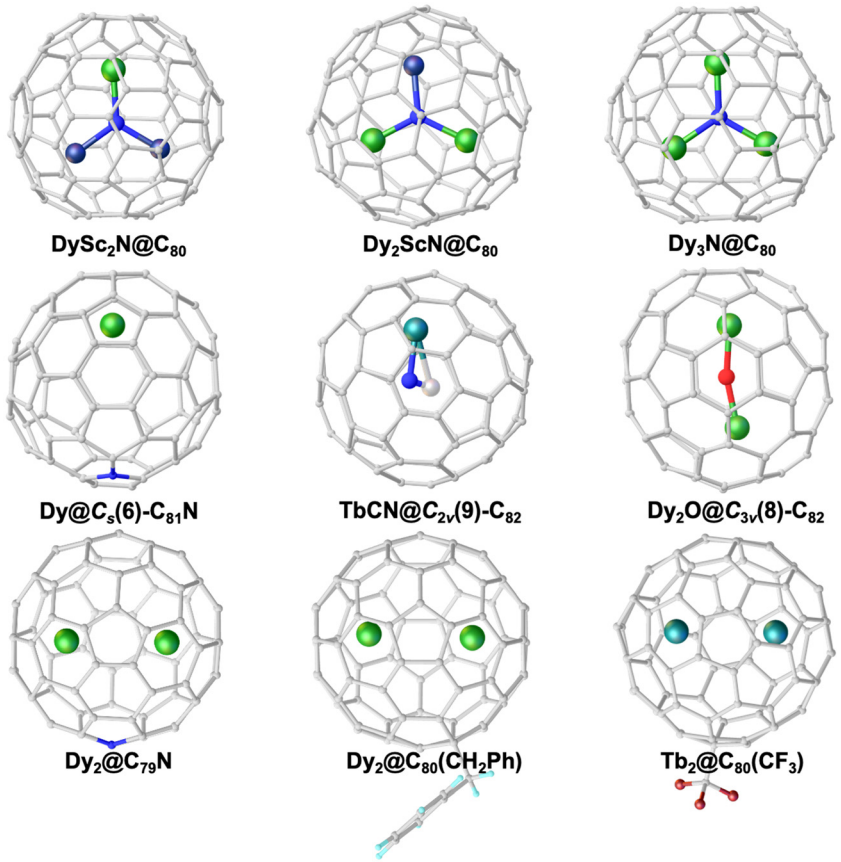

Fig. 1 Molecular structures of representative EMF-SMMs. Green: Dy, cyan: Tb, dark blue: Sc, blue: N, red: O, magenta: F, and gray: C.

static magnetism and the dynamic behavior. When it comes to the magnetic characterization of EMFs, special care should be undertaken mainly owing to their low yields, which may lead to various challenges in sample preparation, measurement and data analysis. We try to clarify some practical concerns in these steps and discuss detailed issues that need to be taken into account.

The low sample amount of EMFs (usually around 1 mg) makes the precise determination of the sample mass difficult, which normally requires a sample preparation method by drop-casting from CS_2 solution of an EMF into a diamagnetic propylene capsule.[18] Another method utilizes paramagnetic Al foil as the sample holder with its well-characterized magnetic behaviors.[22,53] In any case, background correction is necessary to accurately record the magnetization signal of the measured EMF. Since the EMF samples are mainly prepared in powder rather than in crystalline forms for magnetic characterization studies, the fullerene molecules are strongly disordered such that the measured values of magnetization should be doubled due to an isotropic distribution of easy axes of the molecules.[18,54] It becomes impossible to precisely determine the sample mass when it is less than 0.1 mg. Under this circumstance, a standard quartz sample holder can be used for a vibrating sample magnetometer (VSM) SQUID, which has a negligible diamagnetic background signal at helium temperatures.[55] Valuable information can still be obtained in this context by relying on the shapes, instead of the absolute values, of the variable-field magnetic susceptibility and variable-temperature magnetization data.

One of the most straightforward ways to identify an SMM is to record a magnetic hysteresis loop at a given temperature, which presents a magnetic memory effect that comes from the magnetic bistability. The opening of the hysteresis loops up to a certain temperature has been well-used as one definition of T_B. However, this hysteretic behavior is highly dependent on the sweep rate of the applied magnetic field during the measurement, such that the temperature at which hysteresis persists is not parameter-free. Another definition of T_B is derived from the bifurcation point of the zero-field cooling/field cooling (ZFC/FC) magnetic susceptibility curves. Similarly, this bifurcation temperature relies on the experimental temperature sweep rate. Thus, the comparison of the T_B values among different SMMs, determined either as hysteresis temperature or ZFC/FC bifurcation temperature, should be done with caution. Apart from T_B, the width of the hysteresis loop (*i.e.* coercive field, H_c) is equally important, which is the measure of the ability of an SMM to withstand while being demagnetized, and thus it would directly affect the stability and reliability of magnetic information that can be stored. The coercive field is mainly governed by the quantum tunneling effect that takes place close to zero

magnetic field. This again is related to the sweep rate of the applied magnetic field.

A more reliable definition of T_B, at which 100 s magnetic relaxation time (τ) is determined from the decay of magnetization, is free of experimental parameters and thus serves as a golden standard for SMMs in current state-of-the-art research.[1] This demagnetization at a given temperature follows an exponential decay of magnetization M over time

$$M(t) = M_{eq} + (M_0 - M_{eq})\exp[-(t/\tau)^{\beta}] \quad (1)$$

where M_{eq} and M_0 denote the equilibrium and initial magnetizations, respectively. It is very common that the demagnetization deviates from the single exponential decay ($\beta = 1$) due to the change of the relaxation rate over time, which is presumably caused by the local dipolar change thereof.[21] Instead, a stretched exponential function is often used ($0 < \beta < 1$) to fit the decay curve that in turn gives the τ value (>10 s) at a given temperature. In this review, for consistency we denote the temperature of 100 s relaxation time $T(\tau_{100s})$ as $T_{B,100s}$, and refer to other critical metrics of T_B as hysteresis temperature ($T_{B,hys}$) and bifurcation temperature in ZFC/FC curves ($T_{B,ZFC}$), respectively. Understanding the temperature dependence of the magnetic relaxation is a fundamental subject in the field of SMMs. This behavior can be described by a single or a combination of several possible relaxation mechanisms as follows

$$\tau^{-1} = {\tau_{QTM}}^{-1} + A_H T + CT^n + {\tau_0}^{-1}\exp(-U_{eff}/T) \quad (2)$$

where the first term denotes the temperature-independent quantum tunneling of magnetization (QTM) which causes a spin flip within the ground doublet, and the rest three terms represent the direct, Raman and Orbach mechanisms. The analysis of the well-known Orbach process following an Arrhenius-type relationship determines the effective energy barrier U_{eff}, which is another key factor of an SMM related to the relaxation of magnetization through the excited state. However, relaxation may occur *via* under-barrier pathways, including the Raman process with the assistance of phonons, thus resulting in a low T_B. Blocking the phonon-induced relaxation process has now become a central topic in SMM research. This involves the design strategy of decoupling spin states from molecular vibrations, providing not only theoretical insights[56–60] but also experimental evidence to show that sparse phonon spectra are crucial.[61–63]

In addition to demagnetization measurements which normally determine $\tau > 10$ s, the full characterization of the magnetic relaxation with τ spanning over a large range from 10^{-3} s to 1 s requires the dynamic studies by alternating current (AC) magnetometry. These AC measurements could be done in the absence of a static magnetic field with the variable frequency of the AC field in the range of 1–1000 Hz, and give rise to frequency-dependent in-phase (χ') and out-of-phase (χ'') susceptibilities, from which τ can be determined at different temperatures by fitting the data using a generalized Debye model. The exceptionally low yields of EMFs, however, often impede the accurate characterization using AC susceptibility to record the Orbach process for the determination of U_{eff}. This problem becomes worse when the slow magnetic relaxation is extended to high temperatures (>50 K), at which the sensitivity becomes lower since the out-of-phase signal χ'' almost vanishes based on the small population difference between spin states separated by a weak (~5 Oe) driving AC field.[16,64]

Alternatively, magnetic characterization of an SMM can also be performed *via* X-ray circular magnetic dichroism (XMCD) experiments on the atomic level. This advanced element-specific technique relies on X-ray absorption spectroscopy (XAS) for an SMM at the Ln $M_{4,5}$ edge, allowing for the unambiguous determination of the magnetic properties at its Ln origin, from which field-dependent XMCD hysteresis loops are extracted. Moreover, detailed atomic information, such as the expected values of the spin quantum number, angular momentum and the exact magnetic moment, can be precisely obtained by applying XMCD sum rules at the Ln edge, offering an in-depth insight into the magnetic behaviors of an SMM. It is noteworthy that much less sample is required for XMCD measurements compared to the amount used for commercial SQUID magnetometers, which is suitable for EMF-SMMs with low yields. However, the much noisier magnetic signal from XMCD measurements hampers the characterization of SMMs with weak coercive fields and low remanence at relatively high temperatures.

4. Categories of EMF-SMMs

4.1 Clusterfullerenes

4.1.1 Metal nitride clusterfullerenes (NCFs)

4.1.1.1 NCFs as single-ion magnets. The advent of trimetallic nitride clusterfullerenes (NCFs) showing the composition of $(M_1^{3+})_x(M_2^{3+})_{3-x}(N^{3-})@C_{2n}^{6-}$ (M_1/M_2 = rare earth metals, Ti, V; x = 1–3),[31,65–71] with $Sc_3N@I_h(7)$-C_{80} as an elegant example,[28] has opened up a new avenue for EMF research by offering a possibility to construct metal clusters inside the carbon cages. It is noteworthy that in this family of compounds, the most stable configuration of the encapsulated nitride cluster is a planar one, thus inducing a strong cluster size-dependent selection of preferential fullerene cages, which move from the most prevalent C_{80} to C_{88} and even to C_{96} as the radius of the metal ion increases.[32,72–74] From the magnetic point of view, the single-ion anisotropy of a magnetic Ln ion can thus be tailored by the encapsulated N^{3-} ligand and the outer cage coordination. To understand this feature in NCFs employing the trimetallic nitride template, the simplest model is a single-ion magnet (SIM) with only one magnetic center. This calls for a mixed trimetallic nitride through substituting one diamagnetic Sc^{3+} ion in $Sc_3N@C_{80}$ by a magnetic Ln^{3+} ion. In this regard, Dy^{3+} and Tb^{3+} with the oblate 4f electron density strongly facilitate axial single-ion anisotropy and thus are the most prevalent building blocks to design SMMs.[75] Specifically, Dy^{3+} has an odd number of f electrons (f^9) with the ground multiplet of $^6H_{15/2}$. This follows the Kramers theorem which indicates that the degeneracy of the ground doublet ($m_J = \pm 15/2$) cannot be lifted in the absence of a magnetic field. In contrast, the

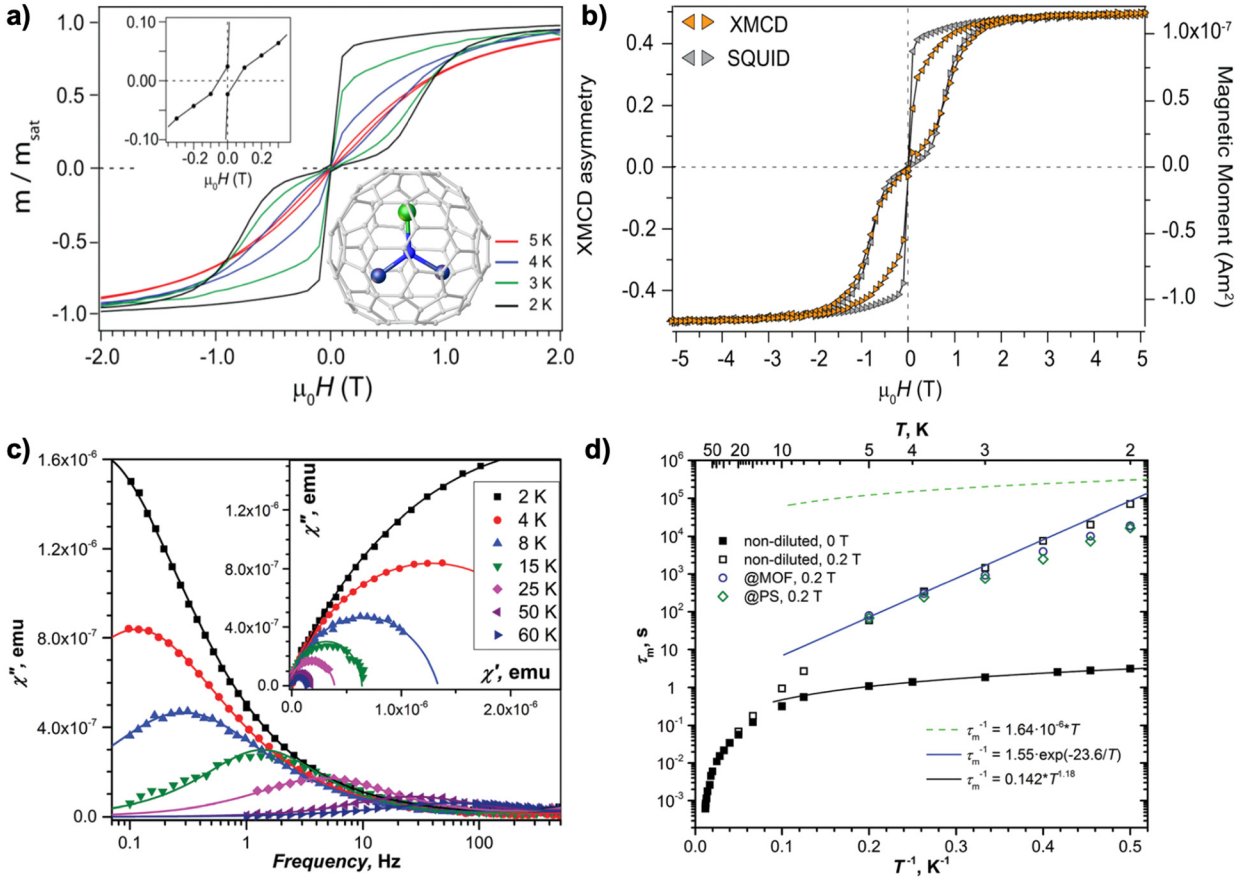

Fig. 2 (a) Magnetic hysteresis loops for $DySc_2N@C_{80}$ (the molecular structure is shown in the inset) recorded using SQUID magnetometry at 2–5 K with a field sweep rate of 1.3 mT s^{-1}. (b) Comparison of the magnetic hysteresis loops for $DySc_2N@C_{80}$ recorded by SQUID and XMCD magnetometry at 2 K. Reproduced with permission from ref. 15 (Copyright 2012, American Chemical Society). (c) Out-of-phase magnetic susceptibility χ'' of $DySc_2N@C_{80}$ measured in zero field in the 2–60 K range. The inset shows Cole–Cole plots. The solid lines are fits by the generalized Debye model. (d) Magnetization relaxation times of $DySc_2N@C_{80}$ at temperatures of 2–87 K. Zero-field values are shown as full dots and in-field (0.2 T) values are denoted as open dots. Relaxation times for non-diluted $DySc_2N@C_{80}$ are shown in black, and the values for diluted samples are shown in blue (diluted with MOFs) and green (diluted with polystyrene, PS). Reproduced from ref. 64.

non-Kramers ion Tb^{3+} is an even-number system without fundamental degeneracy. This leads to a tunnel splitting between the two lowest spin states and often gives rise to fast magnetic relaxation when the strict axiality is broken by low-symmetry ligand fields. As a result, majority of SIMs are based on Dy^{3+}.[76,77]

Following this strategy, the first EMF-SMM was reported by Gerber *et al.* in 2012 for $DySc_2N@C_{80}$, in which the nitrogen ligand (N^{3-}) imposes a strong ligand field around Dy^{3+} to achieve axial magnetic anisotropy.[15] This results in a magnetic hysteresis as shown in Fig. 2a that persists up to 5 K using a SQUID magnetometer at a slow magnetic field sweep rate of 1.3 mT s^{-1}. The hysteresis loop shows a clear drop in the low-field region with a butterfly shape, which indicates a fast QTM process typical of SIMs. This magnetic behavior is also confirmed by element-specific XMCD measurement, which shows hysteresis of the 4f spin and orbital moment in Dy^{3+} (Fig. 2b). Despite this, slow magnetic relaxation with τ exceeding 2000 s has been evidenced at zero field. The QTM effect can be effectively quenched by applying a magnetic field of 0.3 T, which facilitates the determination of $T_{B,100s}$ = 4.6 K. Such an effect is also suppressed by diluting $DySc_2N@C_{80}$ within a diamagnetic C_{60} matrix to greatly reduce intermolecular interactions. As a result, $\tau > 20\,000$ s is determined at zero field.

Since this first discovery, the magnetic behaviors of $DySc_2N@C_{80}$ have been extensively studied. Using the XMCD technique, the same group reported that X-rays lead to an increased relaxation rate of magnetization, which is induced by the resonant absorption of the X-ray irradiation and is dependent on its dose.[80] This additional demagnetization upon X-ray irradiation is helpful in understanding the thinner XMCD magnetic hysteresis compared to that recorded by using conventional SQUID magnetometry. An in-depth research of $DySc_2N@C_{80}$, focusing on its powder and single-crystal samples, as well as with solid dilutions in three different diamagnetic matrices, demonstrates that the dilution enlarges the hysteresis loops in the low-field region.[64] In this context, the use of a polystyrene diamagnetic matrix is the most effective approach, which steers the QTM resonance from 150 mT in an undiluted sample to <1 mT. This change of the zero-field

tunneling resonance width upon dilution significantly affects the relaxation rates and can be understood with the aid of an analysis of dipolar field distributions. Surprisingly, magnetic relaxation of $DySc_2N@C_{80}$ can be accessed by AC magnetometry in a very broad temperature range from 2 to 87 K (Fig. 2c and d). Magnetic relaxation up to such a high temperature is caused by the absence of a fast and linear Orbach process usually observed for other SMMs.

The single-ion anisotropy of Dy^{3+} can be manipulated in this type of NCF when Sc^{3+} is replaced by other diamagnetic rare earth metal ions such as Y^{3+} and Lu^{3+}. This is essentially due to the inner strain of the trimetallic cluster that is controlled by the sizes of different metals. Note that $DyLa_2N@C_{80}$ cannot be synthesized since the encapsulated cluster is too large to maintain a planar configuration. It has been shown that introducing a larger Lu^{3+} ion leads to a shorter Dy–N bond and hence a stronger ligand field than in $DySc_2N@C_{80}$.[78] Consequently, improved SMM properties are observed for $DyLu_2N@C_{80}$ with a $T_{B,ZFC}$ of 9.5 K in comparison with that of its traditional scandium congener (7 K). This study also points out that the mass of the diamagnetic metal ion is another important factor governing the SMM properties of NCFs by influencing cluster-based vibrations, which is achieved *via* a strong mixing of the local cluster vibrations with acoustic phonons, thus eventually affecting the magnetic relaxation. This observation has further been analyzed systematically in $DyM_2N@C_{80}$ (M = Sc, Y and Lu), which reveals that a larger size of M leads to stronger ligand fields in the order of Y > Lu > Sc. Moreover, magnetic behaviors are found to be correlated with the mass of M. This results in the improved SMM properties, both in terms of hysteresis at higher temperature and longer relaxation times, in the order of Lu > Y > Sc (Fig. 3a and c, Table 1).[79] A similar conclusion was also obtained by Wang *et al.* showing a larger opening of hysteresis in $DyY_2N@C_{80}$ compared to that of $DySc_2N@C_{80}$.[81]

In addition to the encapsulated diamagnetic metal that plays an important role in determining the single-ion anisotropy and thus the SMM properties of NCFs, the cage structure

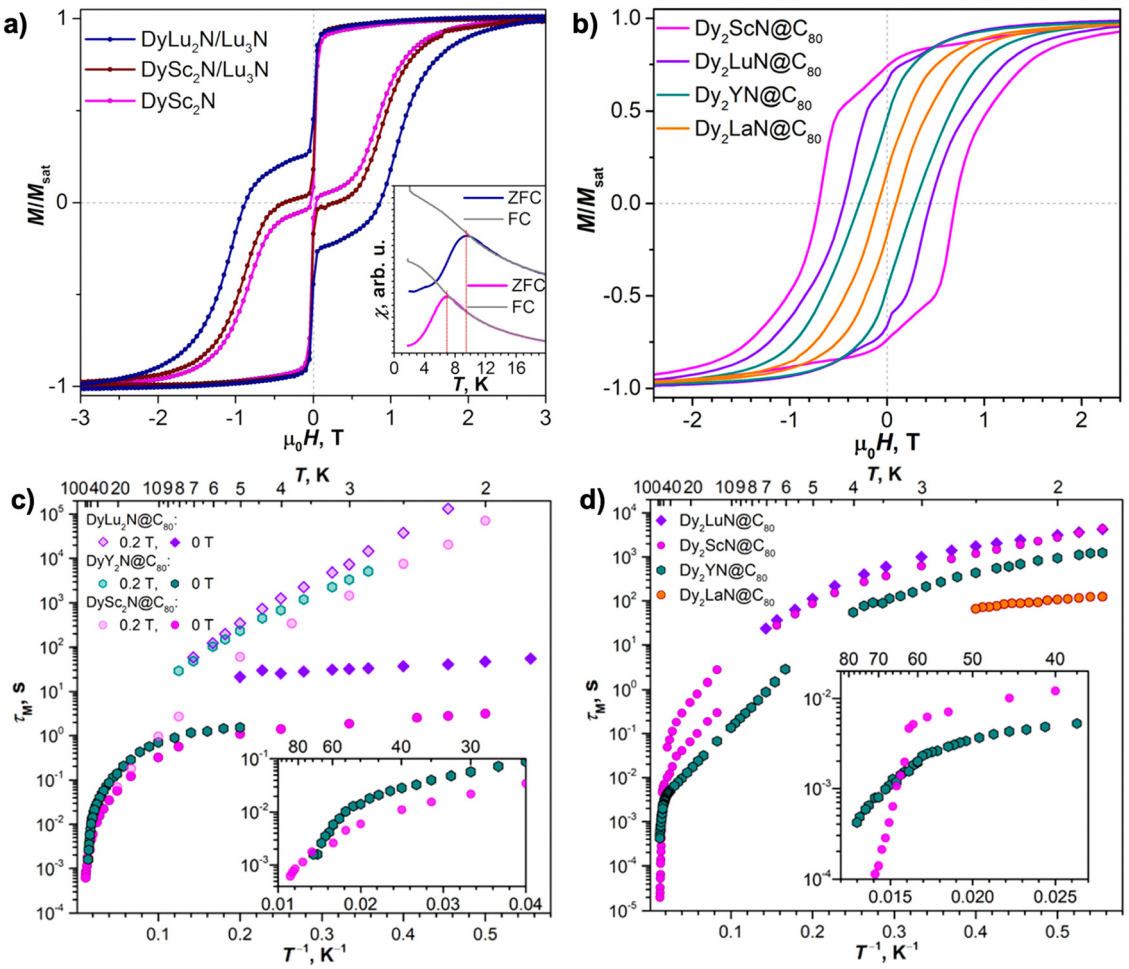

Fig. 3 (a) Magnetic hysteresis loops of $DyLu_2N@C_{80}/Lu_3N@C_{80}$ measured at 2 K and compared with those of $DySc_2N@C_{80}$ and $DySc_2N@C_{80}$ diluted with $Lu_3N@C_{80}$ in a 1 : 1 ratio. Sweep rate: 2.9 mT s^{-1}. The inset shows the determination of the bifurcation temperature, $T_{B,ZFC}$, from the temperature dependence of the magnetic susceptibility with a temperature sweep rate of 5 K min^{-1}. (b) Magnetic hysteresis loops for $Dy_2MN@C_{80}$ (M = Sc, Y, La, Lu) at 2 K (2.1 K for the La case) with a field sweep rate of 2.9 mT s^{-1}. (c) and (d) Magnetization relaxation times of $DyM_2N@C_{80}$ (M = Sc, Y, Lu) (c) and of $Dy_2MN@C_{80}$ (M = Sc, Y, La, Lu) (d). The insets in (c) and (d) show enlargement of high-temperature parts. Reproduced from (a) ref. 78 and (b)–(d) ref. 79.

Table 1 An exhaustive list of clusterfullerene SMMs reported to date

Type	EMF	$T_{B,100s}$ [K]	$T_{B,hys}$ [K](dH/dt) [mT s^{-1}][c]	$T_{B,ZFC}$ [K](dT/dt)[d] [K min^{-1}]	U_{eff} [K]	ΔE_{AFM-FM} [K]	Ref.
NCF-SIMs	$DySc_2N@D_3(6140)$-C_{68}	2.3[a]	5 (2.9)	3.8 (5)	23.6	—	84
	$DySc_2N@D_{5h}(6)$-C_{80}	3.6[a]	7 (2.9)	5.9 (5)	17.7	—	84
	$DySc_2N@I_h(7)$-C_{80}	4.6[a]	7 (2.9)	6.9 (5)	23.6	—	15 and 64
	$DyY_2N@I_h(7)$-C_{80}	~6[a]	8 (2.9)	8.4 (5)	929	—	79
	$DyLu_2N@I_h(7)$-C_{80}[b]	~6.5[a]	9 (2.9)	9.5 (5)	24.2	—	78 and 79
	$HoSc_2N@I_h(7)$-C_{80}[b]	—	—	—	16.5	—	85
NCFs with multiple magnetic metals	$Dy_2ScN@I_h(7)$-C_{80}	5.0	7 (2.9)	8 (5)	10.7/1735	8.1	95
	$Dy_2YN@I_h(7)$-C_{80}	~3.5	5 (2.9)	4.7 (5)	43.8/680	1.4	79
	$Dy_2LaN@I_h(7)$-C_{80}	~2	4 (2.9)	3.3 (5)	—	−1.2	79
	$Dy_2LuN@I_h(7)$-C_{80}	5.2	8 (2.9)	8 (5)	4.3	4.3	78 and 79
	$Dy_2GdN@I_h(7)$-C_{80}	~1.5	~1.8 (5.3)	—	15.1	—	96
	$DyErScN@I_h(7)$-C_{80}	~4.5	9 (33)	~8 (3)	12.5	7.0	97
	$Tb_2ScN@I_h(7)$-C_{80}	0.4	~0.4 (3.3)	—	1/10.5/56.4	9.4	98
	$Dy_2ScN@D_{5h}(6)$-C_{80}	2.6	7 (2.9)	5.3 (5)	8.4	—	84
	$Dy_2ScN@D_s(51\,365)$-C_{84}	~1.8	5 (2.9)	3.3 (5)	—	—	84
	$Dy_3N@I_h(7)$-C_{80}	—	~2 (0.8)	—	—	3.5	93
CYCFs	$TbCN@C_{2v}(19\,138)$-C_{76}[b]	—	—	—	12	—	99
	$TbCN@C_2(5)$-C_{82}[b]	—	—	—	10–20	—	100
	$TbCN@C_s(6)$-C_{82}[b]	—	—	—	10–20	—	100
	$TbCN@C_{2v}(9)$-C_{82}[b]	—	—	—	10–20	—	100
OCFs	$Dy_2O@C_s(10\,528)$-C_{72}	3.4	7 (2.9)	8 (5)	—	2.2	55
	$Dy_2O@C_2(13\,333)$-C_{74}	5.0[a]	14 (2.9)	14 (5)	—	~0.1	55
	$Dy_2O@C_{2v}(5)$-C_{80}	3.2	6 (2.9)	11 (5)	25.9	−26.6	101
	$Dy_2O@C_s(6)$-C_{82}	2.8	6 (2.9)	10 (5)	10.8	−10.8	102
	$Dy_2O@C_{3v}(8)$-C_{82}	5.9	7 (2.9)	9 (5)	7.8	−7.8	102
	$Dy_2O@C_{2v}(9)$-C_{82}	3.7	7 (2.9)	8 (5)	18.6	−18.6	102
	$Dy_2O@C_1(26)$-C_{88}	6.0	8 (2.9)	10.5 (5)	20.4	−23.7	103
	$Dy_2O@C_s(32)$-C_{88}	4.6[a]	8 (2.9)	8.5 (5)	—	−0.6	103
	$Dy_2O@D_2(35)$-C_{88}	3.9	8 (2.9)	8.5 (5)	—	5.2	103
SCFs	$Dy_2S@C_s(10\,528)$-C_{72}	—	3.0 (8.33)	—	—	—	29
	$Dy_2S@C_s(6)$-C_{82}	—	3.0 (8.33)	—	17.8	15.8	29 and 104
	$Dy_2S@C_{3v}(8)$-C_{82}	2.0	5 (8.33)	4.0 (5)	6.0	9.2	29 and 104
	$DyScS@C_s(6)$-C_{82}	~4	9 (10)	7.3 (5)	15.2	—	105
	$DyScS@C_{3v}(8)$-C_{82}	~2	9 (10)	7.3 (5)	6.5	—	105
CCFs	$DyYTiC@I_h(7)$-C_{80}	~5[a]	7 (2.9)	8 (5)	14.9	—	106
	$Dy_2TiC@I_h(7)$-C_{80}	1.7	3 (5)	—	9.5	12.2	107
	$Dy_2TiC_2@I_h(7)$-C_{80}	—	1.8 (5)	—	—	—	107
	$Dy_2TiC@D_{5h}(6)$-C_{80}	—	1.8 (5)	—	—	—	107
	$Dy_2C_2@C_s(6)$-C_{82}	—	3.0 (8.33)	—	17.4	17.4	29
	$Dy_2C_2@C_s(32)$-C_{88}	—	2.1 (2.9)	—	—	9.1	103
	$Dy_2C_2@D_2(35)$-C_{88}	—	2.1 (2.9)	—	—	4.7	103

[a] The value of $T_{B,100s}$ is determined under an applied magnetic field of 0.2 T. [b] Field-induced SMMs. [c] The value in the bracket indicates the field sweep rate (mT s^{-1}) used to record hysteresis loops. [d] The value in the bracket indicates the temperature sweep rate (K min^{-1}) used to record ZFC/FC curves.

is expected to be another degree of freedom that can be used for chemical design towards such a goal. In this line, it is the carbon ring motifs coordinating to the metal inside the cage that are of significance to the single-ion anisotropy and ligand fields, which include various binding sites such as a hexagon, pyracylene, and a fused-pentagon in a cage violating the isolated pentagon rule (IPR).[82,83] However, the number of mixed-metal NCFs based on fullerene cages instead of $I_h(7)$-C_{80} is rather limited, partly due to the exceptional stability and high yield of C_{80}^{6-} and also associated with the synthetic difficulty in HPLC separation of NCFs with different metallic clusters inside the same cage. Popov *et al.* reported the synthesis of $DySc_2N$ nitride clusterfullerenes with different carbon cages, including $D_3(6140)$-C_{68} and $D_{5h}(6)$-C_{80} as well as the well-studied $I_h(7)$-C_{80}.[84] Magnetic characterization of this series of NCFs shown in Fig. 4a and c indicates cage-dependent SMM properties, with the $I_h(7)$-C_{80} case as the best SMM featuring the broadest hysteresis loop at 2 K, the longest relaxation times and the highest bifurcation temperature ($T_{B,ZFC}$) of 7 K in ZFC/FC curves, the $D_{5h}(6)$-C_{80} fullerene as the intermediate one with $T_{B,ZFC}$ = 5.9 K followed by the $D_3(6140)$-C_{68} non-IPR cage with only 3.8 K.

The possibility to construct NCF-based SIMs using other anisotropic Ln^{3+} ions, instead of Dy^{3+}, has also been explored.

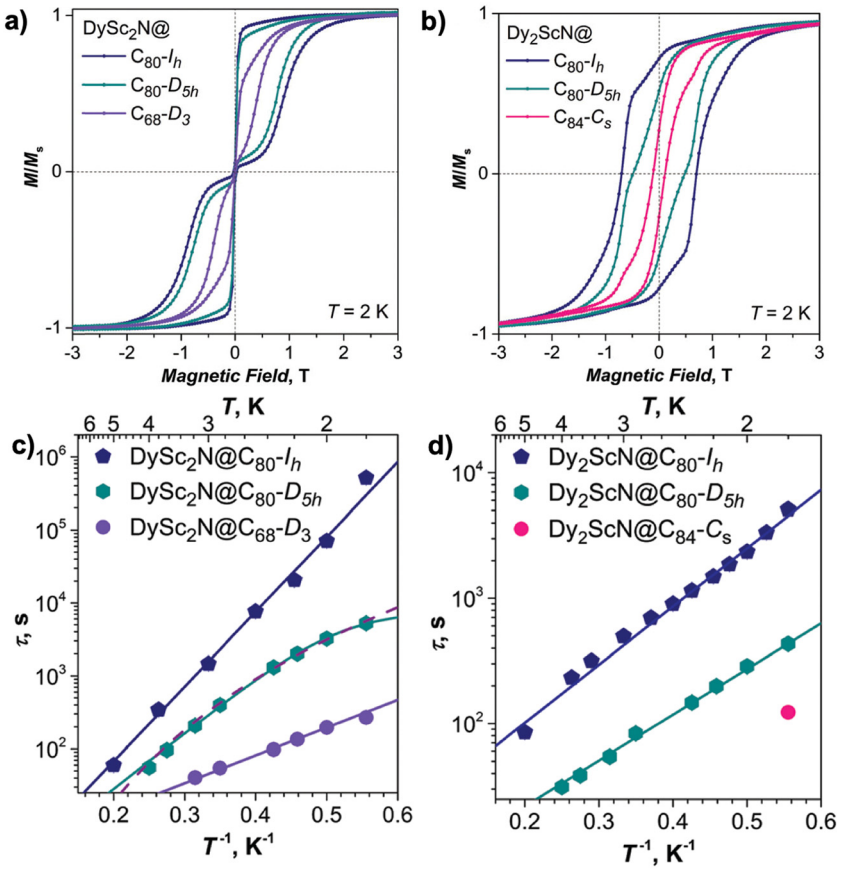

Fig. 4 (a) Magnetic hysteresis loops for different Dy-Sc NCFs, with the $DySc_2N$ cluster encapsulated inside D_3(6140)-C_{68}, D_{5h}(6)-C_{80} and I_h(7)-C_{80} cages, measured at 2 K with a field sweep rate of 2.9 mT s^{-1}. (b) Magnetic hysteresis loops for NCFs, with the Dy_2ScN cluster encapsulated inside D_{5h}(6)-C_{80}, I_h(7)-C_{80} and C_s(51 365)-C_{84} cages, measured at 2 K with a field sweep rate of 2.9 mT s^{-1}. (c) and (d) Magnetization relaxation times of $DySc_2N@C_{2n}$ ($2n$ = 68, 80 (two isomers)) (c) and of $Dy_2ScN@C_{2n}$ ($2n$ = 84, 80 (two isomers)) (d). Reproduced from ref. 84.

AC measurements of $HoSc_2N@I_h(7)$-C_{80} reveal that it is a field-induced SMM, that is, slow relaxation of magnetization is only shown in the presence of an applied DC field.[85] Although it is not a "genuine" SMM that functions at zero field, relaxation times in the order of milliseconds are determined below 6 K. The much faster relaxation rate of $HoSc_2N@C_{80}$ in comparison with that of $DySc_2N@C_{80}$ is attributed to its low-symmetry ligand field imposed by the cage which efficiently promotes the magnetic relaxation in the non-Kramers SIM. Similar to Dy-NCFs discussed above, the metal-dependent single-ion anisotropy of $HoM_2N@C_{80}$ (M = Sc, Lu, Y) was studied by paramagnetic ^{13}C NMR studies, XMCD analysis and ligand field calculations using a point-charge model.[86] The results indicate that despite the same magnetic ground state of Ho^{3+} with $|m_J|$ = 8 in these molecules, chemical shifts and ligand fields are strongly dependent on the size of the M^{3+} ion, which is consistent with the conclusion extracted from $DyM_2N@C_{80}$.[79] Furthermore, an interesting behavior was revealed for $HoLu_2N@C_{80}$, in which the encapsulated cluster can be oriented in a magnetic field since the Ho magnetic moment aligns along the Ho-N axis due to the strong ligand field.[87] Thus, a hopping motion of the cluster is possible upon applying external magnetic fields, and the activation energy associated with such a process can be determined for $HoLu_2N@C_{80}$ as well as for $TbSc_2N@C_{80}$, providing insights into the cluster–cage binding interaction.

Popov *et al.* systematically studied $MSc_2N@C_{80}$, using paramagnetic NMR combined with point-charge calculations, with M including all lanthanides (M = La, Ce, Pr, Nd, Tb, Dy, Ho, Er, Tm, Lu) that can be introduced into NCFs.[88] The ^{45}Sc NMR spectra are especially useful for the study of the magnetic properties of these NCF-based SIMs. The interpretation of these spectra accomplished by the point-charge model shows a strong axial ligand field generated by the short M–N bond length in each case. This leads to an easy-axis magnetic anisotropy for the lanthanide ions with an oblate shape of the 4f density (Ce^{3+}, Pr^{3+}, Nd^{3+}, Tb^{3+}, Dy^{3+}, and Ho^{3+}), and an easy-plane anisotropy for prolate lanthanide ions Er^{3+} and Tm^{3+}.

4.1.1.2 NCFs with multiple magnetic metal ions. Soon after the discovery of $DySc_2N@C_{80}$ as the first EMF-SMM, its single-ion anisotropy was investigated by Chibotaru *et al.* through *ab initio* calculations, revealing a large effective barrier exceeding 1000 K.[89] This high height of the barrier, however, does not simply guarantee a high blocking temperature due to the fast

QTM in the ground doublet as discussed above, which is further facilitated by hyperfine coupling to nuclear spins.[1,90] How to inhibit QTM has been central to the studies of SMMs directed towards magnetic bistability at high temperatures. To this end, the local symmetry of the coordination environment is found to be crucial to suppress QTM by minimizing the transverse ligand fields and reducing the mixing between different m_J states.[9] Another synthetic strategy is to design a di-nuclear SMM in which simultaneous reversal of magnetic moments on both lanthanide ions becomes difficult due to magnetic exchange interaction (or magnetic coupling) between them.[91,92] However, it is challenging in conventional organometallic compounds to achieve strong magnetic exchange between lanthanide ions having well-shielded 4f electrons. The confined sub-nanospace provided by a rigid fullerene cage, on the other hand, offers a possibility to enforce close proximity of Ln ions in an encapsulated metal cluster so as to enhance their magnetic coupling.

An *ab initio* investigation of the dinuclear $Dy_2ScN@C_{80}$ shows an exchange splitting with an energy barrier of $\sim$8 cm^{-1}, which is expected to efficiently block the QTM process at low temperatures, and thus may give rise to a high-performance SMM with a long magnetic relaxation time and large magnetic remanence.[89] Indeed, this prediction was later confirmed by magnetic characterization showing a much wider magnetic hysteresis at 2 K in contrast to the butterfly-shaped hysteresis of mononuclear $DySc_2N@C_{80}$.[93] The suppressed QTM in $Dy_2ScN@C_{80}$, as predicted by Chibotaru *et al.*,[89] is ascribed to a ferromagnetic coupling between two Dy^{3+} ions in the molecule. As a result, a 100 s blocking temperature $T_{B,100s}$ in the absence of a magnetic field is determined to be about 5.5 K. The angle between the magnetic moments on the two Dy sites can be precisely determined from temperature-dependent magnetization curves, in excellent agreement with the theoretical result showing that the quantization axes of the two Dy ions are collinear with the two Dy–N bonds.[94] Slow magnetic relaxation of $DySc_2N@C_{80}$ at higher temperatures can be probed by AC magnetometry up to 76 K.[95] A remarkably high effective barrier U_{eff} of 1735 K is extracted from the temperature dependence of τ, which exhibits an Orbach process functioning above 60 K. This thermally activated relaxation process is understood by *ab initio* calculations, and takes place *via* the fifth-excited Kramers doublet of the single-ion ligand field splitting in $Dy_2ScN@C_{80}$.

Similar to monodysprosium NCFs, the role that diamagnetic metals play in the SMM properties can be studied in didysprosium NCFs, where intramolecular magnetic coupling between two Dy^{3+} ions is of particular importance. Substituting Sc with Lu in $Dy_2ScN@C_{80}$, a similar bifurcation temperature ($T_{B,ZFC}$ = 8 K) is obtained for $Dy_2LuN@C_{80}$, while they differ in the interaction between the magnetic moments of Dy^{3+}, leading to different temperature and field dependence of the relaxation times.[78] In the series of $Dy_2MN@C_{80}$ (M = Sc, Y, La, and Lu), Dy$\cdots$Dy coupling and magnetic relaxation is mainly controlled by the size of M^{3+}.[79] The hysteresis becomes narrower when the ionic radius of M^{3+} is larger, and the relaxation rate at low temperatures is similar for NCFs entrapping Dy_2ScN and Dy_2LuN, but becomes progressively faster for Dy_2YN and Dy_2LaN with much larger clusters (Fig. 3b and d). These observations are correlated with the strength of Dy$\cdots$Dy coupling, and the corresponding energy difference between ferromagnetic and antiferromagnetic states (ΔE_{AFM-FM}) changes gradually from 8.1 K to -1.2 K as the size of M^{3+} increases. The mass of M, on the other hand, is less critical for the magnetic properties, meaning that the phonon degrees of freedom do not contribute heavily to the relaxation pathways in didysprosium NCFs compared to the situation in monodysprosium SIMs. Substitution of a diamagnetic Sc^{3+} ion in $Dy_2ScN@C_{80}$ with Gd^{3+} having half-filled f orbitals was also investigated.[96] It is demonstrated that the energy of the excited exchange state ΔE_{AFM-FM} decreases in $Dy_2GdN@C_{80}$ relative to that in $Dy_2ScN@C_{80}$. This results in a much faster QTM in $Dy_2GdN@C_{80}$, as evidenced by its very narrow hysteresis at 1.8 K; this acceleration of magnetic relaxation is due to the fact that the isotropic Gd^{3+} can act as a single-atom catalyst.

The interplay between cage structures and intramolecular magnetic coupling in didysprosium NCFs has been studied by encapsulating Dy_2ScN clusters into $I_h(7)$-C_{80}, $D_{5h}(6)$-C_{80} and a non-IPR $C_s(51\,365)$-C_{84} (Fig. 4b and d).[84] Similar to the result of monodysprosium NCFs employing different host cages, the best SMM properties of the didysprosium compounds are found in $I_h(7)$-C_{80}, which exhibits the broadest hysteresis and the highest bifurcation temperature $T_{B,ZFC}$ determined from ZFC/FC curves. The NCF with the non-IPR cage has the worst SMM performance in the series of compounds. This is also verified by the larger U_{eff} of the Orbach relaxation in $I_h(7)$-C_{80} *via* the exchange excited state compared to that in $D_{5h}(6)$-C_{80}, whereas shorter relaxation time of $Dy_2ScN@C_{84}$ precludes the study of its temperature dependence of relaxation time.

Apart from Dy^{3+}, the possibility to incorporate another Ln^{3+} into an NCF-based dinuclear SMM has also been explored. A heteronuclear NCF $DyErScN@I_h(7)$-C_{80} was reported as an SMM with a broadened hysteresis close to zero field compared to that of $DySc_2N@C_{80}$ due to the suppressed QTM, which stems from the magnetic exchange interaction between Dy^{3+} and Er^{3+}.[97] The more important feature of this molecule is the luminescent Er^{3+} ion integrated into the cage, which provides an additional function of characteristic Er^{3+} near-infrared emission for the SMM, rendering a bifunctional magneto-luminescent molecule. Incorporation of two non-Kramers Tb^{3+} ions instead of Dy^{3+} leads to a $Tb_2ScN@C_{80}$ SMM exhibiting magnetic hysteresis at sub-Kelvin temperatures, at which a relaxation time in the order of 100 s can be determined.[98] Analysis of the temperature dependence of τ indicates an Orbach process with 10 K U_{eff} arising from the exchange excited state due to magnetic coupling. The prefactor (τ_0 in eqn (1)) is 4 orders of magnitude smaller than that of the Dy congener, which is ascribed to the lack of Kramers protection in $Tb_2ScN@C_{80}$. The magnetic coupling can be better studied in dinuclear systems with two isotropic Gd^{3+} ions instead of other anisotropic Ln^{3+}.[108] Despite the fact that strong axial anisotropy is lacking in Gd^{3+}, which is beneficial to the design of an SMM,

magnetic characterization of $Gd_2ScN@C_{80}$ clearly confirms a ferromagnetic coupling between two Gd^{3+} ions, and also suggests a non-negligible anisotropy in the molecule.

The situation gets much more complicated when three magnetic Ln^{3+} ions are embedded simultaneously inside a fullerene cage using the trimetallic nitride template, where various ways of coupling three magnetization moments are possible in the trimetallic triangle. This magnetic coupling was first analyzed in $Ho_3N@C_{80}$ and $Tb_3N@C_{80}$ using magnetization curves.[109] The strong ligand fields are able to induce a collinear alignment of the individual moments parallel to the M–N bonds, giving rise to a ferromagnetically coupled net magnetic moment in each case. The ferromagnetic coupling was reported in experiment for $Gd_3N@C_{80}$,[108,110] as well as in theory for $Dy_3N@C_{80}$.[89] The latter is expected to trigger magnetic frustration that can greatly suppress magnetization blocking in the SMM regardless of the exchange barrier. Such a magnetic frustrated state is caused by the quasi-degeneracy of the three exchange multiplets in the ground state, that is, the net magnetic moment of the molecule can be aligned along each of the three Dy–N bonds. These predictions of the magnetic properties for $Dy_3N@C_{80}$ were later confirmed by experiments showing a very narrow magnetic hysteresis at 2 K, which is caused by the frustrated ground state as one of the simplest realizations of a frustrated and ferromagnetically coupled system.[93]

4.1.2 Metal cyanide clusterfullerenes (CYCFs). The vast majority of clusterfullerenes reported so far contain more than one metal ion inside the cage. Synthesis of monometallic clusterfullerenes was expected to be challenging since fewer electrons could be transferred from the encapsulated cluster to the outer carbon cage, thus contributing less to the stabilization of this type of host–guest molecule. This paradigm has been broken down with the discovery of the first monometallic cyanide clusterfullerene (CYCF) $YCN@C_s(6)\text{-}C_{82}$ by Yang *et al.*[47] X-ray crystallographic study shows a triangular cluster geometry which transfers two electrons to the cage, thus facilitating its encapsulation into the popular C_{82} fullerene with the stable 2- charged state which shares a similar electronic structure with mono-EMFs $M@C_{82}$ bearing a divalent metal ion (M = Sm, Eu, Yb).[111–115] This monometallic CYCF opens up a new avenue for the design of EMF-SIMs.

To this end, Tb^{3+} with large magnetic anisotropy was later introduced to form $TbCN@C_2(5)\text{-}C_{82}$.[116] The same group further synthesized terbium-CYCF based on three isomers of C_{82}, namely $C_2(5)$, $C_s(6)$ and $C_{2v}(9)$, all adopting a triangular cluster geometry as illustrated in Fig. 5a–c.[100] Variable-temperature magnetization measurements with the aid of a noncollinear magnetic moment model, which considers isotropic distribution of magnetic moments, reveal a magnetic ground state of $|m_J| = 6$ for each case. AC susceptibility studies demonstrate field-induced SIM properties for all these series of compounds (Fig. 5d–f). Remarkably, it is found that as the isomeric structure of the C_{82} cage varies from $C_2(5)$ to $C_s(6)$ and to $C_{2v}(9)$, the Tb–N distance becomes shorter, and the relaxation time increases accordingly, which is likely attributed to the enhanced ligand fields imposed on the Tb^{3+} ion. Thus, this direct correlation between the magnetic properties and the cluster geometry indicates a facile approach to fine-tune single-ion anisotropy by changing the cage structure in these SIMs. Indeed, upon further varying the host cage from the popular C_{82} to a non-IPR $C_{2v}(19\,138)\text{-}C_{76}$, the embedded TbCN cluster becomes nearly linear instead of maintaining the triangular geometry.[99] This geometric change is relevant to the strong metal–cage interaction in the presence of the fused-pentagon motif on the cage, as also evidenced by a combined

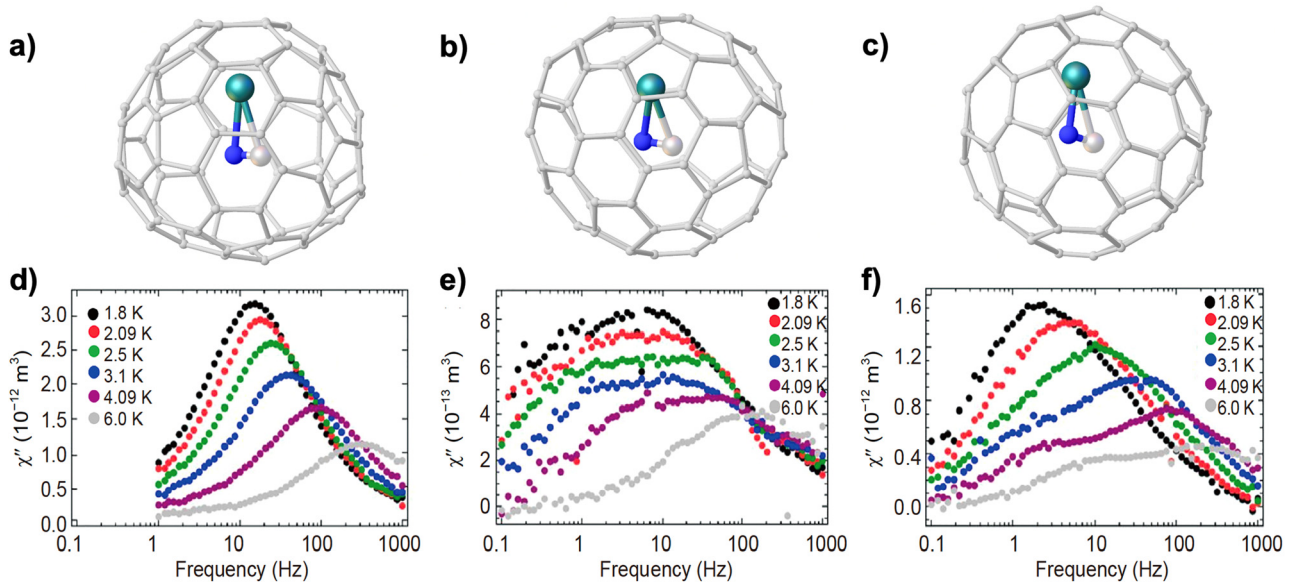

Fig. 5 Molecular structures of $TbCN@C_2(5)\text{-}C_{82}$ (a), $TbCN@C_s(6)\text{-}C_{82}$ (b) and $TbCN@C_{2v}(9)\text{-}C_{82}$ (c). Out-of-phase AC magnetic susceptibility of $TbCN@C_2(5)\text{-}C_{82}$ (d), $TbCN@C_s(6)\text{-}C_{82}$ (e) and $TbCN@C_{2v}(9)\text{-}C_{82}$ (f) at 1.8–6 K. Reproduced from ref. 100.

experimental and theoretical study on CYCFs encapsulating a LuCN cluster into C_{76} and C_{82} cages.[117] The field-induced SIM properties were verified by the frequency-dependent out-of-phase susceptibility χ'' observed in AC measurements for $TbCN@C_{76}$, from which a shorter relaxation time is extracted in comparison with that of its C_{82} counterparts. The reason for the faster relaxation rate in CYCFs with a linear cluster is still not clear. The QTM process governed by the local symmetry or spin-phonon coupling mediated by cluster-based vibrations may be accountable for this observation.

Although no further CYCF-based SIMs have been reported to date besides $TbCN@C_{76,82}$, synthetic efforts have been devoted in the field to expand this family of molecules by introducing different lanthanide metals and fullerene cages. In this regard, Dy-based CYCFs are of particular interest owing to their Kramers ion nature, which competes with non-Kramers Tb^{3+} and is usually associated with the suppressed QTM process. By employing Prussian blue as a cheap solid cyanide/nitrogen dual-source, Dy-containing CYCFs can be readily synthesized with high yields.[30] X-Ray crystallographic studies of the three isomers of $DyCN@C_{82}$ indicate the triangular geometry of the embedded cluster which is tunable upon varying the isomeric structure of the cage. Recently, the host cage of CYCFs was extended to C_{84} with two isomers $C_2(13)$ and $C_{2v}(17)$, while the metals involved encompass Y, Dy and Tb.[118] The missing $C_{2v}(17)$-C_{84}, which had never been reported before both in empty fullerenes and EMFs, can be interconverted from the $C_2(13)$-C_{84} isomer through two steps of Stone–Wales transformation. This demonstrates the advantage of the monometallic cyanide cluster in stabilizing novel fullerene structures. The subtle difference in the ionic radii of Y^{3+}, Dy^{3+}, and Tb^{3+} gives rise to a noticeable change in the metal–cage interaction, which can also be varied within different isomeric cages. Thus, the metal–cage interactions and the related single-ion anisotropy, if a magnetic Ln ion is introduced, can be altered *via* both the encapsulated cluster and host cage.

An alternative strategy to modify the cluster geometry was realized by exohedral functionalization on the cage *via* high-temperature trifluoromethylation.[119,120] This leads to the synthesis of multi-trifluoromethylated CYCFs based on C_{82} and C_{84}. Different derivatized products, including $YCN@C_{82}(CF_3)_{16/18}$ and $YCN@C_{84}(CF_3)_{16/18}$, have been structurally characterized using X-ray crystallography. These compounds are stabilized by the formation of isolated C=C bonds and benzenoid rings on the fullerene cages after CF_3 addition, which is able to localize the metal atoms within a particular fragment of the cage. Moreover, the encapsulated YCN cluster with triangular geometry can be further altered depending on the exohedral addition pattern. This shall allow the manipulation of the single-ion anisotropy for Dy^{3+}- or Tb^{3+}-based CYCFs and thus would certainly stimulate further studies on their SMM properties.

4.1.3 Metal oxide clusterfullerenes (OCFs). Considering the strong ligand field strategy directed at enhancing single-ion anisotropy and the effective barrier of magnetization reversal, it is reasonable to choose a stronger ligand over N^{3-} and CN^- in clusterfullerenes as discussed above. This leads to the entrapment of O^{2-} as a nonmetal inside the cage with higher electronegativity. The as-formed oxide clusterfullerenes (OCFs) were first synthesized by Balch *et al.* in tetrametallic molecules $Sc_4O_2@C_{80}$ and $Sc_4O_3@C_{80}$ with the oxygen atoms as μ_3-bridging ligands.[121,122] Note that since scandium has the smallest covalent radius among the family of rare-earth metals, these tetrametallic oxide clusters are limited cases so far, which precludes the synthesis of Ln-congeners with much larger encapsulated clusters that are of interest in this review from the magnetic point of view. The same group later reported another simpler form of OCFs $Sc_2O@C_s(6)$-C_{82} consisting of a slightly bent dimetallic oxide cluster, whose electronic structure can be described as $(Sc^{3+})_2O^{2-}@C_{82}^{4-}$.[46] The formal four-electron transfer from the cluster suggests that fullerene cages that can form stable tetraanions are suitable hosts in this type of OCF. Indeed, a series of OCFs entrapping Sc_2O clusters within a variety of fullerenes ranging from C_{70} to C_{82} were reported by Chen and Feng *et al.*, in which CO_2 is found to boost the yields of OCFs during the arc-discharging production process.[123–129] This template of OCFs can also be extended to lanthanide metals,[130–132] with a notable example of $M_2O@C_2(13\,333)$-C_{74} (M = Tb, Ho, Lu) featuring a linear M_2O cluster inside the non-IPR fullerene cage.[133–135] Understanding the interplay between the cluster geometry and the cage structure would be crucial to explore their magnetic properties.

Magnetic studies on this type of OCF started from a theoretical work focused on the single-ion anisotropy of heterometallic compounds $DyMO@C_{2n}$ (M = Sc, Lu; $2n$ = 72, 76, 82), where diamagnetic rare-earth metal ions are used in conjunction with anisotropic Dy^{3+} to avoid the relaxation pathway through low-lying exchange excited states that are induced by generally weak 4f–4f magnetic coupling.[136] As expected from a more electronegative O^{2-} compared to N^{3-}, *ab initio* calculations show a strong splitting of the $^6H_{15/2}$ ground multiplet for Dy^{3+} in each case. Detailed analysis of the wavefunctions of the doublets and the transition probability among them indicates that QTM can be quenched up to the third-excited doublet in the series of compounds. A very large effective barrier U_{eff} exceeding 2000 K is determined in $DyScO@C_{82}$. This highly axial anisotropy is expected to give rise to a strong SIM. However, heteronuclear OCFs have not yet been synthesized due to the difficulties both in synthesis and in separation. It should be noted that the overall yields of OCFs are much lower than those for NCFs, and the mixture of Dy_2O, Sc_2O and DyScO species makes the HPLC separation process a challenging task. Thus, one has to focus on the homonuclear system at this stage, where two magnetic Dy^{3+} ions are involved simultaneously. In this context, enhancing magnetic coupling interaction between two Dy^{3+} ions becomes crucial to suppress QTM as discussed in the above section on NCFs with multiple magnetic metal ions (4.1.1.2). Indeed, oxygen-bridged dinuclear compounds in various organometallic SMMs have been demonstrated to induce strong coupling between the two Dy^{3+} ions *via* superexchange interactions.[137–141]

To start with the discussion of the magnetic properties for these dinuclear Dy-SMMs, their low-energy spin states can be generally described using the following spin Hamiltonian

$$\hat{H}_{\text{spin}} = \hat{H}_{\text{LF1}} + \hat{H}_{\text{LF2}} - 2j_{12}\hat{J}_1\hat{J}_2 + \hat{H}_{\text{ZEE}} \quad (3)$$

where the first two terms are the single-ion ligand-field Hamiltonian for the *i*-th dysprosium site, and are obtained from *ab initio* calculations of the two Dy fragments substituting the other Dy^{3+} by a diamagnetic metal ion such as Y^{3+}; the third term represents the magnetic coupling interaction between the two Dy^{3+} magnetic moments $\hat{J}_i$ with j_{12} as the coupling constant; and the last term represents the Zeeman effect upon applying a magnetic field. The total magnetic coupling j_{12} is often treated in the literature, for simplicity, as an effective scalar term stemming from isotropic interaction, rather than a more complex anisotropic tensor.[142] This information can be either derived from the fitting of the isothermal magnetization and variable-temperature magnetic susceptibility curves, or from the analysis of temperature-dependent relaxation times correlating exchange excited states (with the energy of $\Delta E_{\text{AFM-FM}}$) with U_{eff} in the Orbach relaxation process. This total coupling consists of dipolar and exchange contributions, j_{dip} and j_{exch}. The dipolar term is dependent on the distance and relative orientation of the magnetic moments (easy axis of each metal ion) that are extracted from structure and *ab initio* calculations. The exchange term, determined as the difference of j_{12} and j_{dip}, represents magnetic interaction at a chemical origin as a result of orbital overlap between two metal ions, either in a direct way (Heisenberg exchange) or transferred by the bridging ligand (superexchange). Note that instead of the situation in Eqn 3 where lanthanide moment $\hat{J}$ is used, another convention of magnetic coupling Hamiltonian employs a projection of pseudospin $\tilde{S}_i = 1/2$ for the *i*-th magnetic metal center. To avoid ambiguity, therefore, we compare the corresponding energy difference between ferromagnetic (FM) and antiferromagnetic (AFM) states ($\Delta E_{\text{AFM-FM}}$) throughout this review. Under the $-2j_{12}\hat{J}_1\hat{J}_2$ convention illustrated in eqn (3), this energy splitting for a didysprosium system can be computed as

$$\Delta E_{\text{AFM-FM}} = 225j_{12}\cos(\alpha) \quad (4)$$

where α is the angle between quantization axes of two Dy^{3+} ions derived from single-ion anisotropy calculations, and the factor of 225 results from their $m_J = \pm 15/2$ ground state.

The first magnetically characterized OCF-based SMMs were reported in 2019 including three isomers of $Dy_2O@C_{82}$ with $C_s(6)$, $C_{3v}(8)$ and $C_{2v}(9)$ cage symmetries.[102] As illustrated in Fig. 6a–c, each of these molecules possesses a slightly bent shape for the encapsulated Dy_2O cluster which features unusually short Dy–O bonds of $\approx$2.0 Å, resulting in a very strong magnetic anisotropy of Dy ions with their magnetic moments aligning along the Dy–O bonds. $Dy_2O@C_{82}$ isomers show SMM behaviors with a broad magnetic hysteresis at low temperature (2 K), which persists up to 6–7 K using a field sweep rate of 2.9 mT s^{-1} (Fig. 6d–f). The opening of the hysteresis loop close to zero field is clear evidence of effective quenching of QTM by magnetic coupling of two Dy^{3+}, in contrast to the butterfly-shaped hysteresis observed for NCF-based SIMs.[15,81] A more interesting feature in $Dy_2O@C_{82}$ isomers lies in the inflection of their hysteresis loops. The abrupt drop of magnetization at zero field at 2 K, noticeable in the $C_{2v}(9)$ case, arises from QTM

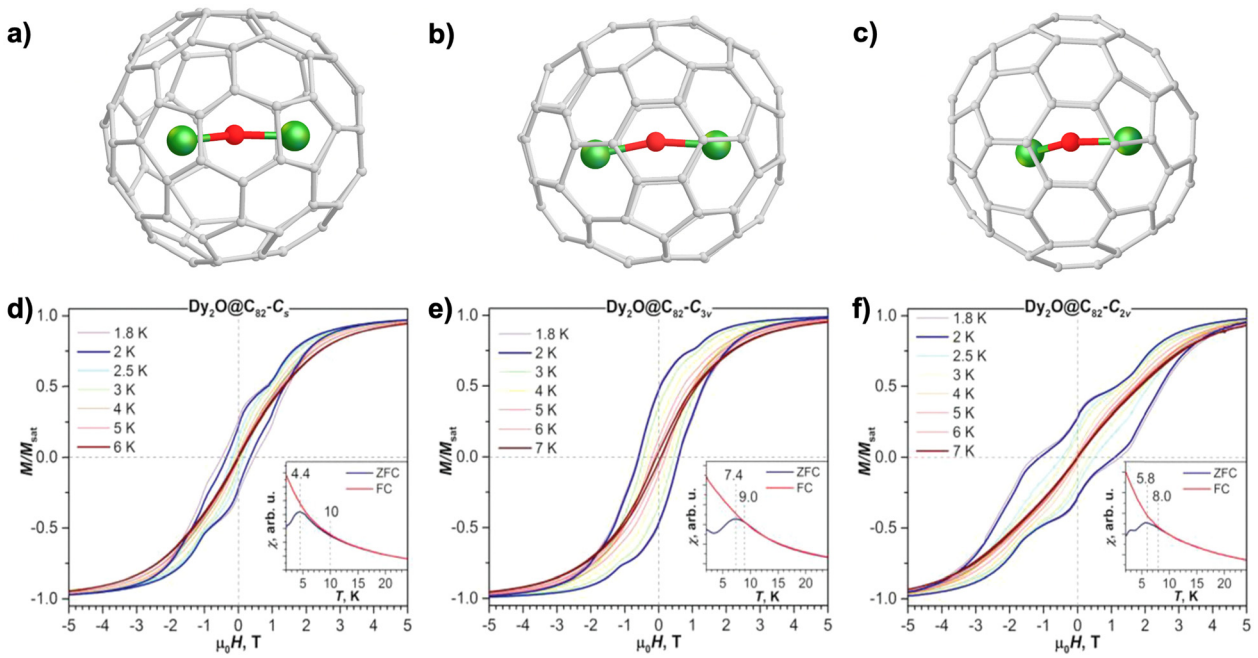

Fig. 6 Molecular structures of $Dy_2O@C_s(6)$-C_{82} (a), $Dy_2O@C_{3v}(8)$-C_{82} (b) and $Dy_2O@C_{2v}(9)$-C_{82} (c). Magnetic hysteresis curves of $Dy_2O@C_s(6)$-C_{82} (d), $Dy_2O@C_{3v}(8)$-C_{82} (e) and $Dy_2O@C_{2v}(9)$-C_{82} (f) in the range of 1.8–7 K using a field sweep rate of 2.9 mT s^{-1}. The insets represent their corresponding ZFC/FC curves at an applied magnetic field of 0.2 T with a temperature sweep rate of 5 K min^{-1}. Reproduced from ref. 102.

that is not completely quenched by magnetic coupling. The inflections away from the zero-field region, on the other hand, are ascribed to the Zeeman splitting of the energy of the FM and AFM states in the presence of a certain magnetic field, at which the crossing point is found between these spin states. It should be noted that this inflection phenomenon is much more obvious than that in the hysteresis of the ferromagnetically coupled $Dy_2ScN@C_{80}$,[95] in which the FM state is more likely to be the ground state at a certain molecular orientation without level crossing due to its stronger Zeeman response. Therefore, the complex feature of hysteresis indicates an antiferromagnetically coupled system for $Dy_2O@C_{82}$. The particular field of inflection can then be used to determine ΔE_{AFM-FM} as well as the coupling constant j_{12} combining eqn (3) and (4). Alternatively, the coupling situation can be understood, as discussed above, by the fitting of magnetization curves using eqn (3) and (4), or by the study of their relaxation mechanisms applying eqn (2) and (4). The latter gives the Orbach relaxation process *via* the FM excited state at low temperatures with U_{eff} corresponding to ΔE_{AFM-FM}. The value of ΔE_{AFM-FM} is thus determined as −7.8 to −18.6 K, suggesting that the Dy···Dy exchange coupling in $Dy_2O@C_{82}$ is the strongest at this time among all dinuclear Dy SMMs with diamagnetic bridges.[137,138,143–145]

The possibility of putting Dy_2O clusters into other fullerene cages has been explored, discovering two non-IPR cages $C_s(10\,528)$-C_{72} and $C_2(13\,333)$-C_{74} as suitable hosts.[55] The fused-pentagon moieties in these cages govern the positions of Dy^{3+} inside thanks to the strong metal–cage interaction, and the geometry of the Dy_2O cluster is controlled in this way, which is bent within C_{72} but becomes linear in C_{74}. The cage-dependent cluster geometry greatly affects the SMM behaviors of these two OCFs. Both molecules show open magnetic hysteresis at 1.8 K but with very different shapes. In the case of $Dy_2O@C_{72}$, the hysteresis loop is typical of an antiferromagnetically coupled SMM featuring quenched QTM in the absence of field and an inflection in the presence of field, similar to the situation of the abovementioned $Dy_2O@C_{82}$ isomers.[102] In contrast, $Dy_2O@C_{74}$ exhibits an SIM-like hysteretic behavior which is almost closed at zero field due to the strong QTM. Detailed analysis reveals that in this dinuclear Dy-SMM, the ferromagnetic dipolar coupling is nearly completely counterbalanced by the antiferromagnetic Dy–O–Dy superexchange interaction, thus leading to decoupled Dy moments that are accountable for such a SIM-like hysteresis. Although the relaxation rate of $Dy_2O@C_{74}$ is fast at zero field, slow relaxation (with $\tau > 40$ s) can be observed up to 6 K at a finite magnetic field of 0.2 T or 0.8 T. The magnetic hysteresis remains open up to 14 K in $Dy_2O@C_{74}$ and up to 7 K in $Dy_2O@C_{72}$ at a field sweep rate of 2.9 mT s^{-1}. The former value is the highest hysteresis temperature among all clusterfullerenes reported so far.

Compared to that of $Dy_2O@C_{82}$, even stronger Dy···Dy coupling was found by Popov *et al.* in $Dy_2O@C_{2v}(5)$-C_{80}.[101] The ΔE_{AFM-FM} determined by the fitting of magnetization data shows a very large value of −26.6 K (the dipolar and exchange contributions are 3.9 and −30.5 K, respectively), which is also consistent with the U_{eff} of 25.9 K extracted from the temperature dependence of magnetic relaxation time. $Dy_2O@C_{80}$ has a broad hysteresis at 1.8 K opening between −5 T and 5 T and with a coercive field of 0.65 T. A pronounced inflection of the hysteresis loop upon decreasing the field is observed, which is related to the level crossing between AFM and FM states. The magnetic hysteresis persists until 6 K using a field sweep rate of 2.9 mT s^{-1}, while the bifurcation temperature $T_{B,ZFC}$ is determined as 11 K from ZFC/FC measurements with a temperature sweep rate of 5 K min^{-1}.

Recently, this family of OCF-SMMs has been further extended to three C_{88} isomers with cage symmetries of $C_1(26)$, $C_s(32)$, and $D_2(35)$.[103] All isomers of $Dy_2O@C_{88}$ display slow relaxation of magnetization and magnetic hysteresis. The latter measure of SMMs can be observed up to 7–9 K at 2.9 mT s^{-1} sweep rate. It is worth noting that $Dy_2O@C_{88}$ represents EMF-SMMs possessing the largest carbon cages to date. The three isomers of $Dy_2O@C_{88}$ also allows for the study of their SMM properties as a function of the isomeric fullerene cage. Similar to the above analysis of other OCF-SMMs with smaller cages, it seems clear that the O^{2-} bridge favors antiferromagnetic exchange coupling between the two Dy^{3+} ions. The strength of Dy···Dy superexchange interactions, however, differs significantly upon varying the isomeric structure of the C_{88} cage. The comparative analysis of all nine OCF-SMMs reported so far reveals that only $Dy_2O@D_2(35)$-C_{88} has a moderately positive ΔE^{exch}_{AFM-FM} value of 2.0–3.2 K, considering only superexchange interactions without the contribution from the dipolar terms. All the other eight molecules feature a negative exchange term, which ranges from the modest −2.2 K in the case of C_{72} to very large −27.3 K in $C_1(26)$-C_{88} and −30.5 K in C_{80}, with the latter two being the strongest Dy···Dy interactions in all didysprosium compounds reported by far. Further enhancing the magnetic coupling in Dy-OCFs is definitely a research direction aimed at increasing the blocking temperature of this type of SMM. Despite the fact that unfortunately no clear structural correlation of the exchange coupling strength is concluded in the present literature for Dy-OCFs, the structural diversity of the fullerene cage would become a rich playground to achieve such a goal in future studies.

4.1.4 Metal sulfide clusterfullerenes (SCFs). Replacing the oxygen atom in OCFs by a sulfur atom, a new type of metal sulfide clusterfullerene (SCF) can be constructed in the form of $M_2S@C_{2n}$ (M = Sc, Ti, Y, Dy, Er, Lu; $2n$ = 70–82) with a similar electronic structure to that of OCFs. The first SCFs $M_2S@C_{3v}(8)$-C_{82} (M = Sc, Y, Dy, Lu) were synthesized by Dunsch *et al.* using guanidium thiocyanate (CH_5N_3·HSCN) as a solid sulfur source during the arc-discharging production process, and were characterized by various spectroscopic techniques in combination with DFT calculations.[146] Very soon after this first discovery, Echegoyen *et al.* reported the synthesis of a series of scandium sulfide clusterfullerenes $Sc_2S@C_{2n}$ ($2n$ = 80–100) by introducing SO_2 as the sulfur source, among which Sc-SCFs based on two isomers of C_{82}, with the cage symmetries of $C_s(6)$ and $C_{3v}(8)$, have been isolated and spectroscopically characterized.[147] The molecular structures of the two isomers of $Sc_2S@C_{82}$ were then

determined crystallographically to show significantly bent Sc_2S clusters inside the fullerene cages.[148] Later, it was found in the crystal structure that this bent shape is maintained inside a C_s(10 528)-C_{72} cage violating the isolated-pentagon rule.[149] Following this synthetic strategy, Sc_2S clusters can be entrapped in an even smaller non-IPR C_2(7892)-C_{70} cage, which is closely connected with the previously reported C_s(10 528)-C_{72} by a direct insertion of a C_2 unit.[150] This sulfide template can be extended to Er-SCFs employing the two most stable C_{82} isomers (C_s(6) and C_{3v}(8)),[151] and is also able to stabilize transition metal-only clusters inside a fullerene cage, forming $Ti_2S@D_{3h}(5)$-C_{78}.[152] DFT calculations of the latter suggest an almost linear geometry of the Ti_2S cluster which transfers six electrons to the cage due to the tetravalent oxidation state of titanium, distinct from the four-electron transfer in conventional SCFs encaging trivalent rare-earth metal ions.

Similar to OCF-SMMs with strong magnetic coupling between two Dy^{3+} ions, Dy-SCFs are of particular interest for magnetic studies. By using Dy_2S_3 as a solid source of metal and sulfur, and adding methane to a reactive atmosphere so as to reduce the formation of empty fullerenes in the arc-discharging process, Dy-SCFs can be selectively synthesized as the main fullerene products.[29] Among them, two C_{82} isomers (C_s(6) and C_{3v}(8)) and C_s(10 528)-C_{72} have been successfully isolated, and the structures of the former two isomers were unambiguously determined by single-crystal XRD characterization to reveal significantly bent Dy_2S clusters inside the cages. All these three molecules exhibit magnetic hysteresis at low temperatures, with the C_{3v}(8)-C_{82} case being the best SMM showing open hysteresis up to 4 K using a field sweep rate of 8.33 mT s^{-1} and $T_{B,ZFC}$ = 4 K at a temperature sweep rate of 5 K min^{-1} in ZFC/FC measurements. Its dynamic magnetic properties can be studied by DC and AC susceptibility measurements in the temperature range from 1.6 K to 70 K. This exceptional slow magnetic relaxation up to high temperatures enables the determination of three Orbach relaxation processes with U_{eff} of 10.5, 48 and 1232 K, respectively. The first energy barrier is associated with the magnetic exchange excited state similar to that for Dy-OCFs; the intermediate barrier can be ascribed to the local vibrational mode of librating the Dy_2S cluster within the cage, while the highest value matches the excited doublet in the single Dy^{3+} ligand field. On the other hand, $Dy_2S@C_s(6)$-C_{82} has a faster magnetic relaxation featuring two barriers of 15.2 and 523 K, corresponding to relaxation *via* the exchange excited state and *via* the excited doublet in ligand field splitting, respectively. Comparing the magnetic behaviors of these SCFs with their OCF counterparts, it is evident that generally weaker SMM performance can be found in SCFs. This disparity originates from the lower electronegativity and the larger covalent radius of sulfur. The latter results in the bent shape of the cluster instead of nearly linear one usually observed in OCFs; and the former means that a weaker ligand field is imposed by S^{2-} in comparison with that by O^{2-}. Nevertheless, Dy-SCFs still have the longest relaxation times and the highest energy barriers compared to other Dy-SMMs that contain a sulfur bridge.[153–155] This is because sulfur possesses a larger negative charge inside the fullerene, while the Dy–S bond length is also considerably shorter, thus giving rise to a strong ligand field.

The two isomers of $Dy_2S@C_{82}$ were further magnetically characterized at sub-Kelvin temperature, which shows broad hysteresis at 0.41 K with two clear QTM steps (one at zero field and the other at a certain field) in each case (Fig. 7c and d).[104] This allows a detailed analysis of the level crossing for different orientations in the presence of an applied magnetic field, providing precise information on the strength of Dy···Dy interactions in $Dy_2S@C_{82}$. The derived ΔE_{AFM-FM} values are 15.4 K and 7.3 K for C_s and C_{3v} isomers, respectively, which are in line with the results extracted from the fitting of temperature dependence of relaxation times as discussed above.[29] It is worthwhile to note that while the O^{2-} bridge facilitates an antiferromagnetically coupled system in Dy-OCFs, a ferromagnetically coupled ground state is found for Dy-SCFs. The sub-Kelvin temperatures enable the determination of relaxation times by DC demagnetization measurements. The QTM regime is thus achieved, rendering long relaxation times near 900 s and 3200 s for C_s and C_{3v} isomers. This QTM process is related to the situation where the two Dy^{3+} magnetic moments flip simultaneously as an entity.

Substituting one Dy^{3+} by a diamagnetic Sc^{3+} ion in these two isomers of $Dy_2S@C_{82}$ further leads to two SIMs.[105] Magnetic characterization of these $DyScS@C_{82}$ isomers shows an open magnetic hysteresis even at zero field at 2 K, indicating a quenched QTM effect compared to that of Dy-NCFs featuring a nearly closed hysteresis loop at zero field (Fig. 7e and f).[76] The hysteresis of $DyScS@C_{82}$ is open until 9 K in each case, where a fast field sweep rate of 10 mT s^{-1} is used. The bifurcation temperatures determined from ZFC/FC curves are both around 7.3 K. This better SMM performance of $DyScS@C_{82}$ than $Dy_2S@C_{82}$ suggests potential interest in future magnetic studies of $DyScO@C_{82}$ with an even stronger axial ligand field.[136]

4.1.5 Metal carbide clusterfullerenes (CCFs). Another type of clusterfullerenes isostructural and isoelectronic to OCFs and SCFs is metal carbide clusterfullerenes (CCFs) $M_2C_2@C_{2n}$ (M = rare earth metals; $2n$ = 68–108) featuring a C_2^{2-} bridging ligand.[45,48,156–159] CCFs are the second family of clusterfullerenes after NCFs, which was first discovered in 2001 by Wang *et al.* in $Sc_2C_2@D_{2d}(23)$-C_{84}.[160] Over the past two decades, an increasingly large number of CCFs have been synthesized with a rich variety of structures both for the encapsulated clusters and for the host fullerene cages. The interplay between the host and guest has been disclosed to show a structural transformation from a bent butterfly cluster shape in small cages to a linear geometry in large fullerenes thanks to the cage compression effect.[161] Despite the plethora of structural studies on CCFs with a C_2^{2-} bridge, one of the few CCF-SMMs that have been reported to date includes $Dy_2C_2@C_s(6)$-C_{82}.[29] This molecule exhibits similar SMM performance to $Dy_2S@C_s(6)$-C_{82} discussed above, showing a narrow magnetic hysteresis at 1.8 K which persists up to 3 K with a field sweep rate of 8.33 mT s^{-1}. AC susceptibility measurements reveal an effective barrier, corresponding to the exchange excited state, of 17.4 K in $Dy_2C_2@C_s(6)$-C_{82}, which is comparable to the value of 15.2 K

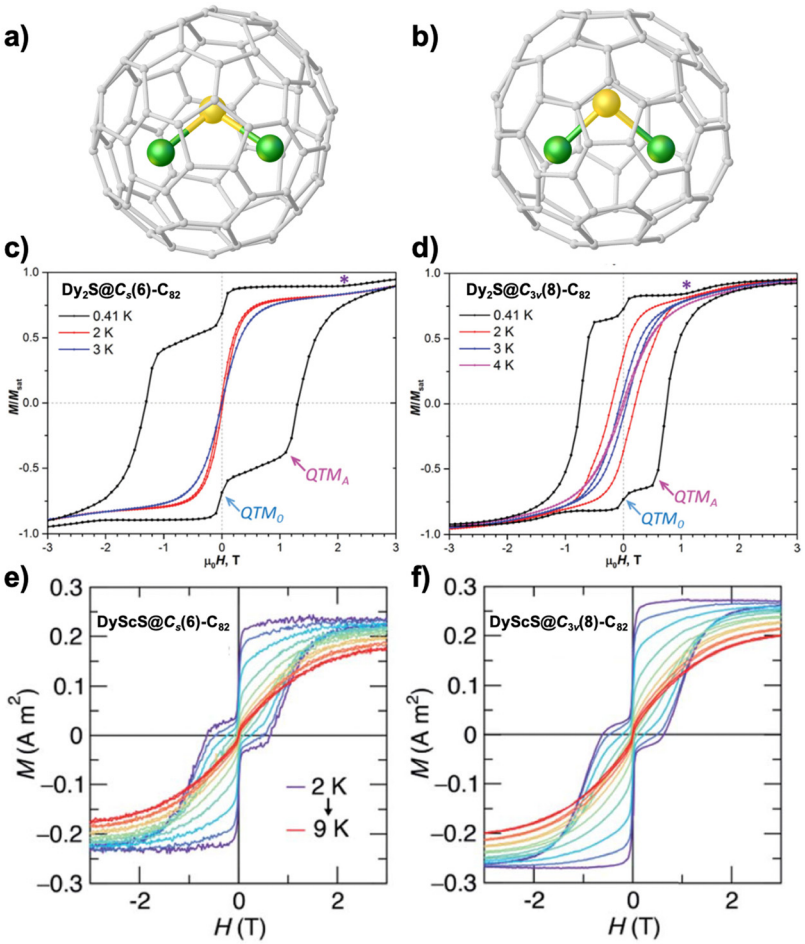

Fig. 7 Molecular structures of $Dy_2S@C_s(6)$-C_{82} (a) and $Dy_2S@C_{3v}(8)$-C_{82} (b). Magnetic hysteresis loops of $Dy_2S@C_s(6)$-C_{82} (c) and $Dy_2S@C_{3v}(8)$-C_{82} (d) at 0.41 K and compared to some higher-temperature curves recorded until the hysteresis is closed. Field sweep rates 2.9 mT s^{-1} for T = 2 K and above, and 3.3 mT s^{-1} for T = 0.41 K. QTM_0, QTM_A, and asterisk denote the features appearing because of the level crossing in Zeeman energies. Magnetic hysteresis loops of $DyScS@C_s(6)$-C_{82} (e) and $DyScS@C_{3v}(8)$-C_{82} (f) at 2–9 K with a sweep rate of 10 mT s^{-1}. Reproduced from (c) and (d) ref. 104 and (e) and (f) ref. 105.

determined for $Dy_2S@C_s(6)$-C_{82}. Note that inside the same $C_s(6)$-C_{82} cage, the two Dy^{3+} magnetic moments in Dy_2C_2 and Dy_2S are ferromagnetically coupled, whereas an antiferromagnetically coupled ground state is identified for Dy_2O.[102] Similar observations were found for the two isomers of $Dy_2C_2@C_{88}$ with cage symmetries of $C_s(32)$ and $D_2(35)$, which also show significantly narrower magnetic hysteresis loops compared to those of their Dy_2O counterparts.[103] Thus, a general conclusion can be drawn from the comparative studies that, given the same cage structure, OCFs have better SMM performance than SCFs and OCFs. This is very likely due to the stronger single-ion anisotropy and stronger superexchange interaction in the presence of an O^{2-} bridging ligand.

In addition to the C_2^{2-} bridging ligand, metal carbide containing a single C atom is also available within the fullerenes. This type of clusterfullerene was first synthesized by Popov *et al.* in $Lu_2TiC@I_h(7)$-C_{80} having a μ_3-carbide ligand and mimics the structure of $M_3N@C_{80}$ (M = rare earth metals) NCFs.[162] The tetravalent oxidation state of Ti gives rise to a Ti=C double bond in the former. As a result, both of these clusterfullerenes feature a cluster-to-cage six-electron transfer. Replacing the diamagnetic Lu^{3+} by Dy^{3+} leads to two dinuclear Dy-SMMs $Dy_2TiC@C_{80}$ with the cage symmetries of $I_h(7)$ and $D_{5h}(6)$ that are structurally characterized by spectroscopic methods.[107] The two isomers display similar hysteresis loops at 1.8 K. The hysteresis of the $I_h(7)$ isomer can be observed up to 3 K using 5 mT s^{-1} field sweep rate, showing a much weaker SMM performance compared to that of $Dy_2ScN@C_{80}$ ($T_{B,hys}$ = 7 K at 2.9 mT s^{-1} sweep rate), despite a stronger magnetic coupling found for $Dy_2TiC@C_{80}$.[95] This may be explained by a larger deviation of the orientation of the Dy magnetic moments from the Dy–C bond axes.[94] Adding one more carbon atom in the encapsulated cluster, $Dy_2TiC_2@C_{80}$ only exhibits a narrow hysteresis at 1.8 K. An SIM can also be constructed in DyYTiC@C_{80} that contains three different metals, with two being diamagnetic.[106] Similar to $DySc_2N@C_{80}$,[15] a butterfly-shaped hysteresis is observed for DyYTiC@C_{80} at 1.8 K, which is open up to 7 K at 2.9 mT s^{-1} sweep rate.

The trimetallic carbide can be further extended to a special case of $Dy_3C_2@C_{80}$ reported recently by Yang *et al.*, in which a

three-center single-electron metal–metal bond is disclosed within the triangular Dy_3 plane with very short Dy–Dy distances of ~3.4 Å.[163] A similar trimetallic single-electron bond was later unveiled in $Er_3C_2@C_{80}$.[164] This peculiar metal–metal bonding character is distinct from the situation in $Sc_3C_2@C_{80}$ where the unpaired electron is localized on the C_2 unit,[165–167] and thus is expected to evoke strong magnetic coupling between three Ln ions, which has just been confirmed very recently in a trinuclear gadolinium organometallic compound with a giant $S = 11$ ground state.[168]

4.2 Conventional EMFs

4.2.1 Monometallofullerenes (mono-EMFs). Coming back from clusterfullerenes with complex structures of the encapsulated species, we now focus on a simpler and conventional category of EMFs in which only metal atom(s) can be entrapped within the fullerene cage. To construct novel EMF-based SIMs, it is a natural idea to choose monometallofullerenes (mono-EMFs) encapsulating merely one metal ion inside a carbon cage. In fact, this simplest form of EMFs dates back to the discovery of empty fullerene and has a relatively high yield, in particular $M@C_{82}$ (M = rare earth metals).[39] The majority of mono-EMFs contain trivalent lanthanide ions, such as La^{3+}, Ce^{3+}, Pr^{3+}, Nd^{3+}, Gd^{3+}, Tb^{3+}, Dy^{3+}, Ho^{3+}, and Er^{3+}. Thus, the cage is paramagnetic in the presence of an unpaired electron. On the other hand, if an encapsulated Ln^{3+} possesses partially filled 4f orbitals, its intrinsic magnetic properties are of particular interest. In this context, the magnetic properties are more complex since it is inevitably affected by the magnetic coupling with the unpaired electron on the cage. Early-stage research studies on the magnetic properties of these mono-EMFs mainly aimed at the determination of their effective magnetic moments using a SQUID magnetometer, which is either extracted by the Curie–Weiss law or from the fitting isothermal magnetization with the Brillouin function.[169] For instance, the magnetization of $Gd@C_{82}$ measured at different temperatures gives an effective magnetic moment of 7.70 μ_B, which is slightly smaller than that of the free Gd^{3+} ion with an $^8S_{7/2}$ ground state (μ_{eff} = 7.94 μ_B) in the absence of orbital angular momentum (L) due to its half-filled 4f-shell.[170] This reduction of the magnetic moment is explained by the antiferromagnetic coupling between Gd^{3+} (S_{Gd} = 7/2) and the unpaired electron on the cage (S_{cage} = 1/2), and was later confirmed by high-frequency electron paramagnetic resonance (EPR) spectroscopy indicating an antiferromagnetically coupled $S = 3$ ground state.[171] Other lanthanide ions with nonvanishing orbital moment further complicate the determination of the magnetic moment of a mono-EMF.[172] Although a systematic SQUID study on a series of mono-EMF compounds $M@C_{82}$ (M = Gd, Ho, Tb, Dy, Er) suggests noticeable magnetic anisotropy for each molecule from isothermal magnetization, as a function of applied magnetic field divided by temperature (H/T), no magnetic hysteresis has been observed down to 1.8 K in all cases.[173]

It is reasonably expected that the unpaired electron on the cage of these trivalent mono-EMFs could be detrimental to their magnetic stability that intrinsically originated in the anisotropic Ln ions, such as Dy^{3+}. This can be rationalized by considering that on the one hand, the cage spin is weakly coupled with the encapsulated magnetic metal, which is sensitive to the subtle variations in the environment, such as lattice phonons and intermolecular interaction in a powder form. This strong molecular interaction is even able to induce dimerization of a relatively unstable $Y@C_s(6)$-C_{82} isomer in its cocrystal with Ni(OEP).[174] The harmful influence of the open-shell cage on the metal, on the other hand, is aggravated due to the fact that the charge and the associated spin are actually delocalized on the cage, and thus numerous cage-based molecular vibrations can easily affect the spin state of the whole molecule. Very often these vibrations are able to accelerate magnetic relaxation and need to be carefully engineered at molecular and atomic levels. In fact, mono-EMFs represent an ideal case in which the Ln ion is coordinated with only one rigid carbon cage ligand, thus resulting in an ultralow phonon density of state involving metal-based vibrations. Only three vibrational modes are present in mono-EMFs in which the metal ion oscillates along the *x*-, *y*- and *z*-axes.[83] This extraordinarily low-coordination environment, being inaccessible *via* conventional synthetic strategies since Ln ions always tend to have large coordination numbers, resembles the cases where single Ln atoms (Ho and Dy) are attached on graphene or metallic surfaces.[175–177] Thanks to the reduced spin-phonon coupling as a result of low coordination, these single-atom magnets display magnetic bistability at an atomic level despite the large strength difference of ligand fields imposed by distinct surfaces.

Extracted from the above analysis, mono-EMFs are a promising platform to design SMMs, yet it is crucial to quench the unpaired electron on the cage which can then be used as a diamagnetic matrix for the Ln ion, with the aim to protect the spin state against the influence from the open-shell carbon cage. Such a goal can be realized by encapsulating divalent metals, such as Eu^{2+}, Sm^{2+} and Yb^{2+}. While the latter possesses fully occupied f orbitals (f^{14}), Eu^{2+} has a half-filled f^7 configuration and thus is considered to be isotropic at its atomic origin but slightly anisotropic in real molecules.[178] Sm^{2+}, on the other hand, could be interesting from the magnetic point of view. ^{13}C NMR spectra also show changes in chemical shifts due to the paramagnetic lanthanide ion.[111,179,180] However, it is not anisotropic enough to induce SMM behaviors. Thus, one has to again resort to trivalent mono-EMFs employing conventional magnetic Ln ions such as Dy^{3+} and Tb^{3+}. In this context, a possible solution to quench the unpaired electron on the cage is exohedral functionalization *via* radical addition. This strategy can be achieved either by *in situ* derivatization during the arc-discharging process or by chemical reaction during extraction of the raw soot using organic solvents, affording covalent modifications of the cage with trifluoromethyl,[181,182] dichlorophenyl,[44,183–185] benzyl,[186,187] and other radical groups.[188,189] Not only mono-EMF derivatives have been reported based on the most popular C_{82} cages, but also various unstable fullerenes can be stabilized in this way, such as $La@C_{72}$-$C_6H_3Cl_2$ having a non-IPR cage and "missing" mono-EMFs like $M@C_{74}$ and $M@C_{70}$ (M = Y, La). The successful

syntheses of these otherwise unstable species evidence the stabilization effect induced by radical addition on the open-shell mono-EMFs. The closed-shell carbon cage obtained *via* this approach also leads to the activation of the luminescence of Er^{3+} in its mono-EMFs due to the enlarged optical band gap upon functionalization.[184]

An even more straightforward method to realize the closed-shell fullerene cage in mono-EMFs is *in situ* nitrogen substitution of the pristine carbon cage, thus producing an azafullerene. Indeed, the idea of azafullerene was first achieved in $(C_{59}N)_2$ dimers[190] and was later applied in mono-EMF La@C_{81}N together with the synthesis of the pristine La@C_{82}.[191] However, this observation of monometallic azafullerene was only suggested by mass spectroscopy. The precise confirmation of its structure had long remained an open question over decades. Recently, such an approach towards a nitrogen-substituted mono-EMF with a closed-shell fullerene cage has been accomplished in La@C_{81}N which is derived from the pristine C_{3v}-C_{82} cage.[42] The closed-shell nature of the azafullerene cage is verified by EPR spectroscopy showing an EPR-silent behavior for La@C_{81}N.

Introducing Dy^{3+} to design a novel SMM, an azafullerene compound Dy@C_{81}N was reported by Coronado *et al.* very recently based upon C_s-C_{82}.[16] In the structure of the mono-EMF Dy@C_{81}N, the Dy^{3+} ion is asymmetrically coordinated by one side to a hexagonal carbon ring on the cage, while lacking any nonmetal ligand or negative charge on the other side towards the center of the cage. This extraordinary low coordination results in a very weak ligand field causing a small overall splitting ($\sim$230 cm^{-1}) of the $^6H_{15/2}$ ground multiplet for Dy^{3+}, similar to that found for a single Dy atom attached on graphene with the Dy-C_6 ring coordination.[177] *Ab initio* calculations not only confirm the weak ligand field, but also indicate a mixed ground state for Dy^{3+}. This special feature of single-ion anisotropy, often associated with weak SMM properties,[192] is in striking contrast to the situation in all high-performance Dy-SMMs, where a pure $m_J = \pm 15/2$ ground Kramers doublet and a strongly axial field are always required. Despite this, the DC magnetic characterization of Dy@C_{81}N shows slow magnetic relaxation (with $\tau > 40$ s) up to 60 K (Fig. 8c). Analysis of the temperature dependence of the relaxation times reveals a temperature-independent QTM process below 17 K and a thermally activated Raman-like mechanism at high temperatures. The 100-s blocking temperature $T_{B,100s}$, extracted from the fitting of the $\tau(T^{-1})$ curve, is determined as 45 K. This

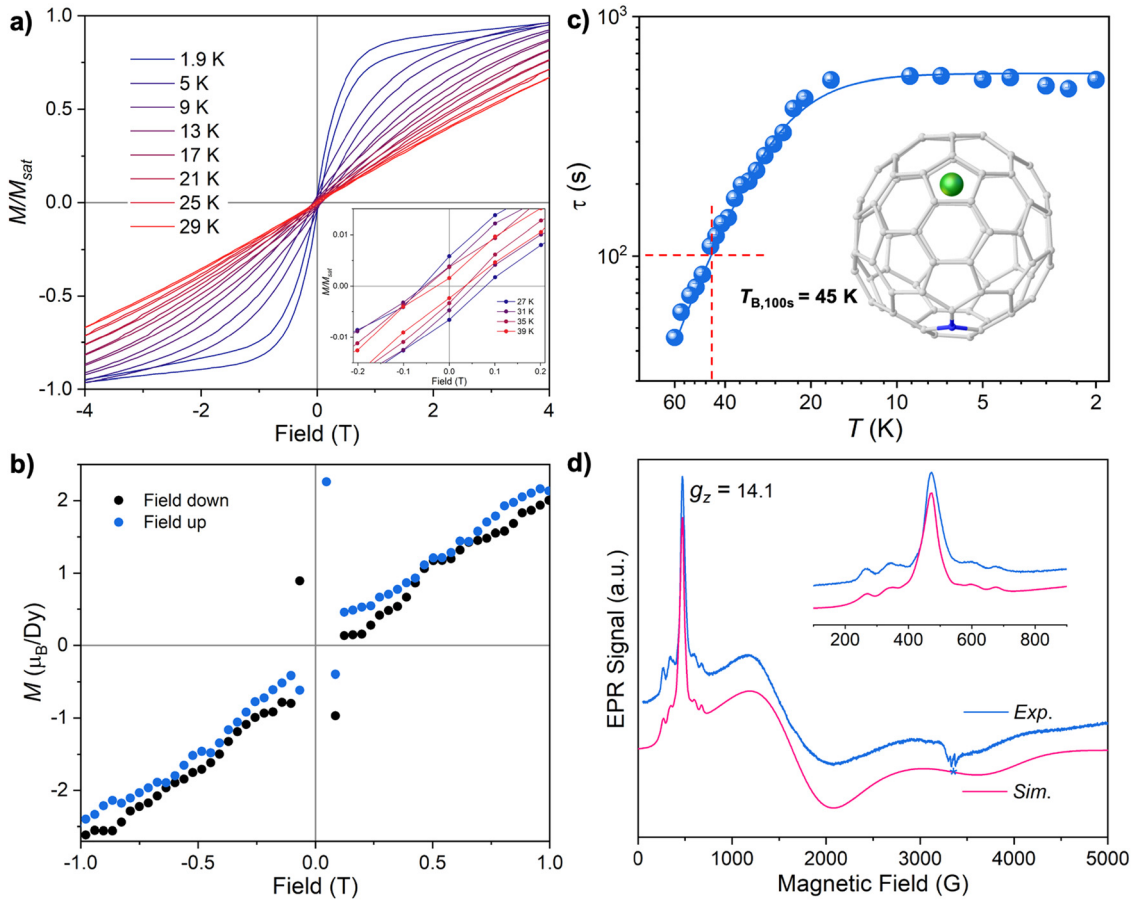

Fig. 8 (a) Magnetic hysteresis loops for Dy@C_{81}N at 1.9–39 K using SQUID magnetometry with a field sweep rate of 3.5 mT s^{-1}. (b) Magnetic hysteresis for Dy@C_{81}N at 5 K recorded by using the XMCD technique. (c) Temperature-dependence of magnetization relaxation times for Dy@C_{81}N and the determination of its blocking temperature $T_{B,100s}$ = 45 K. The inset shows its molecular structure. (d) Experimental and simulated EPR spectra of Dy@C_{81}N in a toluene solution at 10 K. The inset illustrates the hyperfine structures. Reproduced from ref. 16.

represents a record value among all known EMF-SMMs reported to date, being only behind the cyclopentadienyl (Cp)-based lanthanide complexes.[11,12,23,193–195] The fast drop of τ due to an Orbach process normally detected for high-performance SMMs is not observed in $Dy@C_{81}N$ even up to 60 K. The lack of the Orbach process was reported before in $DySc_2N@C_{80}$ as discussed above,[64] which suggests a weak spin-phonon coupling in this type of EMF-SIMs. Among them, $Dy@C_{81}N$ is even cleaner in terms of relaxation through the phonon bath because it has a minimal number (three) of vibrational modes that can couple to the spin states.

As shown in Fig. 8a, magnetic hysteresis of $Dy@C_{81}N$ was recorded up to 39 K at a magnetic field sweep rate of 3.5 mT s^{-1}, and further persists until 60 K using a faster sweep rate of 100 Oe s^{-1}. Surprisingly, the hysteresis is thin even at the lowest measured temperature of 1.9 K, *i.e.*, with weak coercive field and magnetization remanence. This very special hysteretic feature is further confirmed by element-specific XMCD measurement at the Dy $M_{4,5}$ edge (Fig. 8b). The direct process in the presence of a strong applied magnetic field is likely responsible for the usual reduction of magnetic hysteresis due to the strongly mixed ground doublet of Dy^{3+} in the low-coordination environment, whose Zeeman energy is sensitive to the distortion caused by coupling of long-range vibrations to the spin states. The mixing nature of the ground doublet in $Dy@C_{81}N$ also leads to the observation of the EPR signal at 10 K using a conventional X-band spectrometer (Fig. 8d). A strong hyperfine coupling is evidenced for $Dy@C_{81}N$ between the electron spin and the nuclear spin within Dy^{3+}, in which the hyperfine constant A_z = 1600 MHz is determined for ^{163}Dy. This information extracted from the EPR spectrum, in contrast, is elusive for other Dy-based SMMs due to the fast spin–lattice relaxation arising from the strong spin–orbit coupling in Dy^{3+}, which may be ascribed to the well-protected Dy^{3+} spin from the destabilizing interactions with phonons in $Dy@C_{81}N$ at zero or finite magnetic fields where QTM dominates. Taking advantage of the hyperfine structures, it could be feasible to fine-tune magnetic relaxation upon applying magnetic fields, as already shown in SMMs based on Ho^{3+} and Tb^{3+}.[196,197]

4.2.2 Dimetallofullerenes (di-EMFs). Apart from the single-ion system, introducing another metal ion complicates the electronic and magnetic properties of the molecule. As can be inferred from the above discussions on clusterfullerenes behaving as dinuclear SMMs, the design strategy towards better SMM performance lies in enhancing the magnetic coupling between two Ln ions. Although some success has been achieved by utilizing strong bridging ligands to induce large ligand field splitting and favor superexchange interactions, the coupling is still not strong enough to preserve magnetic bistability up to practically high temperatures (for example, above the liquid nitrogen temperature of 77 K) against relaxation. This is majorly owing to the well-shielded 4f electrons that are not amenable to interacting with other magnetic metal ions.

The goal of strong magnetic coupling can be realized by introducing a N_2^{3-} radical bridge between two Ln^{3+} ions in an organometallic compound due to the rather diffuse unpaired electron from the N_2^{3-} bridge.[198] Such diffuse electron spin is able to strongly interact with the 4f electrons of Ln^{3+}, thus giving rise to magnetic hysteresis up to 8.3 K at a sweep rate of 80 mT s^{-1} when the high-anisotropy Dy^{3+} is incorporated. Better SMM properties are obtained in Tb^{3+}–N_2^{3-}–Tb^{3+} three-center systems, among which a $T_{B,100s}$ value of 20 K is determined by employing Cp-based ligands together with the radical bridge.[199,200] An advantageous consequence of the strong magnetic coupling is a broad hysteresis with a large coercive field thanks to the effective quenching of QTM at zero field. This design strategy of radical-bridged dilanthanide compounds as high-performance SMMs has been extensively studied, featuring strong antiferromagnetic or ferromagnetic coupling between the radical and Ln^{3+}.[201,202]

Taking advantage of fullerene cages with confined nanospace, dimetallofullerenes (di-EMFs) are of particular interest for magnetic studies aiming at direct metal–metal interactions and thus strong magnetic coupling without any nonmetal ligand between the two metals. This ligand-unsupported metal–metal bond can be stabilized in $M_2@C_{82}$ (M = Sc, Y, Er, Lu), in which each metal adopts the divalent oxidation state, offering one electron to form a σ bond, and as a result the most popular tetravalent C_{82} cages are favored.[203–205] For $I_h(7)$-C_{80} with exceptional stability in a 6-charged state, on the other hand, di-EMFs were initially expected to contain a rare-earth metal with the high oxidation state (+3), as exemplified in $La_2@C_{80}$. However, the valence state of the metal atom in di-EMFs is in fact determined by its $ns^2(n-1)d^1$ to $ns^1(n-1)d^2$ excitation energy that corresponds to the metal–metal bonding orbital.[17,203] The relation of this energy to the cage molecular orbitals (MOs) is then crucial to govern the electronic structure of a di-EMF. A peculiar triplet ground state is thus found in theory for $M_2@C_{80}$ (M = Sc, Y, Gd, Er, Lu) resulting from the half filling of the low-lying bonding MOs of the M_2 dimer to form a single-electron metal–metal bond (SEMB), while the cage possesses another unpaired electron.[206,207] Under this circumstance, M_2 transfers five electrons to the cage, leaving each metal with a formal charge of +2.5. This is akin to the situation of radical-bridged dilanthanide complexes as mentioned above, but with much structural simplicity in which the unpaired electron is shared solely by two metals, instead of being localized on the bridging ligand, affording an M^{3+}–e–M^{3+} three-center system.

Preceding the in-depth understanding of the SEMB, such a bonding peculiarity was realized in a stable dimetallic azafullerene $M_2@C_{79}N$ (M = Y, Tb) by Dorn *et al.*, which is derived from the unstable $M_2@C_{80}$ by quenching its unpaired electron on the cage *via* nitrogen substitution.[41] The singly-occupied metal–metal bonding molecular orbital (SOMO) is low-lying below the highest occupied MO (HOMO), thus leading to the stabilization of this open-shell molecule. Despite having a SEMB inside the cage, crystallographic study of $Tb_2@C_{79}N$ shows a long Tb–Tb distance of 3.902 Å, even exceeding the sum of the covalent radius of two Tb atoms (3.88 Å), which is likely attributed to the strong Coulombic repulsion within the Tb_2^{5+} dimer. The open-shell nature is better understood

in an $S = 1/2$ species, $Y_2@C_{79}N$, which enables the detection of single electron spin using EPR spectroscopy. The signal is split into three peaks with an intensity ratio of 1 : 2 : 1 arising from the hyperfine interaction of the single electron with the $I = 1/2$ ^{89}Y nuclear spin. A very large hyperfine coupling constant of 81 G (with the isotropic g factor of 1.9740 measured at room temperature) is observed for $Y_2@C_{79}N$. In comparison, the value is only 3.1 G in a radical-bridged diyttrium compound with a Y^{3+}–N_2^{3-}–Y^{3+} three-center system. This indicates the substantially stronger interaction between the unpaired electron and metals in di-EMFs containing SEMBs without any nonmetal bridging ligand, which can be evidenced by the sharing of the SOMO by the two metals in $Y_2@C_{79}N$ whereas a SOMO mainly localized on the N_2 unit is found for the radical-bridged diyttrium compound.[208]

The same group later also synthesized $Gd_2@C_{79}N$, which was characterized by X- and W-band EPR spectroscopy to show a giant spin ground state of $S = 15/2$, as a result of strong ferromagnetic coupling between the $S = 1/2$ unpaired electron and two Gd^{3+} ions with $S = 7/2$.[43] *Ab initio* studies of the isoelectronic $[Gd_2@C_{80}]^-$ anion suggest that this ferromagnetic coupling arises from Hund's rule, but not from the double exchange mechanism conventionally observed in dinuclear mixed-valence transition-metal compounds.[209] The exceptional stability of these SEMB-containing open-shell di-EMFs comes from the low-lying metal–metal bonding orbital as discussed before. Even for $La_2@C_{80}$ with a relatively high-energy La_2 valence MO, SEMBs can still be stabilized by accepting one electron in such an MO upon reduction, radical addition and light-induced charge separation in an electron donor–acceptor conjugate.[210–213] This is because that the La_2 valence MO becomes the lowest unoccupied MO (LUMO) of the whole molecule. The existence of SEMBs in these cases can be then verified by EPR spectroscopy to show strong hyperfine splitting in the spectra due to the ^{139}La nucleus.

The possibility of utilizing SEMB-containing di-EMFs towards high-performance SMMs was explored theoretically by Rajaraman *et al.*[214] Broken-symmetry (BS) DFT studies of $Gd_2@C_{79}N$ reveal a very strong ferromagnetic exchange between Gd and the unpaired electron with the coupling constant j_{Gd-e} (in the $-2j_{Gd-e}S_{Gd}S_e$ convention) in the order of 200 cm^{-1}. *Ab initio* calculations performed on the $Dy_2@C_{79}N$ molecule suggest that the exceptionally strong Dy-*e* magnetic coupling not only quenches QTM but can also increase the effective barrier of magnetization reversal. Thus, $Dy_2@C_{79}N$ is anticipated to be a high-performance SMM. This idea was later realized by Popov *et al.* in a benzyl monoadduct, instead of substituting one carbon atom by nitrogen on the cage, of $Dy_2@C_{80}$ to quench the unpaired cage radical so as to obtain air-stable $Dy_2@C_{80}(CH_2Ph)$ containing a SEMB.[18] In this molecule, the magnetic moments of two Dy^{3+} and the unpaired electron align collinearly to form a single spin unit of 21 μ_B. The spin Hamiltonian of this three-center system should be defined as follows derived from eqn (3) in absence of magnetic field

$$\hat{H}_{spin} = \hat{H}_{LF1} + \hat{H}_{LF2} - 2j_{Ln-e}(\hat{J}_1 S_e + \hat{J}_2 S_e) - 2j_{12}\hat{J}_1\hat{J}_2 \quad (5)$$

where the first two terms are the single-ion anisotropy of two Dy sites; the third term describes the magnetic coupling between single electrons and Dy considering an equal j_{Dy-e} for the two metals; and the last term denotes the coupling between two Dy magnetic moments. Notably, the last term can be safely neglected thanks to the overwhelmingly strong Dy-*e* magnetic coupling over Dy–Dy 4f–4f interaction. The giant Dy-*e* ferromagnetic coupling is confirmed by the fitting of magnetic susceptibility and magnetic magnetization curves, which jointly yield a large j_{Dy-e} of 32 cm^{-1}. This results in the exchange-excited state with the energy that essentially matches with the effective barrier U_{eff} of 613 K extracted from an Orbach relaxation process, in which the spin of one Dy center is flipped (Fig. 9g). Remarkably, QTM is efficiently quenched by the giant magnetic coupling interaction, and a broad hysteresis loop is thus observed at 2 K which closes gradually until 22 K with 2.9 mT s^{-1} field sweep rate (Fig. 9d). A 100-s blocking temperature $T_{B,100s}$ of 18 K is obtained for $Dy_2@C_{80}(CH_2Ph)$ from the temperature dependence of relaxation time, while a bifurcation temperature $T_{B,ZFC}$ of 21.9 K is determined (Fig. 9a). Very similar results were later found for $Dy_2@C_{79}N$, which shows a slightly larger U_{eff} of 669 K but a lower $T_{B,100s}$ of 12 K (Table 2).[22] The weaker SMM performance in $Dy_2@C_{79}N$ is due to the faster zero-field QTM at low temperatures, which likely stems from the structural difference in these congeners. In this context, the functional group attached on the cage of $Dy_2@C_{80}(CH_2Ph)$ shall lead to a larger intermolecular distance in a powder sample and thus suppresses the QTM effect.

Using the cage derivatization method of benzyl radical addition, a series of air-stable $M_2@C_{80}(CH_2Ph)$ ($M_2 = Y_2$, Gd_2, Tb_2, Dy_2, Ho_2, Er_2, TbY, TbGd) compounds containing SEMBs have been synthesized.[19] Among them, $Tb_2@C_{80}(CH_2Ph)$ exhibits a gigantic coercive field of 8.2 T at 5 K extracted from its hysteresis loops, which can be recorded without closing up to 27 K at a field sweep rate of 9.5 mT s^{-1} (Fig. 9e). Analysis of the temperature-dependence of magnetic relaxation time gives a high $T_{B,100s}$ of 25.2 K and a large U_{eff} of 799 K (Fig. 9h). Meanwhile, $T_{B,ZFC}$ of 28.9 K can be extracted from the ZFC/FC curves (Fig. 9b). All these SMM metrics are significantly superior to those of its Dy counterpart, and are similar to the situation of N_2^{3-}-radical-bridged dilanthanide compounds in which Tb is also better than Dy.[198,200] In contrast to the worse Tb-SIMs often observed in organometallic compounds, the exceptional SMM behaviors for $Tb_2@C_{80}(CH_2Ph)$ lie in the Kramers Tb^{3+}–e–Tb^{3+} three-center system, instead of the single non-Kramers Tb^{3+} ion, in such a way that QTM within the degenerate ground doublet of a strongly coupled system is essentially forbidden. Examining the magnetic properties of di-EMFs containing other anisotropic Ln ions reveals much weaker SMMs for Ho_2 and Er_2 cases. The former shows slow magnetization relaxation below 1 s with non-colinear alignment of the three magnetic moments, while the latter only exhibits field-induced AC signals due to the easy-plane anisotropy of the Er spin. Weaker SMM performance is also observed for the mixed-metal TbGd and TbY compounds, where the blocking temperatures ($T_{B,ZFC}$) defined by ZFC/FC

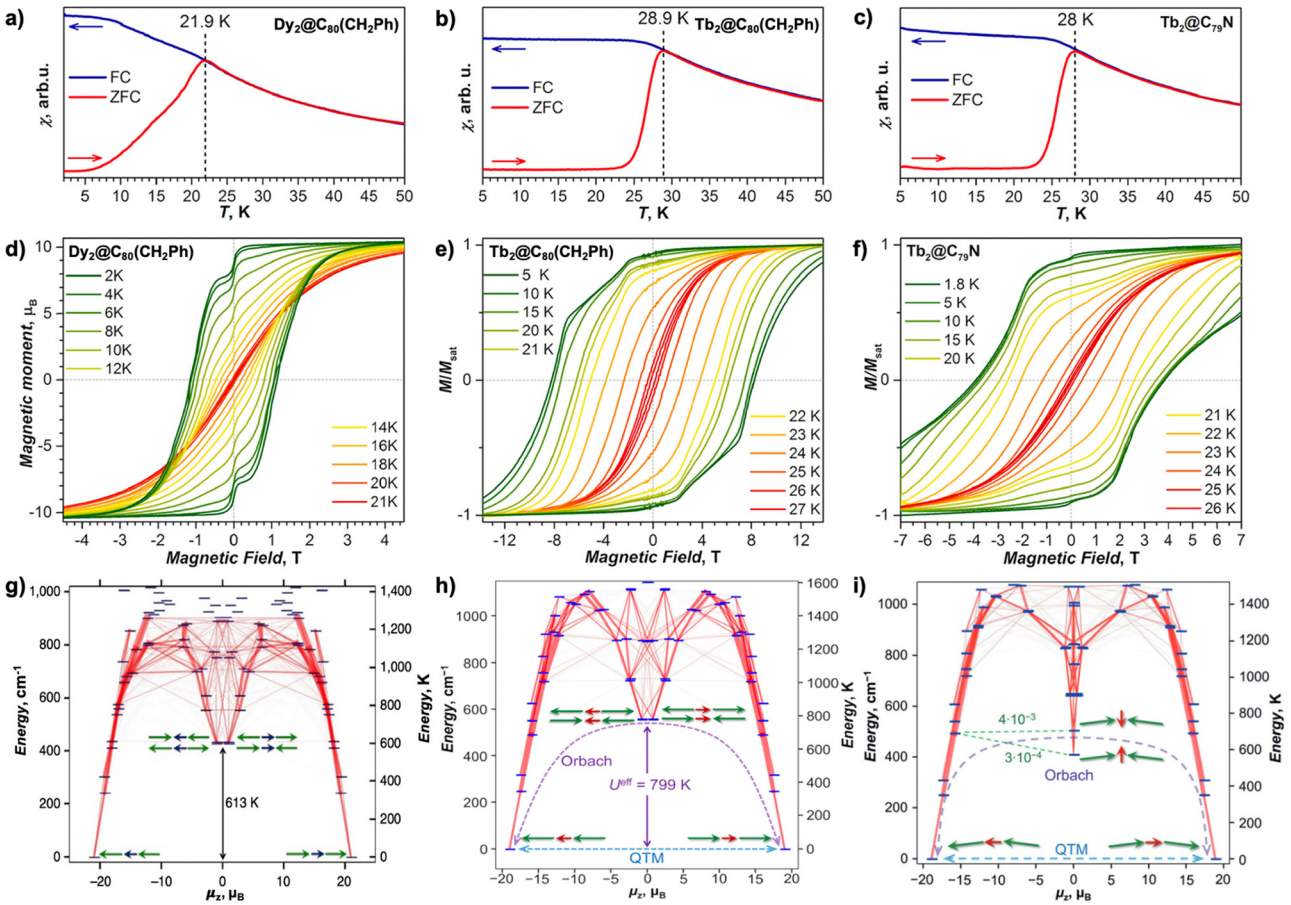

Fig. 9 (a)–(c) ZFC/FC curves of $Dy_2@C_{80}(CH_2Ph)$ (a), $Tb_2@C_{80}(CH_2Ph)$ (b), and $Tb_2@C_{79}N$ (c). The magnetic field was 0.2–0.3 T, and the temperature sweep rate was 5 K min^{-1}. (d)–(f) Magnetic hysteresis of $Dy_2@C_{80}(CH_2Ph)$ (d), $Tb_2@C_{80}(CH_2Ph)$ (e), and $Tb_2@C_{79}N$ (f). The magnetic field sweep rate was 2.9 mT s^{-1} in (d) and (f) and 9.5 mT s^{-1} in (e). (g)–(i) Low-energy part of the spectra of $Dy_2@C_{80}(CH_2Ph)$ (g), $Tb_2@C_{80}(CH_2Ph)$ (h), and $Tb_2@C_{79}N$ (i), using the effective spin Hamiltonian in eqn (5), with transition probabilities visualized as lines of different thickness (thicker lines correspond to higher probabilities), the *x* axis is the projection of magnetic moment upon the main anisotropy axis, μ_z. A schematic description of the spin alignment in the ground state and exchange-excited states is also shown (Dy and Tb, green arrows; single electron spin, dark blue and red arrows). Reproduced with permission from (a)–(f) ref. 17, (g) ref. 18, (h) ref. 19 and (i) ref. 21.

Table 2 An exhaustive list of conventional EMF-SMMs reported to date

Type	EMF	$T_{B,100s}$ [K]	$T_{B,hys}$[b] [K] (dH/dt) [mT s^{-1}]	$T_{B,ZFC}$[c] [K] (dT/dt) [K min^{-1}]	U_{eff} [K]	j_{Ln-e} [cm^{-1}]	Ref.
Mono-EMF	$Dy@C_s(6)$-$C_{81}N$	45	39 (3.5)/60 (10)	69 (1)	—	—	16
Di-EMFs	$Dy_2@C_{80}(CH_2Ph)$	18	22 (2.9)	21.9 (5)	613	32	18
	$Dy_2@C_{79}N$	12	24 (20)	21 (3)	669	32	22
	$Tb_2@C_{79}N$	24	26 (2.9)	28 (5)	757	45	21
	$Tb_2@C_{80}(CH_2Ph)$	25.2	27 (9.5)	28.9 (5)	799	55	19
	$Tb_2@C_{80}(CF_3)$	25	26 (2.9)	28.5 (5)	801	—	20
	$Tb_2@C_{80}(CH_2Ph)(pyr_2)$	26.6	28 (2.9)	30.3 (5)	725	—	26
	$Ho_2@C_{80}(CH_2Ph)$	—	—	—	334	40	19
	$Er_2@C_{80}(CH_2Ph)$[a]	—	—	—	—	20	19
	$TbGd@C_{80}(CH_2Ph)$	—	—	14.4 (5)	—	—	19
	$TbY@C_{80}(CH_2Ph)$	—	5 (2.9)	5 (5)	—	35	19
	$Nd_2@C_{80}(CF_3)$[a]	—	—	—	—	—	217
	$Gd_2@C_{79}N$[a]	—	—	—	6.5	175/170	53 and 218
	$DyEr@C_{3v}(8)$-C_{82}	—	3 (33)	5 (3)	6.4	—	226

[a] Field-induced SMMs. [b] The value in the bracket indicates the field sweep rate (mT s^{-1}) used to record hysteresis loops. [c] The value in the bracket indicates the temperature sweep rate (K min^{-1}) used to record ZFC/FC curves.

measurements are 14 K and 5 K, respectively. It is thus demonstrated that the coupling of the single Ln spin to the electron spin of the SEMB is not sufficiently strong, and the involvement of two anisotropic Ln ions is necessary to

construct a remarkably high-performance SMM. When diamagnetic Y^{3+} and Sc^{3+} are introduced into $M_2@C_{80}(CH_2Ph)$ with an M^{3+}–e–M^{3+} three-center system, strong hyperfine splitting can be observed in the presence of ^{89}Y and ^{45}Sc nuclear spins, giving rise to fully-resolved EPR spectra with well-defined transitions between specific electron-nuclear quantum states.[215,216]

The extraordinary SMM performance of Tb-based di-EMF was then further realized in $Tb_2@C_{79}N$ using an azafullerene to obtain a closed-shell fullerene cage.[21] Magnetic characterization of $Tb_2@C_{79}N$ indicates similar results yet a slightly weaker SMM in comparison with $Tb_2@C_{80}(CH_2Ph)$. Specifically, $Tb_2@C_{79}N$ exhibits a slightly lower $T_{B,100s}$ of 24 K and U_{eff} of 757 K (Fig. 9i). Its hysteresis, albeit broad, has a weaker coercive field of 3.8 T between 1.8 and 10 K, which then closes down up to 26 K at 2.9 mT s^{-1} sweep rate (Fig. 9f). Similarly, a slightly lower bifurcation temperature $T_{B,ZFC}$ of 28 K is determined (Fig. 9c). This difference in magnetic properties between di-EMFs with the carbon cage modified by *N*-substitution and by benzyl addition is consistent with the above discussion on the Dy counterparts. More importantly, *ab initio* calculations demonstrate that the magnetic moments of Tb ions in $Tb_2@C_{79}N$ are tilted from the Tb–Tb bond by approximately 7°. This slight non-collinearity of the Tb quantization axes may be caused by the strong variation of the electrostatic potential distribution upon replacing one carbon atom by nitrogen, and could contribute to the change of magnetic behaviors. Apart from nitrogen substitution and exohedral benzyl addition on the cage, trifluoromethylation of di-EMF anions was then demonstrated to be a highly selective alternative route to this kind of structures featuring a ferromagnetically coupled M^{3+}–e–M^{3+} three-center system.[20] Through this method, $Tb_2@C_{80}(CF_3)$ can be readily synthesized as the main reaction product, which behaves as a strong SMM with a broad magnetic hysteresis, a high $T_{B,100s}$ of 24 K and an effective barrier U_{eff} of 801 K. Very recently, this method has been applied to stabilize SEMBs within an early lanthanide dimer Nd_2 inside the $I_h(7)$-C_{80} and $D_{5h}(6)$-C_{80} cages, making $Nd_2@C_{80}(CF_3)$ based on the $I_h(7)$ isomer a field-induced SMM showing slow relaxation below 3 K.[217]

The magnetic coupling situation in di-EMFs containing SEMBs can be better understood in a Gd^{3+}–e–Gd^{3+} system incorporating two nearly isotropic Gd^{3+} ions without spin–orbit coupling. Fitting the magnetic susceptibility and magnetization curves of $Gd_2@C_{79}N$ clearly reveals a giant ferromagnetic Gd–e coupling with a coupling constant of 160–180 cm^{-1}.[53,218] Note that this value is comparable to the result predicted by BS-DFT calculations ($\sim$200 cm^{-1})[214] and greatly surpasses the antiferromagnetic coupling constant (-27 cm^{-1}) obtained in the N_2^{3-}-radical-bridged digadolinium compound.[198] Such a strong magnetic coupling enables a giant total spin of S = 15/2 for the whole molecule. This high-spin ground state is well separated from the excited states and can be retained even at room temperature. Surprisingly, low temperature AC measurements also disclose that $Gd_2@C_{79}N$ is a field-induced SMM showing slow relaxation of magnetization with the τ values at the millisecond scale at low temperatures below 3 K.[218]

The isotropic nature of the half-filled Gd^{3+} ion precludes the possibility to design a high-performance SMM based on it. This isotropy in the free Gd^{3+} ion is lifted in a coordination compound in the presence of ligand fields, which is ascribed to the mixing of the excited state with the ground multiplet $^8S_{7/2}$. Note that the splitting of the ground multiplet in this case is very small (in the order of 1 cm^{-1}) compared to that for other anisotropic Ln-based compounds in the same coordination environment (normally 100–1000 cm^{-1}), but matches with the energy scale of conventional X-band EPR ($\sim$0.3 cm^{-1}), which can then be used as a powerful tool to probe the spin states of compounds having Gd^{3+}. Despite the fragile magnetic bistability in a slightly anisotropic Gd-SMM, superposition between their two spin states could be created utilizing the pulsed EPR technique, giving rise to a spin qubit candidate showing a quantum coherence effect that could pave a way for quantum information processing.[219–222] Indeed, $Gd_2@C_{79}N$ was found to be an excellent high-spin qubit with microsecond-scale long coherence time at 5 K.[53] A more intriguing feature of this molecule lies in its well-defined 16-fold spin sublevels derived from an S = 15/2 high-spin ground state. This allows coherent manipulation of the arbitrary superposition state between each adjacent level pair in a periodic manner, resulting in diverse Rabi oscillations performed at different applied magnetic fields. $Gd_2@C_{79}N$ thus represents the largest-spin molecule that possesses Rabi oscillations reported so far. Aiming at a step forward using SMMs in quantum information technologies, the non-equidistant energy levels and long coherence times in the high-spin $Gd_2@C_{79}N$ fulfill the requirements of Grover's searching algorithm exploiting multi-levels of the anisotropic SMMs,[223] which has been realized on the nuclear spin of a Tb-SMM.[224]

The appealing magnetic properties in these SEMB-containing di-EMFs further stimulated the synthesis of strongly coupled dilanthanide organometallic compounds $(Cp^{iPr5})_2Ln_2I_3$ (Ln = Dy, Tb, Gd) directed at high-performance SMMs.[23] By employing two Cp-based ligands as a source of strong axial ligand fields and three I^- anions as bridging ligands, very strong SEMBs are constructed, giving rise to a ferromagnetically coupled high-spin ground state. These features jointly result in an enormous coercive field with a lower bound of 14 T in $(Cp^{iPr5})_2Dy_2I_3$ at 60 K, which surpasses even commercial magnets. Analysis of its relaxation times show a record-high $T_{B,100s}$ of 72 K, while this value is 65 K for the Tb congener. As a result of strong coupling, their effective barriers U_{eff} are determined to be as high as 2347 K and 1990 K, respectively. The better SMM performance, compared to that of di-EMFs with the same Ln^{3+}–e–Ln^{3+} three-center system (Ln = Tb, Dy) derived from the pristine $Ln_2@C_{80}$, originates in the stronger magnetic coupling in $(Cp^{iPr5})_2Ln_2I_3$. Fitting the variable-temperature magnetic susceptibility curve of the Gd case using the three-center model gives a giant Gd–e coupling constant of j_{Gd-e} = 389 cm^{-1}, more than twice the value of 175 cm^{-1} determined for $Gd_2@C_{79}N$.[53] This strong SEMB can also be evidenced from the short Ln–Ln distances in $(Cp^{iPr5})_2Ln_2I_3$ that are within the sum of covalent radii for each metal atom. In contrast,

substantially longer Ln–Ln distances are found for di-EMFs in the presence of strong Coulombic repulsion and metal–cage interactions that tend to separate the two Ln ions.

Extracted from the above comparative analysis, enhancing magnetic coupling in SEMB-containing di-EMFs is key to further improve their SMM properties. Since the previously discussed species are all based on $I_h(7)$-C_{80}, it seems inevitable to alter the cage structure to achieve this goal. In this context, finding a much smaller cage is a logical next step to enforce close contact of the two encapsulated metals and overcome Coulombic repulsion by the confinement effect. This idea was confirmed theoretically in an actinide di-EMF that direct overlap of 5f orbitals may be realized to form U≡U triple bonds in $U_2@C_{60}$,[227] while the short U–U distance is not observed in $U_2@C_{80}$ due to the strong metal–cage interactions.[228] Similar to $Ln_2@C_{79}N$ (Ln = Tb, Dy, Gd) that are of particular interest to molecular magnetism, $Ln_2@C_{59}N$ has been computed to show strong SEMBs.[229] *Ab initio* calculations yield a large Gd–e coupling constant of j_{Gd-e} = 434.8 cm^{-1} that is two times larger than the value determined for $Gd_2@C_{79}N$. Very high effective barriers U_{eff} are also predicted with values of 1702 and 2160 K for Dy and Tb cases, respectively, comparable to the current record determined in $(Cp^{iPr5})_2Gd_2I_3$.[23]

Although these theoretical studies point out a promising future direction, synthesizing di-EMFs with such a small cage based on C_{60} is not feasible at the current stage of research. By slightly varying the cage size from C_{80}, it has been shown that a SEMB may also be formed in $Er_2@C_{3v}(8)$-C_{82} by electrochemically manipulating the Er–Er bonding orbital.[151] Similarly, two isomers of DyEr@C_{82} with $C_{3v}(8)$ and $C_s(6)$ cage symmetries were reported, exhibiting cage-dependent magnetic and photoluminescent properties.[226] Magnetic characterization studies indicate that DyEr@$C_{3v}(8)$-C_{82} is an SMM with a thin hysteresis which closes below 3 K at a sweep rate of 33 mT s^{-1}, while DyEr@$C_s(6)$-C_{82} is a paramagnet. Theoretical studies suggest the likely presence of SEMBs in these cases and consequently open-shell cage structures.

Very recently, Yang *et al.* have made a step forward towards the stabilization of SEMBs inside various pristine cages without the need for nitrogen substitution or chemical derivatization.[225] This is accomplished by introducing a transition metal Ti in conjunction with La to form a heterometallic LaTi dimer inside the $D_{3h}(5)$-C_{78}, $I_h(7)$-C_{80}, $D_{5h}(6)$-C_{80} and $C_{2v}(9)$-C_{82} carbon cages, each of which has a formal 6-charged state. After transferring six electrons to the cage, there is one unpaired electron left within the LaTi dimer, creating a SEMB. The La–Ti distances can be largely varied from 4.31 to 3.97 Å upon increasing the cage size from C_{78} to C_{82} (Fig. 10a). This uncommon anticorrelation between the cage size and the La–Ti distance suggests that the metal–cage interaction is instead the dominating effect in determining the strength of a SEMB inside medium-size fullerene cages. As shown in Fig. 10b, DFT calculations confirm the existence of SEMBs in each case featuring a metal–metal bonding SOMO, despite the long La–Ti separation due to the much smaller Ti atom, and its increased strength is verified by the gradual shift in the accumulation of electron density towards the center of the LaTi dimer. Interestingly, EPR spectroscopy shows a consecutive enhancement of hyperfine coupling between the unpaired electron and La following the decrease of La–Ti distance (Fig. 10c and d). The strongest coupling is thus found in LaTi@$C_{2v}(9)$-C_{82}. By changing metal–metal interactions and magnetic coupling, therefore, this proof-of-concept study offers a possibility to design SMMs, based on other anisotropic lanthanide metals such as Dy and Tb, which show improved performance in comparison with di-EMFs employing a modified $I_h(7)$-C_{80} cage.

5. Assemblies of EMF-SMMs

The practical use of SMMs in information storage requires a well-defined molecular array that allows single molecules of interest to be precisely addressed. To this end, SMMs are required at first to be processed into a molecular assembly, such as a 2D monolayer on a substrate, in which sublimation is needed. This means that SMMs should be both chemically and thermally stable. In fact, these features constitute the major advantage of using EMFs as SMMs thanks to their highly robust fullerene structures. In this section, we move from the magnetic properties obtained from molecular ensembles in powder EMF samples towards the feasibility and prospect of their assembled molecular arrangements into different dimensions.

5.1 1D SMM assemblies inside single walled carbon nanotubes (SWCNTs)

With cylindrical empty space, single walled carbon nanotubes (SWCNTs) with a typical diameter range of 1–2 nm are intuitively considered as a suitable container for atoms or molecules to construct a 1D assembly. Spherical EMF molecules, such as Gd@C_{82} and $La_2@C_{80}$, usually possess diameters less than 1 nm and can be readily encapsulated into SWCNTs to form a peapod-like hybrid structure, thus enabling single atom imaging of lanthanides that may be transformed into lanthanide atomic wires upon heating.[230–232] Regarding SMMs, nevertheless, very few examples have been demonstrated combining them and SWCNTs, one of which is achieved through attaching bis-phthalocyaninato terbium ($TbPc_2$) onto the surfaces of SWCNTs, generating supramolecular spin valves with giant magnetoresistance.[233] On the other hand, encapsulation of SMMs into SWCNTs is expected to give rise to a quasi 1D arrangement in which their SMM properties should be enhanced.[234] A non-1D manifestation is using multi-walled carbon nanotubes (MWCNTs) with large diameters of ~6.5 nm to accommodate $[Mn_{12}O_{12}(O_2CCH_3)_{16}(H_2O)_4]$ ($Mn_{12}Ac$, with a diameter of 1.6 nm), whose SMM behaviors are significantly altered inside MWCNTs compared to its bulk properties.[235]

The first example to encapsulate EMF-SMMs into SWCNTs was reported by Yamashita *et al.* focusing on a well-studied NCF-SMM $DySc_2N@C_{80}$ *via* a sublimation method.[236] Transmission electron microscopy clearly showcases peapod structures wherein the EMF molecules line up in a quasi 1D chain as depicted in Fig. 11a and b. Magnetic characterization of this

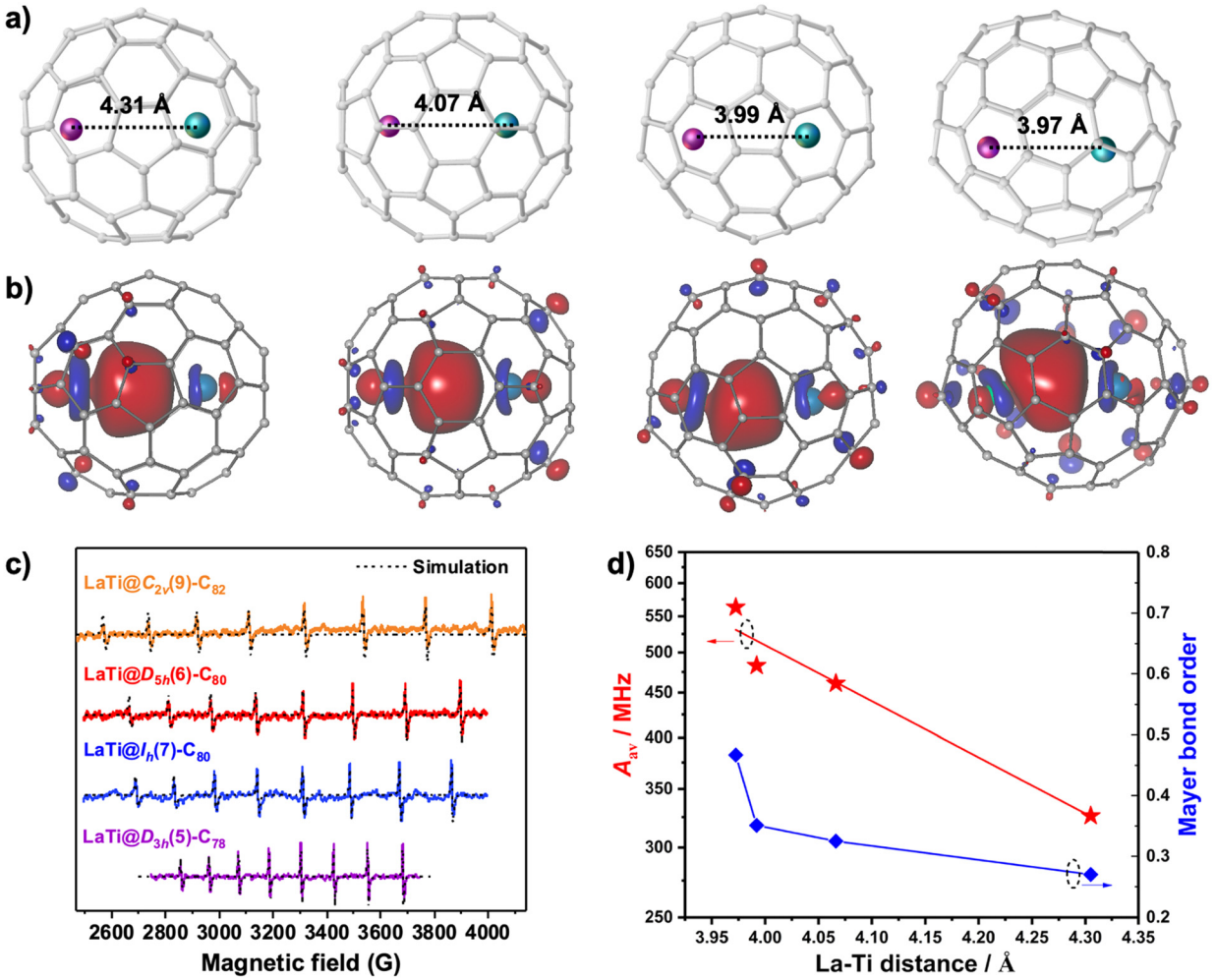

Fig. 10 (a) Molecular structures of LaTi@D_{3h}(5)-C_{78}, LaTi@I_h(7)-C_{80}, LaTi@D_{5h}(6)-C_{80}, and LaTi@C_{2v}(9)-C_{82} (from left to right). La: cyan, Ti: violet. Their La-Ti distances are indicated. (b) SOMOs of LaTi@D_{3h}(5)-C_{78}, LaTi@I_h(7)-C_{80}, LaTi@D_{5h}(6)-C_{80}, and LaTi@C_{2v}(9)-C_{82} (from left to right). (c) Experimental and simulated EPR spectra of LaTi@C_{2n} ($2n$ = 78, 80 (two isomers), 82) measured in toluene solutions at 243 K. (d) Average hyperfine coupling constant (A_{av} in MHz) and La-Ti Mayer bond order of LaTi@C_{2n} ($2n$ = 78, 80 (two isomers), 82) as a function of the La-Ti distance. Reproduced with permission from ref. 225 (Copy right 2023, American Chemical Society).

peapod structure [$DySc_2N@C_{80}$]@SWCNT by using SQUID magnetometers confirms that its characteristic SMM properties are retained inside SWCNTs with stepwise hysteresis at 1.8 K (Fig. 11c). Remarkably, the coercive field is greatly increased from 0.5 Oe in the bulk measurement to 0.4 T in the peapod structures, and correspondingly a slow relaxation of magnetization is observed in the absence of an external magnetic field with τ of 5650 s determined at 2 K, which is longer than that of $DySc_2N@C_{80}$ measured as a powder sample.[15] Suppression of QTM by diluting the EMF upon encapsulation into SWCNTs is likely accountable for these improvements in the SMM performance, demonstrating that SWCNTs are able to protect SMMs from the environment in this 1D hybrid system.

At the same time, another NCF bearing two Dy^{3+} ions, $Dy_2ScN@C_{80}$, was also successfully packed inside SWCNTs.[237] Element-specific XMCD was performed for this hybrid material at the Dy M_5-edge. The results show a deviation in its X-ray absorption spectra from that of an isotropic bulk sample, indicating a preferential orientation of the encapsulated Dy2ScN cluster that partially aligns the magnetization easy axis of the SMM in a 1D chain. This partial ordering of the clusters is also verified by *ab initio* calculations considering the diamagnetic counterpart $Y_2ScN@C_{80}$ inside the SWCNTs. Surprisingly and in striking contrast to the situation in mononuclear $DySc_2N@C_{80}$ packed peapod structures as described above, the broad hysteresis of the bulk $Dy_2ScN@C_{80}$ sample is not preserved when being filled inside the SWCNTs. Instead, magnetization curves for the $Dy_2ScN@C_{80}$/SWCNTs hybrid recorded at ~2 K reveal a reduced magnetic bistability and vanishing hysteretic behavior. Various possible reasons, such as a higher local temperature in XMCD measurements, interaction with conducting electrons in metallic SWCNTs, and dipole–dipole interactions with residue metallic catalyst nanoparticles, were proposed to explain the observed reduction of SMM properties, yet no conclusive rationale has been reached.

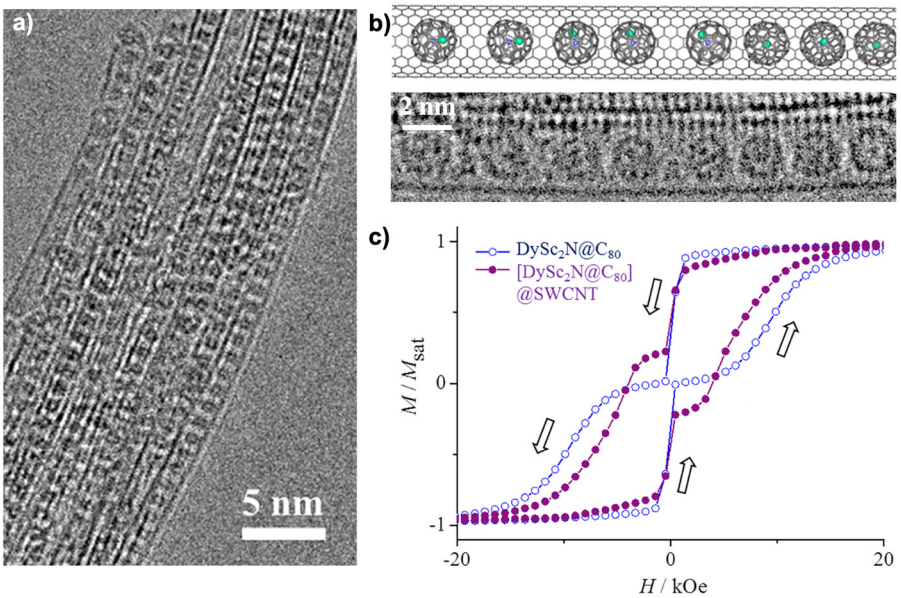

Fig. 11 (a) and (b) TEM images and structural model of [$DySc_2N@C_{80}$]@SWCNT. (c) Magnetic hysteresis loops for $DySc_2N@C_{80}$ (open circles) and [$DySc_2N@C_{80}$]@SWCNT (filled circles) at 1.8 K. Arrows indicate the direction of the measurements. Reproduced with permission from ref. 236 (Copy right 2018, American Chemical Society).

5.2 2D SMM assemblies on surfaces

Attaching SMMs onto conducting surfaces to form 2D molecular assemblies is a crucial step forward in the field, in which the inherent magnetic properties of the SMMs should be maintained or precisely controlled.[238–240] Among the plethora of examples of SMMs prepared so far, only a handful of candidates have been studied in surface science, such as $Mn_{12}Ac$, $TbPc_2$, and Fe_4, where the XMCD technique is greatly needed.[241–246] Various reasons can be ascribed to the lack of research in this area, majorly including the chemical instability that is often associated with the SMMs which precludes their processability onto surfaces under ultrahigh vacuum conditions at room temperature by sublimation and facilitates the loss of their magnetic bistability due to the detrimental interaction with the surfaces.[2] EMFs can thus be a suitable candidate in this context.

A submonolayer of a magnetic EMF $Gd_3N@C_{80}$ was prepared by depositing molecules onto metallic surfaces by thermal evaporation at room temperature.[247] Field-, temperature- and angle-dependent XMCD measurements of $Gd_3N@C_{80}$ on Cu(001) reveal that the magnetic moments of the individual $4f^7$ Gd^{3+} ion couple ferromagnetically to each other. On the other hand, changing the surface to ferromagnetic Ni(001) induces a spin polarization of the Gd^{3+} magnetic moments, enabling the detection of two different Gd species that couple ferromagnetically and antiferromagnetically to the Ni substrate. An indirect exchange mechanism mediated by the fullerene cage is accountable for the magnetic coupling to the substrate, and the different orientations of the cage are likely responsible for the observation of different coupling interactions within the same submonolayer.

The first EMF-SMM for surface science studies was reported by Greber *et al. via* depositing $Dy_2ScN@C_{80}$ onto a Rh(111) substrate using the same sublimation method under vacuum.[250] A submonolayer is generated in this way, in which the Dy^{3+} magnetic moments are aligned because of the interaction between the SMM and the metallic substrate. The angular anisotropy of X-ray absorption spectra and multiplet calculations indicate that the Dy_2ScN cluster is orientated parallel to the surface. Remarkably, magnetic hysteresis is observed in this submonolayer at $\sim$ 4 K. The relaxation time is estimated to be about 30 s at zero field, much faster than that measured for powder samples. Despite this reduced magnetic bistability after deposition, which should be partly due to the demagnetization effect caused by X-ray irradiation as mentioned before,[80] the surface-aligned magnetic ordering and the SMM behaviors in this EMF/Rh submonolayer are observed at one order of magnitude higher sample temperature than that for the transition-metal cluster SMMs.[242–244]

This result demonstrates the merit of using EMF-SMMs in surface science and thus has sparked further studies. For instance, employing the same preparation method, the same EMF-SMM $Dy_2ScN@C_{80}$ was evaporated onto a different surface, h-BN/Rh(111) nanomesh, to form 1.3 monolayers.[251] Similarly, partial orientations of the encapsulated units and of the magnetic moments are determined by angle-dependent XMCD measurements. It is demonstrated that the monolayers exhibit a larger hysteresis with a coercive field of 0.4 T at 2 K in comparison with the result of $Dy_2ScN@C_{80}$ on a pure Rh(111) surface. The magnetic behaviors of $Dy_2ScN@C_{80}$ monolayers on different substrates were then studied, where not only metals like Au(111) and Ag(100) but also insulators such as

MgO|Ag(100) were chosen for SMM deposition.[248] A strong influence of the surface on the structural ordering of $Dy_2ScN@C_{80}$ monolayers is revealed. Despite this, their SMM properties are very similar in XMCD studies, all exhibiting broad magnetic hysteresis, with a coercive field of *ca*. 0.4 T at 2 K (Fig. 12e), that is independent of the substrate. DFT calculations indicate that the charge state of the encapsulated cluster remains intact, which is due to the protection of its electronic and magnetic properties provided by the fullerene, acting as a Faraday cage, against interactions with conducting substrates.

Apart from evaporating the pristine EMFs to construct a 2D molecular assembly on surfaces, the chemical possibility to achieve the same goal, using functionalized $Dy_2ScN@C_{80}$ and $DySc_2N@C_{80}$ SMMs, was explored by Popov *et al.*[249] This is realized by 1,3-dipolar cycloaddition with surface-anchoring thioether groups (–S–CH_3). Compared to the pristine EMFs, the two functionalized molecules display different magnetic behaviors. In the case of $DySc_2N@C_{80}$, functionalization increases the bifurcation temperature $T_{B,ZFC}$ by 1 K, while the shape of hysteresis remains largely unchanged. For $Dy_2ScN@C_{80}$, the value of $T_{B,ZFC}$ becomes 4 K smaller and the hysteresis is noticeably thinner after functionalization. The thioether groups make it feasible to link these two functionalized EMF-SMMs to an Au(111) surface by simple physisorption, so as to generate low-coverage self-assembled monolayers (SAMs). XMCD measurements evidence that the magnetic bistability of these EMF-SMMs is retained in SAMs, featuring magnetic hysteresis at 2 K for each case. However, close contact of the fullerene cage with the metallic surface is favored in the preferential horizontal configurations, which is a result of the strong interaction of the fullerene and the linker with the substrate. This feature is expected to facilitate magnetic relaxation in SAMs. Furthermore, calculations indicate a random orientation of the Dy^{3+} magnetic moments at room temperature because of the highly mobile nature of these structures, whereas an orientation parallel to the surface is expected at low temperatures. A similar observation was also found recently for $DySc_2N@C_{80}$ adsorbed on a Pt(111) surface, which is directly inferred from the X-ray absorption spectra with in-plane polarization and indicates a weak but non-negligible interaction between the encapsulated cluster and the metallic surface.[252]

Changing the thioether linker –S–CH_3 to a thioacetate group –S–Ac as the surface-anchoring group (Fig. 12b), cycloadducts of $Dy_2ScN@C_{80}$ and $DySc_2N@C_{80}$ SMMs can be grafted on gold *via* chemisorption, rather than a pure physisorption process, to form self-assembled films with submonolayer coverage.[253] This is realized by dissolving functionalized EMFs in *o*-dichlorobenzene (*o*-DCB)/ethanol (10 : 1) upon adding H_2SO_4. The obtained SAMs from solution demonstrate that in both cases the magnetic bistability of bulk samples is maintained and the magnetic moments of the Dy ions are preferentially aligned parallel to the surface. Comparative magnetic studies were performed by XMCD measurements of the grafted SMMs using this facile solution-based procedure and of the pristine EMFs on the substrate prepared by sublimation. It is shown that while this chemical functionalization tends to reduce the SMM properties of $Dy_2ScN@C_{80}$, magnetic bistability in the on-surface $DySc_2N@C_{80}$, as can be seen in Fig. 12f, is significantly enhanced with observable magnetic hysteresis up to 10 K. The shielding effect of the carbon cage on the encapsulated magnetic centers also enables robust SMM behaviors that are not hinged upon the metallic substrate.

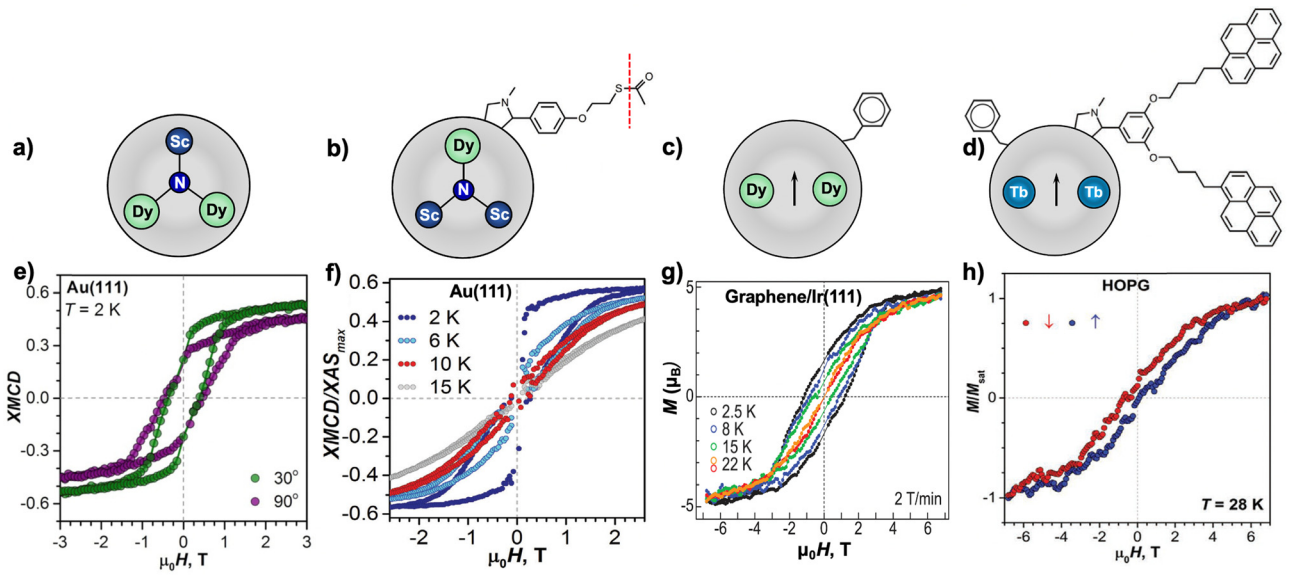

Fig. 12 (a)–(d) Illustrations of $Dy_2ScN@C_{80}$ (a), functionalized $DySc_2N@C_{80}$ with a surface-anchoring thioacetate group (b), $Dy_2@C_{80}(CH_2Ph)$ (c), and pyrene-functionalized $Tb_2@C_{80}(CH_2Ph)$. (e)–(h) Magnetic hysteretic behaviors of submonolayers for $Dy_2ScN@C_{80}$ on Au(111) (e), functionalized $DySc_2N@C_{80}$ on Au(111) (f), $Dy_2@C_{80}(CH_2Ph)$ on graphene/Ir(111) (g), and pyrene-functionalized $Tb_2@C_{80}(CH_2Ph)$ on HOPG (h). Reproduced with permission from (e) ref. 248, (f) ref. 249, (g) ref. 24 and (h) ref. 26.

Moving from the NCFs to SEMB-containing di-EMFs with better SMM performance, the possibility of generating a 2D molecular assembly based on $Dy_2@C_{80}(CH_2Ph)$ was first explored.[24] It should be noted that in contrast to the non-derivatized EMFs with the pristine fullerene cages, lower thermal stability of $Dy_2@C_{80}(CH_2Ph)$ precludes its direct deposition on a surface by sublimation. Meanwhile, this functionalized EMF also lacks a surface-anchoring group that is necessary for the formation of self-assembled submonolayers. To this end, a gentle deposition method of electrospray technique was used in the preparation of $Dy_2@C_{80}(CH_2Ph)$ on graphene/Ir(111) as a suitable substrate. Remarkably, the as-formed submonolayer exhibits SMM behaviors that are fully comparable to those observed for the bulk sample. A broad magnetic hysteresis can be recorded by XMCD measurements at 2 K, which persists until around 20 K (Fig. 12g). Moreover, time-dependent XMCD relaxation measurements allow disentanglement of the contribution of the X-ray photon flux to the demagnetization effect. The analysis of its temperature-dependent relaxation times thus gives rise to a high 100-s blocking temperature T_B of 17 K in this surface-supported SMM. In this 2D assembly, scanning tunneling microscopy was applied to directly image the unoccupied single-electron Dy–Dy bonding orbital (LUMO) with the aid of *ab initio* calculations.[254] This result is further validated by changing the encapsulated metal from Dy to Er, which leads to the observation of an energy shift of the metal-based LUMO with respect to the neighboring cage-based orbitals. The energetically and spatially resolved SEMB orbital thus offers a direct access to this exchange-coupled magnetic system in transport experiments.

The bulk studies of di-EMFs indicate the better SMM performance of the Tb^{3+}–e–Tb^{3+} three-center system, with $Tb_2@C_{80}(CH_2Ph)$ as an example, than that of its Dy counterpart. In order to obtain its self-assembled monolayers, further exohedral functionalization is necessary. This was done by introducing pyrene groups which show high affinity to graphitic substrates.[26] Interestingly, pyrene-functionalized $Tb_2@C_{80}(CH_2Ph)(pyr_2)$ (Fig. 12d) features similar but slightly better SMM performance than $Tb_2@C_{80}(CH_2Ph)$. Higher $T_{B,100s}$ of 26.6 K and $T_{B,ZFC}$ of 30.3 K are obtained after functionalization compared to those of $Tb_2@C_{80}(CH_2Ph)$ ($T_{B,100s}$ = 25.2 K and $T_{B,ZFC}$ = 28.9 K) determined using the same experimental conditions. $Tb_2@C_{80}(CH_2Ph)(pyr_2)$ SAMs can then be simply constructed by the solution-based preparation procedure on graphitic substrates (graphene and highly oriented pyrolytic graphite HOPG) in an ambient environment. The magnetic bistability of this EMF-SMM is preserved on substrates, showing a broad magnetic hysteresis that closes down up to a very high temperature of 28 K (Fig. 12h), which is a major step forward in the field of on-surface SMMs.

In the case of $Tb_2@C_{79}N$ with a similar three-center system but without the derivatized "branch" outside the cage, the growth of thin films by sublimation under ultra-high vacuum conditions becomes feasible thanks to its sufficient thermal stability. Thus, monolayers of $Tb_2@C_{79}N$ were prepared on Cu(111) and Au(111) substrates.[25] While the bulk sample of $Tb_2@C_{79}N$ is a high-blocking temperature ($T_{B,100s}$ = 24 K) SMM featuring a strongly ferromagnetic coupling between two Tb magnetic moments and the unpaired electron spin, a distinct antiferromagnetically coupled ground state is identified for its monolayers in XMCD studied at the Tb-$M_{4,5}$ edge. This results in a non-magnetic state in which magnetization is completely lost, and can be assigned to anionic $Tb_2@C_{79}N^-$ species with a doubly-occupied Tb–Tb bonding orbital, likely due to charge transfer from the substrate or trapping of secondary electrons. Since the antiferromagnetic coupling in this non-magnetic state is not strong enough, a metamagnetic transition can be found in the field of 2.5–4 T, where the ferromagnetically coupled state dominates. By depositing $Tb_2@C_{79}N$ on other substrates, such as h-BN|Rh(111) and MgO|Ag(100), the coexistence of neutral and anionic species can be observed, leading to a narrow magnetic hysteresis that persists up to 25 K.

5.3 3D SMM assemblies within metal–organic frameworks (MOFs)

A more complex network of SMMs is a 3D molecular assembly, for which porous metal–organic frameworks can be naturally considered as a suitable host.[255,256] Regarding EMFs, paramagnetic $Y_2@C_{79}N$ was first introduced by Wang *et al.* inside the pores of a MOF crystal (MOF-177) to show axisymmetric paramagnetic properties.[257] These different magnetic properties in the host–guest complex, in comparison with the isotropic system observed for $Y_2@C_{79}N$ both in solution and in powder, suggest that the electron spin can be steered inside the pores of the MOF. The same group later reported that by combining the same MOF-177 and a different paramagnetic EMF $Sc_3C_2@C_{80}$, the latter is able to act as a spin probe to sensitively detect the pore environment of the MOF.[258] On the other hand, gas adsorption can be detected when a pyrene-based covalent organic framework (Py-COF) is introduced as the host.[259]

By embedding $DySc_2N@C_{80}$ SMM into the pores of MOF-177, it is demonstrated that the QTM effect at zero field can be effectively suppressed upon encapsulation.[260] A similar observation was also found for the same EMF incorporated into a different MOF structure, which is due to the dilution effect that weakens intermolecular interactions.[64] By incarcerating $DySc_2N@C_{80}$ into a photo-switchable azobenzene functionalized MOF (^{Azo}MOF), magnetic hysteresis opens up at zero field at 2 K by suppressing the QTM effect.[261] More importantly, the hysteresis becomes broader after ultraviolet (365 nm) irradiation. The isomerization of azobenzene groups is expected to change the host–guest interaction between the EMF molecule and the MOF structure, and should be responsible for the enhanced SMM properties.

6. Conclusions and outlook

Since the discovery of $DySc_2N@C_{80}$ as the first EMF-SMM in 2012, EMFs have constituted an important branch of lanthanide-based SMMs during the last decade as elaborately summarized in this article. For the SMMs that are hinged upon

only one magnetic lanthanide ion (SIMs), single-ion anisotropy plays a pivotal role. This factor can be precisely manipulated by engineering the structures of the encapsulated cluster and of the host fullerene cage in various types of clusterfullerene, in which the confinement effect imposed by the carbon cage facilitates strong axial anisotropy towards the nonmetal ligand with a short metal–nonmetal distance. Removing this nonmetal ligand and changing the electronic structure of the fullerene give rise to a low-coordination mono-EMF with a closed-shell cage, where vibrational degrees of freedom are minimized, thus reducing another equally important factor of spin–vibration coupling that is detrimental to magnetic bistability. In these EMF-SIMs, how to effectively suppress QTM in non-diluted bulk samples? To address this critical issue, judicious design of the cluster and cage structures is necessary. Heterometallic oxide clusterfullerenes with the largest possible effective barrier may be a target because their extremely axial ligand field may be able to quench QTM within the highly pure ground doublet $m_J = \pm 15/2$ for the encapsulated Dy^{3+} ion. Fine control of the local symmetry of the coordination environment is another possible solution, which nevertheless remains largely unexplored in EMFs. The design strategy for the special case of mono-EMFs with closed-shell fullerene cages, on the other hand, is more straightforward since the cage structure is the only variable factor given the same encapsulated Ln. Here, a fullerene cage with a more rigid metal–cage binding interaction is expected to reduce spin–vibration coupling so as to slow down the magnetic relaxation. To this end, mono-EMFs with non-IPR cages are of particular relevance.

For the SMMs consisting of two magnetic lanthanide ions, magnetic coupling between them becomes a decisive factor governing their magnetic properties by blocking quantum tunneling of magnetization. This factor can be applied in clusterfullerenes by designing different bridging ligands that are able to transfer superexchange interactions as well as by altering the cage structures which in turn fine-tune the cluster geometry. Alternatively, such a goal can be realized in di-EMFs by engineering the electronic structure of the cage to generate single-electron metal–metal bonds (SEMBs), in which the unpaired electron directly couples to the two metals in the absence of any nonmetal bridging ligand. In these dinuclear EMFs, how to enhance magnetic coupling is the key to realize better SMMs. Whether it is feasible to generate an efficient direct Heisenberg exchange, rather than superexchange interaction, in a Ln–Ln bonding system becomes an intriguing aspect. On the other hand, although single-electron Ln–Ln bonds are an eye-catching case, the problem lies in the fact that the Ln–Ln distance is not short enough to induce strong magnetic coupling comparable to that of the best-performing SMM. Changing the host cage to compress the Ln_2 dimer appears to be a promising direction despite its synthetic challenge given that available cage structures are very limited so far.

Another more general consideration is focused on the lanthanide metals. Since now the magnetic bistability of all reported EMF-SMMs comes from Dy^{3+} and Tb^{3+} only, the possibility of exploiting other Ln metals, especially early lanthanides, is of great interest to researchers. These candidates are in fact being widely used in permanent magnets, such as $Nd_2Fe_{14}B$ and $SmCo_5$. The similarity of single-ion anisotropy between early and late lanthanide ions that differ by seven f electrons may provide a general guidance herein. Beyond single molecular behaviors in bulk, several EMF-SMMs have been further processed into molecular assemblies *via* sublimation or self-assembly thanks to their rich structural diversity, exceptional magnetic properties and high chemical and thermal robustness. Their intrinsic SMM properties can be largely maintained in these organized structures, showcasing their great potential in information storage where single-molecule addressing is needed. With these exciting advancements, a next step forward would be to construct molecular spintronic devices based on SMMs towards their practical use as magnetic memory units to store information, yet very little is known about the role SMMs can play in this context. To fulfill future advancement directed at high-temperature, processable EMF-SMMs and beyond, there are many open questions remaining to be addressed. These endeavors, from the point of view of synthetic chemistry, shall be undertaken with an emphasis on the new structures, new related physical phenomena as well as the understanding of their interplay at an atomic level.

Conflicts of interest

There are no conflicts to declare.

Acknowledgements

This work was supported by the National Natural Science Foundation of China (51925206, U1932214, and 52302052), the Anhui Provincial Natural Science Foundation (2308085MB33), the Strategic Priority Research Program of the Chinese Academy of Sciences (XDB0450301), the Fundamental Research Funds for the Central Universities (20720220009), and the National Synchrotron Radiation Laboratory (KY2060000240)

References

1 D. Gatteschi, R. Sessoli and J. Villain, *Molecular Nanomagnets*, OUP Oxford, 2006.
2 E. Coronado, *Nat. Rev. Mater.*, 2020, **5**, 87–104.
3 A. Gaita-Ariño, F. Luis, S. Hill and E. Coronado, *Nat. Chem.*, 2019, **11**, 301–309.
4 M. Atzori and R. Sessoli, *J. Am. Chem. Soc.*, 2019, **141**, 11339–11352.
5 R. Sessoli, D. Gatteschi, A. Caneschi and M. Novak, *Nature*, 1993, **365**, 141–143.
6 N. Ishikawa, M. Sugita, T. Ishikawa, S.-Y. Koshihara and Y. Kaizu, *J. Am. Chem. Soc.*, 2003, **125**, 8694–8695.
7 S.-D. Jiang, B.-W. Wang, H.-L. Sun, Z.-M. Wang and S. Gao, *J. Am. Chem. Soc.*, 2011, **133**, 4730–4733.

8 S. Cotton, *Lanthanide and Actinide Chemistry*, John Wiley & Sons, 2013.
9 J.-L. Liu, Y.-C. Chen and M.-L. Tong, *Chem. Soc. Rev.*, 2018, **47**, 2431–2453.
10 D. N. Woodruff, R. E. P. Winpenny and R. A. Layfield, *Chem. Rev.*, 2013, **113**, 5110–5148.
11 K. Randall McClain, C. A. Gould, K. Chakarawet, S. J. Teat, T. J. Groshens, J. R. Long and B. G. Harvey, *Chem. Sci.*, 2018, **9**, 8492–8503.
12 F.-S. Guo, B. M. Day, Y.-C. Chen, M.-L. Tong, A. Mansikkamäki and R. A. Layfield, *Science*, 2018, **362**, 1400–1403.
13 A. A. Popov, S. Yang and L. Dunsch, *Chem. Rev.*, 2013, **113**, 5989–6113.
14 S. Yang, T. Wei and F. Jin, *Chem. Soc. Rev.*, 2017, **46**, 5005–5058.
15 R. Westerström, J. Dreiser, C. Piamonteze, M. Muntwiler, S. Weyeneth, H. Brune, S. Rusponi, F. Nolting, A. Popov, S. Yang, L. Dunsch and T. Greber, *J. Am. Chem. Soc.*, 2012, **134**, 9840–9843.
16 Z. Hu, Y. Wang, A. Ullah, G. M. Gutiérrez-Finol, A. Bedoya-Pinto, P. Gargiani, D. Shi, S. Yang, Z. Shi and A. Gaita-Ariño, *Chem*, 2023, **9**, 3613–3622.
17 F. Liu, L. Spree, D. S. Krylov, G. Velkos, S. M. Avdoshenko and A. A. Popov, *Acc. Chem. Res.*, 2019, **52**, 2981–2993.
18 F. Liu, D. S. Krylov, L. Spree, S. M. Avdoshenko, N. A. Samoylova, M. Rosenkranz, A. Kostanyan, T. Greber, A. U. B. Wolter, B. Büchner and A. A. Popov, *Nat. Commun.*, 2017, **8**, 16098.
19 F. Liu, G. Velkos, D. S. Krylov, L. Spree, M. Zalibera, R. Ray, N. A. Samoylova, C.-H. Chen, M. Rosenkranz, S. Schiemenz, F. Ziegs, K. Nenkov, A. Kostanyan, T. Greber, A. U. B. Wolter, M. Richter, B. Büchner, S. M. Avdoshenko and A. A. Popov, *Nat. Commun.*, 2019, **10**, 571.
20 Y. Wang, G. Velkos, N. J. Israel, M. Rosenkranz, B. Büchner, F. Liu and A. A. Popov, *J. Am. Chem. Soc.*, 2021, **143**, 18139–18149.
21 G. Velkos, D. S. Krylov, K. Kirkpatrick, L. Spree, V. Dubrovin, B. Büchner, S. M. Avdoshenko, V. Bezmelnitsyn, S. Davis, P. Faust, J. Duchamp, H. C. Dorn and A. A. Popov, *Angew. Chem., Int. Ed.*, 2019, **58**, 5891–5896.
22 Y. Wang, J. Xiong, J. Su, Z. Hu, F. Ma, R. Sun, X. Tan, H.-L. Sun, B.-W. Wang, Z. Shi and S. Gao, *Nanoscale*, 2020, **12**, 11130–11135.
23 C. A. Gould, K. R. McClain, D. Reta, J. G. C. Kragskow, D. A. Marchiori, E. Lachman, E.-S. Choi, J. G. Analytis, R. D. Britt, N. F. Chilton, B. G. Harvey and J. R. Long, *Science*, 2022, **375**, 198–202.
24 F. Paschke, T. Birk, V. Enenkel, F. Liu, V. Romankov, J. Dreiser, A. A. Popov and M. Fonin, *Adv. Mater.*, 2021, **33**, e2102844.
25 E. Koutsouflakis, D. Krylov, N. Bachellier, D. Sostina, V. Dubrovin, F. Liu, L. Spree, G. Velkos, S. Schimmel, Y. Wang, B. Büchner, R. Westerström, C. Bulbucan, K. Kirkpatrick, M. Muntwiler, J. Dreiser, T. Greber, S. M. Avdoshenko, H. Dorn and A. A. Popov, *Nanoscale*, 2022, **14**, 9877–9892.
26 L. Spree, F. Liu, V. Neu, M. Rosenkranz, G. Velkos, Y. Wang, S. Schiemenz, J. Dreiser, P. Gargiani, M. Valvidares, C.-H. Chen, B. Büchner, S. M. Avdoshenko and A. A. Popov, *Adv. Funct. Mater.*, 2021, **31**, 2105516.
27 W. Krätschmer, L. D. Lamb, K. Fostiropoulos and D. R. Huffman, *Nature*, 1990, **347**, 354–358.
28 S. Stevenson, G. Rice, T. Glass, K. Harich, F. Cromer, M. Jordan, J. Craft, E. Hadju, R. Bible and M. Olmstead, *Nature*, 1999, **401**, 55–57.
29 C.-H. Chen, D. S. Krylov, S. M. Avdoshenko, F. Liu, L. Spree, R. Yadav, A. Alvertis, L. Hozoi, K. Nenkov, A. Kostanyan, T. Greber, A. U. B. Wolter and A. A. Popov, *Chem. Sci.*, 2017, **8**, 6451–6465.
30 J. Xin, F. Jin, R. Guan, M. Chen, X.-M. Xie, Q. Zhang, S.-Y. Xie and S. Yang, *Inorg. Chem. Front.*, 2021, **8**, 1719–1726.
31 J. Zhang, S. Stevenson and H. C. Dorn, *Acc. Chem. Res.*, 2013, **46**, 1548–1557.
32 S. Yang, S. I. Troyanov, A. A. Popov, M. Krause and L. Dunsch, *J. Am. Chem. Soc.*, 2006, **128**, 16733–16739.
33 Y.-Y. Xu, H.-R. Tian, S.-H. Li, Z.-C. Chen, Y.-R. Yao, S.-S. Wang, X. Zhang, Z.-Z. Zhu, S.-L. Deng and Q. Zhang, *Nat. Commun.*, 2019, **10**, 485.
34 S. Yang, F. Liu, C. Chen, M. Jiao and T. Wei, *Chem. Commun.*, 2011, **47**, 11822–11839.
35 X. Lu, L. Feng, T. Akasaka and S. Nagase, *Chem. Soc. Rev.*, 2012, **41**, 7723–7760.
36 A. Rodríguez-Fortea, A. L. Balch and J. M. Poblet, *Chem. Soc. Rev.*, 2011, **40**, 3551–3563.
37 W. Xu, L. Feng, M. Calvaresi, J. Liu, Y. Liu, B. Niu, Z. Shi, Y. Lian and F. Zerbetto, *J. Am. Chem. Soc.*, 2013, **135**, 4187–4190.
38 H. W. Kroto, J. R. Heath, S. C. Obrien, R. F. Curl and R. E. Smalley, *Nature*, 1985, **318**, 162–163.
39 J. Heath, S. O'brien, Q. Zhang, Y. Liu, R. Curl, F. Tittel and R. Smalley, *J. Am. Chem. Soc.*, 1985, **107**, 7779–7780.
40 T. A. Murphy, T. Pawlik, A. Weidinger, M. Höhne, R. Alcala and J.-M. Spaeth, *Phys. Rev. Lett.*, 1996, **77**, 1075.
41 T. Zuo, L. Xu, C. M. Beavers, M. M. Olmstead, W. Fu, T. D. Crawford, A. L. Balch and H. C. Dorn, *J. Am. Chem. Soc.*, 2008, **130**, 12992–12997.
42 W. Xiang, X. Jiang, Y.-R. Yao, J. Xin, H. Jin, R. Guan, Q. Zhang, M. Chen, S.-Y. Xie and A. A. Popov, *J. Am. Chem. Soc.*, 2022, **144**, 21587–21595.
43 W. Fu, J. Zhang, T. Fuhrer, H. Champion, K. Furukawa, T. Kato, J. E. Mahaney, B. G. Burke, K. A. Williams, K. Walker, C. Dixon, J. Ge, C. Shu, K. Harich and H. C. Dorn, *J. Am. Chem. Soc.*, 2011, **133**, 9741–9750.
44 T. Wakahara, H. Nikawa, T. Kikuchi, T. Nakahodo, G. A. Rahman, T. Tsuchiya, Y. Maeda, T. Akasaka, K. Yoza and E. Horn, *J. Am. Chem. Soc.*, 2006, **128**, 14228–14229.
45 H. Yang, C. X. Lu, Z. Y. Liu, H. X. Jin, Y. L. Che, M. M. Olmstead and A. L. Balch, *J. Am. Chem. Soc.*, 2008, **130**, 17296–17300.
46 B. Q. Mercado, M. A. Stuart, M. A. Mackey, J. E. Pickens, B. S. Confait, S. Stevenson, M. L. Easterling, R. Valencia,

A. Rodriguez-Fortea, J. M. Poblet, M. M. Olmstead and A. L. Balch, *J. Am. Chem. Soc.*, 2010, **132**, 12098–12105.
47 S. Yang, C. Chen, F. Liu, Y. Xie, F. Li, M. Jiao, M. Suzuki, T. Wei, S. Wang, Z. Chen, X. Lu and T. Akasaka, *Sci. Rep.*, 2013, **3**, 1487.
48 C. Pan, L. Bao, X. Yu, H. Fang, Y. Xie, T. Akasaka and X. Lu, *ACS Nano*, 2018, **12**, 2065–2069.
49 S. Aoyagi, E. Nishibori, H. Sawa, K. Sugimoto, M. Takata, Y. Miyata, R. Kitaura, H. Shinohara, H. Okada, T. Sakai, Y. Ono, K. Kawachi, K. Yokoo, S. Ono, K. Omote, Y. Kasama, S. Ishikawa, T. Komuro and H. Tobita, *Nat. Chem.*, 2010, **2**, 678–683.
50 R. Guan, M. Chen, F. Jin and S. Yang, *Angew. Chem., Int. Ed.*, 2020, **59**, 1048–1073.
51 Y. Wang, S. Diaz-Tendero, F. Martin and M. Alcami, *J. Am. Chem. Soc.*, 2016, **138**, 1551–1560.
52 T. Wang and C. Wang, *Acc. Chem. Res.*, 2014, **47**, 450–458.
53 Z. Hu, B. W. Dong, Z. Liu, J. J. Liu, J. Su, C. Yu, J. Xiong, D. E. Shi, Y. Wang, B. W. Wang, A. Ardavan, Z. Shi, S. D. Jiang and S. Gao, *J. Am. Chem. Soc.*, 2018, **140**, 1123–1130.
54 J. Dreiser, K. S. Pedersen, C. Piamonteze, S. Rusponi, Z. Salman, M. E. Ali, M. Schau-Magnussen, C. A. Thuesen, S. Piligkos and H. Weihe, *Chem. Sci.*, 2012, **3**, 1024–1032.
55 G. Velkos, W. Yang, Y.-R. Yao, S. M. Sudarkova, X. Liu, B. Büchner, S. M. Avdoshenko, N. Chen and A. A. Popov, *Chem. Sci.*, 2020, **11**, 4766–4772.
56 A. Lunghi, F. Totti, R. Sessoli and S. Sanvito, *Nat. Commun.*, 2017, **8**, 14620.
57 D. Reta, J. G. C. Kragskow and N. F. Chilton, *J. Am. Chem. Soc.*, 2021, **143**, 5943–5950.
58 A. Ullah, J. Cerdá, J. J. Baldoví, S. A. Varganov, J. Aragó and A. Gaita-Ariño, *J. Phys. Chem. Lett.*, 2019, **10**, 7678–7683.
59 L. Escalera-Moreno, J. J. Baldoví, A. Gaita-Ariño and E. Coronado, *Chem. Sci.*, 2018, **9**, 3265–3275.
60 E. Garlatti, A. Chiesa, P. Bonfà, E. Macaluso, I. J. Onuorah, V. S. Parmar, Y.-S. Ding, Y.-Z. Zheng, M. J. Giansiracusa, D. Reta, E. Pavarini, T. Guidi, D. P. Mills, N. F. Chilton, R. E. P. Winpenny, P. Santini and S. Carretta, *J. Phys. Chem. Lett.*, 2021, **12**, 8826–8832.
61 J. G. C. Kragskow, J. Marbey, C. D. Buch, J. Nehrkorn, M. Ozerov, S. Piligkos, S. Hill and N. F. Chilton, *Nat. Commun.*, 2022, **13**, 825.
62 A. L. Blockmon, A. Ullah, K. D. Hughey and Y. Duan, *et al.*, *Inorg. Chem.*, 2021, **60**, 14096–14104.
63 A. Chiesa, F. Cugini, R. Hussain, E. Macaluso, G. Allodi, E. Garlatti, M. Giansiracusa, C. A. P. Goodwin, F. Ortu, D. Reta, J. M. Skelton, T. Guidi, P. Santini, M. Solzi, R. De Renzi, D. P. Mills, N. F. Chilton and S. Carretta, *Phys. Rev. B*, 2020, **101**, 174402.
64 D. S. Krylov, F. Liu, A. Brandenburg, L. Spree, V. Bon, S. Kaskel, A. U. B. Wolter, B. Buchner, S. M. Avdoshenko and A. A. Popov, *Phys. Chem. Chem. Phys.*, 2018, **20**, 11656–11672.
65 A. A. Popov, C. Chen, S. Yang, F. Lipps and L. Dunsch, *ACS Nano*, 2010, **4**, 4857–4871.
66 T. Wei, S. Wang, X. Lu, Y. Tan, J. Huang, F. Liu, Q. Li, S. Xie and S. Yang, *J. Am. Chem. Soc.*, 2016, **138**, 207–214.
67 T. Wei, F. Jin, R. Guan, J. Huang, M. Chen, Q. Li and S. Yang, *Angew. Chem., Int. Ed.*, 2018, **57**, 10273–10277.
68 S. Yang, C. Chen, A. A. Popov, W. Zhang, F. Liu and L. Dunsch, *Chem. Commun.*, 2009, 6391–6393, DOI: 10.1039/b911267g.
69 C. Chen, F. Liu, S. Li, N. Wang, A. A. Popov, M. Jiao, T. Wei, Q. Li, L. Dunsch and S. Yang, *Inorg. Chem.*, 2012, **51**, 3039–3045.
70 S. Stevenson, P. Fowler, T. Heine, J. Duchamp, G. Rice, T. Glass, K. Harich, E. Hajdu, R. Bible and H. Dorn, *Nature*, 2000, **408**, 427–428.
71 M. M. Olmstead, H. M. Lee, J. C. Duchamp, S. Stevenson, D. Marciu, H. C. Dorn and A. L. Balch, *Angew. Chem., Int. Ed.*, 2003, **42**, 900–903.
72 M. N. Chaur, R. Valencia, A. Rodriguez-Fortea, J. M. Poblet and L. Echegoyen, *Angew. Chem., Int. Ed.*, 2009, **48**, 1425–1428.
73 M. N. Chaur, F. Melin, J. Ashby, B. Elliott, A. Kumbhar, A. M. Rao and L. Echegoyen, *Chem. – Eur. J.*, 2008, **14**, 8213–8219.
74 M. N. Chaur, F. Melin, B. Elliott, A. Kumbhar, A. J. Athans and L. Echegoyen, *Chem. – Eur. J.*, 2008, **14**, 4594–4599.
75 J. D. Rinehart and J. R. Long, *Chem. Sci.*, 2011, **2**, 2078–2085.
76 L. Spree and A. A. Popov, *Dalton Trans.*, 2019, **48**, 2861–2871.
77 S. T. Liddle and J. van Slageren, *Chem. Soc. Rev.*, 2015, **44**, 6655–6669.
78 L. Spree, C. Schlesier, A. Kostanyan, R. Westerstrom, T. Greber, B. Buchner, S. M. Avdoshenko and A. A. Popov, *Chem. – Eur. J.*, 2020, **26**, 2436–2449.
79 Y. Hao, G. Velkos, S. Schiemenz, M. Rosenkranz, Y. Wang, B. Büchner, S. M. Avdoshenko, A. A. Popov and F. Liu, *Inorg. Chem. Front.*, 2023, **10**, 468–484.
80 J. Dreiser, R. Westerström, C. Piamonteze, F. Nolting, S. Rusponi, H. Brune, S. Yang, A. Popov, L. Dunsch and T. Greber, *Appl. Phys. Lett.*, 2014, **105**, 032411.
81 M. Nie, J. Liang, C. Zhao, Y. Lu, J. Zhang, W. Li, C. Wang and T. Wang, *ACS Nano*, 2021, **15**, 19080–19088.
82 M. Garcia-Borras, S. Osuna, J. M. Luis, M. Swart and M. Sola, *Chem. Soc. Rev.*, 2014, **43**, 5089–5105.
83 Z. Hu, A. Ullah, H. Prima-Garcia, S.-H. Chin, Y. Wang, J. Aragó, Z. Shi, A. Gaita-Ariño and E. Coronado, *Chem. – Eur. J.*, 2021, **27**, 13242–13248.
84 C. Schlesier, L. Spree, A. Kostanyan, R. Westerstrom, A. Brandenburg, A. U. B. Wolter, S. Yang, T. Greber and A. A. Popov, *Chem. Commun.*, 2018, **54**, 9730–9733.
85 J. Dreiser, R. Westerstrom, Y. Zhang, A. A. Popov, L. Dunsch, K. Kramer, S. X. Liu, S. Decurtins and T. Greber, *Chem. – Eur. J.*, 2014, **20**, 13536–13540.
86 Y. Zhang, D. Krylov, S. Schiemenz, M. Rosenkranz, R. Westerstrom, J. Dreiser, T. Greber, B. Buchner and A. A. Popov, *Nanoscale*, 2014, **6**, 11431–11438.
87 A. Kostanyan, R. Westerstrom, Y. Zhang, D. Kunhardt, R. Stania, B. Buchner, A. A. Popov and T. Greber, *Phys. Rev. Lett.*, 2017, **119**, 237202.

88 Y. Zhang, D. Krylov, M. Rosenkranz, S. Schiemenz and A. A. Popov, *Chem. Sci.*, 2015, **6**, 2328–2341.
89 V. Vieru, L. Ungur and L. F. Chibotaru, *J. Phys. Chem. Lett.*, 2013, **4**, 3565–3569.
90 N. Ishikawa, M. Sugita and W. Wernsdorfer, *Angew. Chem., Int. Ed.*, 2005, **44**, 2931–2935.
91 Y.-C. Chen and M.-L. Tong, *Chem. Sci.*, 2022, **13**, 8716–8726.
92 B.-K. Ling, Y.-Q. Zhai, P.-B. Jin, H.-F. Ding, X.-F. Zhang, Y. Lv, Z. Fu, J. Deng, M. Schulze and W. Wernsdorfer, *Matter*, 2022, **5**, 3485–3498.
93 R. Westerström, J. Dreiser, C. Piamonteze, M. Muntwiler, S. Weyeneth, K. Krämer, S.-X. Liu, S. Decurtins, A. Popov, S. Yang, L. Dunsch and T. Greber, *Phys. Rev. B: Condens. Matter Mater. Phys.*, 2014, **89**, 060406(R).
94 R. Westerström, V. Dubrovin, K. Junghans, C. Schlesier, B. Büchner, S. M. Avdoshenko, A. A. Popov, A. Kostanyan, J. Dreiser and T. Greber, *Phys. Rev. B*, 2021, **104**, 224401.
95 D. S. Krylov, F. Liu, S. M. Avdoshenko, L. Spree, B. Weise, A. Waske, A. U. B. Wolter, B. Buchner and A. A. Popov, *Chem. Commun.*, 2017, **53**, 7901–7904.
96 A. Kostanyan, C. Schlesier, R. Westerström, J. Dreiser, F. Fritz, B. Büchner, A. A. Popov, C. Piamonteze and T. Greber, *Phys. Rev. B*, 2021, **103**, 014404.
97 M. Nie, J. Xiong, C. Zhao, H. Meng, K. Zhang, Y. Han, J. Li, B. Wang, L. Feng, C. Wang and T. Wang, *Nano Res.*, 2019, **12**, 1727–1731.
98 A. Kostanyan, R. Westerström, D. Kunhardt, B. Büchner, A. A. Popov and T. Greber, *Phys. Rev. B*, 2020, **101**, 134429.
99 F. Liu, S. Wang, C. L. Gao, Q. Deng, X. Zhu, A. Kostanyan, R. Westerstrom, F. Jin, S. Y. Xie, A. A. Popov, T. Greber and S. Yang, *Angew. Chem., Int. Ed.*, 2017, **56**, 1830–1834.
100 F. Liu, C.-L. Gao, Q. Deng, X. Zhu, A. Kostanyan, R. Westerström, S. Wang, Y.-Z. Tan, J. Tao, S.-Y. Xie, A. A. Popov, T. Greber and S. Yang, *J. Am. Chem. Soc.*, 2016, **138**, 14764–14771.
101 G. Velkos, W. Yang, Y. R. Yao, S. M. Sudarkova, F. Liu, S. M. Avdoshenko, N. Chen and A. A. Popov, *Chem. Commun.*, 2022, **58**, 7164–7167.
102 W. Yang, G. Velkos, F. Liu, S. M. Sudarkova, Y. Wang, J. Zhuang, H. Zhang, X. Li, X. Zhang, B. Buchner, S. M. Avdoshenko, A. A. Popov and N. Chen, *Adv. Sci.*, 2019, **6**, 1901352.
103 W. Yang, G. Velkos, S. Sudarkova, B. Büchner, S. M. Avdoshenko, F. Liu, A. A. Popov and N. Chen, *Inorg. Chem. Front.*, 2022, **9**, 5805–5819.
104 D. Krylov, G. Velkos, C. H. Chen, B. Buchner, A. Kostanyan, T. Greber, S. M. Avdoshenko and A. A. Popov, *Inorg. Chem. Front.*, 2020, **7**, 3521–3532.
105 W. Cai, J. D. Bocarsly, A. Gomez, R. J. L. Lee, A. Metta-Magana, R. Seshadri and L. Echegoyen, *Chem. Sci.*, 2020, **11**, 13129–13136.
106 A. Brandenburg, D. S. Krylov, A. Beger, A. U. B. Wolter, B. Buchner and A. A. Popov, *Chem. Commun.*, 2018, **54**, 10683–10686.
107 K. Junghans, C. Schlesier, A. Kostanyan, N. A. Samoylova, Q. Deng, M. Rosenkranz, S. Schiemenz, R. Westerstrom, T. Greber, B. Buchner and A. A. Popov, *Angew. Chem., Int. Ed.*, 2015, **54**, 13411–13415.
108 A. L. Svitova, Y. Krupskaya, N. Samoylova, R. Kraus, J. Geck, L. Dunsch and A. A. Popov, *Dalton Trans.*, 2014, **43**, 7387–7390.
109 M. Wolf, K. H. Muller, Y. Skourski, D. Eckert, P. Georgi, M. Krause and L. Dunsch, *Angew. Chem., Int. Ed.*, 2005, **44**, 3306–3309.
110 B. Náfrádi, Á. Antal, Á. Pásztor, L. Forró, L. F. Kiss, T. Fehér, É. Kováts, S. Pekker and A. Jánossy, *J. Phys. Chem. Lett.*, 2012, **3**, 3291–3296.
111 Z. Hu, Y. Hao, Z. Slanina, Z. Gu, Z. Shi, F. Uhlik, Y. Zhao and L. Feng, *Inorg. Chem.*, 2015, **54**, 2103–2108.
112 L. Bao, P. Yu, Y. Li, C. Pan, W. Shen, P. Jin, S. Liang and X. Lu, *Chem. Sci.*, 2019, **10**, 4945–4950.
113 L. Bao, Y. Li, P. Yu, W. Shen, P. Jin and X. Lu, *Angew. Chem., Int. Ed.*, 2020, **59**, 5259–5262.
114 X. Lu, Z. Slanina, T. Akasaka, T. Tsuchiya, N. Mizorogi and S. Nagase, *J. Am. Chem. Soc.*, 2010, **132**, 5896–5905.
115 H. Yang, H. Jin, X. Wang, Z. Liu, M. Yu, F. Zhao, B. Q. Mercado, M. M. Olmstead and A. L. Balch, *J. Am. Chem. Soc.*, 2012, **134**, 14127–14136.
116 F. Liu, S. Wang, J. Guan, T. Wei, M. Zeng and S. Yang, *Inorg. Chem.*, 2014, **53**, 5201–5205.
117 W. Shen, Z. Hu, P. Yu, Z. Wei, P. Jin, Z. Shi and X. Lu, *Inorg. Chem. Front.*, 2020, **7**, 4563–4571.
118 R. Guan, M. Chen, J. Xin, X.-M. Xie, F. Jin, Q. Zhang, S.-Y. Xie and S. Yang, *J. Am. Chem. Soc.*, 2021, **143**, 8078–8085.
119 F. Jin, S. Wang, S. Yang, N. B. Tamm, I. N. Ioffe and S. I. Troyanov, *Inorg. Chem.*, 2016, **55**, 12523–12526.
120 F. Jin, S. Wang, N. B. Tamm, S. Yang and S. I. Troyanov, *Angew. Chem., Int. Ed.*, 2017, **129**, 12152–12156.
121 S. Stevenson, M. A. Mackey, M. A. Stuart, J. P. Phillips, M. L. Easterling, C. J. Chancellor, M. M. Olmstead and A. L. Balch, *J. Am. Chem. Soc.*, 2008, **130**, 11844–11845.
122 B. Q. Mercado, M. M. Olmstead, C. M. Beavers, M. L. Easterling, S. Stevenson, M. A. Mackey, C. E. Coumbe, J. D. Phillips, J. P. Phillips, J. M. Poblet and A. L. Balch, *Chem. Commun.*, 2010, **46**, 279–281.
123 L. Feng, Y. Hao, A. Liu and Z. Slanina, *Acc. Chem. Res.*, 2019, **52**, 1802–1811.
124 M. Zhang, Y. Hao, X. Li, L. Feng, T. Yang, Y. Wan, N. Chen, Z. Slanina, F. Uhlík and H. Cong, *J. Phys. Chem. C*, 2014, **118**, 28883–28889.
125 Q. Tang, L. Abella, Y. Hao, X. Li, Y. Wan, A. Rodriguez-Fortea, J. M. Poblet, L. Feng and N. Chen, *Inorg. Chem.*, 2015, **54**, 9845–9852.
126 T. Yang, Y. Hao, L. Abella, Q. Tang, X. Li, Y. Wan, A. Rodríguez-Fortea, J. M. Poblet, L. Feng and N. Chen, *Chem. – Eur. J.*, 2015, **21**, 11110–11117.
127 Y. Hao, Q. Tang, X. Li, M. Zhang, Y. Wan, L. Feng, N. Chen, Z. Slanina, L. Adamowicz and F. Uhlík, *Inorg. Chem.*, 2016, **55**, 11354–11361.
128 L. Feng, M. Zhang, Y. Hao, Q. Tang, N. Chen, Z. Slanina and F. Uhlík, *Dalton Trans.*, 2016, **45**, 8142–8148.

129 Q. Tang, L. Abella, Y. Hao, X. Li, Y. Wan, A. Rodriguez-Fortea, J. M. Poblet, L. Feng and N. Chen, *Inorg. Chem.*, 2016, **55**, 1926–1933.
130 P. Yu, M. Li, W. Shen, S. Hu, P.-Y. Yu, X. Tian, X. Zhao, L. Bao and X. Lu, *Inorg. Chem. Front.*, 2022, **9**, 2264–2270.
131 P. Yu, H. Mei, S. Hu, C. Pan, W. Shen, P. Yu, K. Guo, Y. Xie, T. Akasaka and L. Bao, *Chin. J. Chem.*, 2023, **41**, 1915–1920.
132 H. Cong, A. Liu, Y. Hao, L. Feng, Z. Slanina and F. Uhlik, *Inorg. Chem.*, 2019, **58**, 10905–10911.
133 J. C. Duchamp, H. C. Dorn, A. L. Wysocki, K. Park, M. M. Olmstead, M. Roy and A. L. Balch, *Inorg. Chem.*, 2023, **62**, 5114–5122.
134 A. Liu, M. Nie, Y. Hao, Y. Yang, T. Wang, Z. Slanina, H. Cong, L. Feng, C. Wang and F. Uhlik, *Inorg. Chem.*, 2019, **58**, 4774–4781.
135 P. Yu, M. Li, S. Hu, C. Pan, W. Shen, G. Kun, Y.-P. Xie, L. Bao, R. Zhang and X. Lu, *Chem. Commun.*, 2023, **59**, 12990–12993.
136 M. K. Singh and G. Rajaraman, *Chem. Commun.*, 2016, **52**, 14047–14050.
137 J. Xiong, H.-Y. Ding, Y.-S. Meng, C. Gao, X.-J. Zhang, Z.-S. Meng, Y.-Q. Zhang, W. Shi, B.-W. Wang and S. Gao, *Chem. Sci.*, 2017, **8**, 1288–1294.
138 J. Wang, Q. W. Li, S. G. Wu, Y. C. Chen, R. C. Wan, G. Z. Huang, Y. Liu, J. L. Liu, D. Reta and M. J. Giansiracusa, *Angew. Chem., Int. Ed.*, 2021, **60**, 5299–5306.
139 P. H. Lin, T. J. Burchell, R. Clérac and M. Murugesu, *Angew. Chem., Int. Ed.*, 2008, **47**, 8848–8851.
140 Y.-N. Guo, G.-F. Xu, W. Wernsdorfer, L. Ungur, Y. Guo, J. Tang, H.-J. Zhang, L. F. Chibotaru and A. K. Powell, *J. Am. Chem. Soc.*, 2011, **133**, 11948–11951.
141 J. Long, F. Habib, P.-H. Lin, I. Korobkov, G. Enright, L. Ungur, W. Wernsdorfer, L. F. Chibotaru and M. Murugesu, *J. Am. Chem. Soc.*, 2011, **133**, 5319–5328.
142 E. Moreno Pineda, N. F. Chilton, R. Marx, M. Dorfel, D. O. Sells, P. Neugebauer, S. D. Jiang, D. Collison, J. van Slageren, E. J. McInnes and R. E. Winpenny, *Nat. Commun.*, 2014, **5**, 5243.
143 X.-Q. Ji, F. Ma, J. Xiong, J. Yang, H.-L. Sun, Y.-Q. Zhang and S. Gao, *Inorg. Chem. Front.*, 2019, **6**, 786–790.
144 C. Y. Chow, H. Bolvin, V. E. Campbell, R. Guillot, J. W. Kampf, W. Wernsdorfer, F. Gendron, J. Autschbach, V. L. Pecoraro and T. Mallah, *Chem. Sci.*, 2015, **6**, 4148–4159.
145 P. Zhang, F. Benner, N. F. Chilton and S. Demir, *Chem*, 2022, **8**, 717–730.
146 L. Dunsch, S. F. Yang, L. Zhang, A. Svitova, S. Oswald and A. A. Popov, *J. Am. Chem. Soc.*, 2010, **132**, 5413–5421.
147 N. Chen, M. N. Chaur, C. Moore, J. R. Pinzon, R. Valencia, A. Rodriguez-Fortea, J. M. Poblet and L. Echegoyen, *Chem. Commun.*, 2010, **46**, 4818–4820.
148 B. Q. Mercado, N. Chen, A. Rodríguez-Fortea, M. A. Mackey, S. Stevenson, L. Echegoyen, J. M. Poblet, M. M. Olmstead and A. L. Balch, *J. Am. Chem. Soc.*, 2011, **133**, 6752–6760.
149 N. Chen, C. M. Beavers, M. Mulet-Gas, A. Rodriguez-Fortea, E. J. Munoz, Y. Y. Li, M. M. Olmstead, A. L. Balch, J. M. Poblet and L. Echegoyen, *J. Am. Chem. Soc.*, 2012, **134**, 7851–7860.
150 N. Chen, M. Mulet-Gas, Y.-Y. Li, R. E. Stene, C. W. Atherton, A. Rodríguez-Fortea, J. M. Poblet and L. Echegoyen, *Chem. Sci.*, 2013, **4**, 180–186.
151 N. A. Samoylova, S. M. Avdoshenko, D. S. Krylov, H. R. Thompson, A. C. Kirkhorn, M. Rosenkranz, S. Schiemenz, F. Ziegs, A. U. B. Wolter, S. Yang, S. Stevenson and A. A. Popov, *Nanoscale*, 2017, **9**, 7977–7990.
152 F.-F. Li, N. Chen, M. Mulet-Gas, V. Triana, J. Murillo, A. Rodríguez-Fortea, J. M. Poblet and L. Echegoyen, *Chem. Sci.*, 2013, **4**, 3404.
153 W. Cao, C. Gao, Y.-Q. Zhang, D. Qi, T. Liu, K. Wang, C. Duan, S. Gao and J. Jiang, *Chem. Sci.*, 2015, **6**, 5947–5954.
154 F. Tuna, C. A. Smith, M. Bodensteiner, L. Ungur, L. F. Chibotaru, E. J. McInnes, R. E. Winpenny, D. Collison and R. A. Layfield, *Angew. Chem., Int. Ed.*, 2012, **51**, 6976–6980.
155 S.-S. Liu, K. Lang, Y.-Q. Zhang, Q. Yang, B.-W. Wang and S. Gao, *Dalton Trans.*, 2016, **45**, 8149–8153.
156 X. Lu, T. Akasaka and S. Nagase, *Acc. Chem. Res.*, 2013, **46**, 1627–1635.
157 Z. Q. Shi, X. Wu, C. R. Wang, X. Lu and H. Shinohara, *Angew. Chem., Int. Ed.*, 2006, **45**, 2107–2111.
158 J. Zhang, F. L. Bowles, D. W. Bearden, W. K. Ray, T. Fuhrer, Y. Ye, C. Dixon, K. Harich, R. F. Helm, M. M. Olmstead, A. L. Balch and H. C. Dorn, *Nat. Chem.*, 2013, **5**, 880–885.
159 S. Zhao, P. Zhao, W. Cai, L. Bao, M. Chen, Y. Xie, X. Zhao and X. Lu, *J. Am. Chem. Soc.*, 2017, **139**, 4724–4728.
160 C. R. Wang, T. Kai, T. Tomiyama, T. Yoshida, Y. Kobayashi, E. Nishibori, M. Takata, M. Sakata and H. Shinohara, *Angew. Chem., Int. Ed.*, 2001, **40**, 397–399.
161 J. Zhang, T. Fuhrer, W. Fu, J. Ge, D. W. Bearden, J. Dallas, J. Duchamp, K. Walker, H. Champion, H. Azurmendi, K. Harich and H. C. Dorn, *J. Am. Chem. Soc.*, 2012, **134**, 8487–8493.
162 A. L. Svitova, K. B. Ghiassi, C. Schlesier, K. Junghans, Y. Zhang, M. M. Olmstead, A. L. Balch, L. Dunsch and A. A. Popov, *Nat. Commun.*, 2014, **5**, 3568.
163 F. Jin, J. Xin, R. Guan, X.-M. Xie, M. Chen, Q. Zhang, A. A. Popov, S.-Y. Xie and S. Yang, *Chem. Sci.*, 2021, **12**, 6890–6895.
164 S. Hu, P. Zhao, B. Li, P. Yu, L. Yang, M. Ehara, P. Jin, T. Akasaka and X. Lu, *Inorg. Chem.*, 2022, **61**, 11277–11283.
165 H. Fang, H. Cong, M. Suzuki, L. Bao, B. Yu, Y. Xie, N. Mizorogi, M. M. Olmstead, A. L. Balch and S. Nagase, *J. Am. Chem. Soc.*, 2014, **136**, 10534–10540.
166 K. Tan and X. Lu, *J. Phys. Chem. A*, 2006, **110**, 1171–1176.
167 Y. Iiduka, T. Wakahara, T. Nakahodo, T. Tsuchiya, A. Sakuraba, Y. Maeda, T. Akasaka, K. Yoza, E. Horn and T. Kato, *J. Am. Chem. Soc.*, 2005, **127**, 12500–12501.
168 K. R. McClain, H. Kwon, K. Chakarawet, R. Nabi, J. G. Kragskow, N. F. Chilton, R. D. Britt, J. R. Long and B. G. Harvey, *J. Am. Chem. Soc.*, 2023, **145**, 8996–9002.
169 H. Funasaka, K. Sakurai, Y. Oda, K. Yamamoto and T. Takahashi, *Chem. Phys. Lett.*, 1995, **232**, 273–277.

170 H. Funasaka, K. Sugiyama, K. Yamamoto and T. Takahashi, *J. Phys. Chem.*, 1995, **99**, 1826–1830.
171 K. Furukawa, S. Okubo, H. Kato, H. Shinohara and T. Kato, *J. Phys. Chem. A*, 2003, **107**, 10933–10937.
172 H. Huang, S. Yang and X. Zhang, *J. Phys. Chem. B*, 1999, **103**, 5928–5932.
173 H. Huang, S. Yang and X. Zhang, *J. Phys. Chem. B*, 2000, **104**, 1473–1482.
174 L. Bao, C. Pan, Z. Slanina, F. Uhlik, T. Akasaka and X. Lu, *Angew. Chem., Int. Ed.*, 2016, **55**, 9234–9238.
175 F. Donati, S. Rusponi, S. Stepanow, C. Wäckerlin, A. Singha, L. Persichetti, R. Baltic, K. Diller, F. Patthey, E. Fernandes, J. Dreiser, Ž. Šljivančanin, K. Kummer, C. Nistor, P. Gambardella and H. Brune, *Science*, 2016, **352**, 318–321.
176 F. Donati, S. Rusponi, S. Stepanow, L. Persichetti, A. Singha, D. M. Juraschek, C. Wäckerlin, R. Baltic, M. Pivetta, K. Diller, C. Nistor, J. Dreiser, K. Kummer, E. Velez-Fort, N. A. Spaldin, H. Brune and P. Gambardella, *Phys. Rev. Lett.*, 2020, **124**, 077204.
177 R. Baltic, M. Pivetta, F. Donati, C. Wäckerlin, A. Singha, J. Dreiser, S. Rusponi and H. Brune, *Nano Lett.*, 2016, **16**, 7610–7615.
178 H. Matsuoka, N. Ozawa, T. Kodama, H. Nishikawa, I. Ikemoto, K. Kikuchi, K. Furukawa, K. Sato, D. Shiomi, T. Takui and T. Kato, *J. Phys. Chem. B*, 2004, **108**, 13972–13976.
179 W. Xu, B. Niu, L. Feng, Z. Shi and Y. Lian, *Chem. – Eur. J.*, 2012, **18**, 14246–14249.
180 W. Xu, B. Niu, Z. Shi, Y. Lian and L. Feng, *Nanoscale*, 2012, **4**, 6876–6879.
181 Z. Wang, Y. Nakanishi, S. Noda, H. Niwa, J. Zhang, R. Kitaura and H. Shinohara, *Angew. Chem., Int. Ed.*, 2013, **52**, 11770–11774.
182 Z. Wang, S. Aoyagi, H. Omachi, R. Kitaura and H. Shinohara, *Angew. Chem., Int. Ed.*, 2016, **55**, 199–202.
183 H. Nikawa, T. Kikuchi, T. Wakahara, T. Nakahodo, T. Tsuchiya, G. A. Rahman, T. Akasaka, Y. Maeda, K. Yoza and E. Horn, *J. Am. Chem. Soc.*, 2005, **127**, 9684–9685.
184 D. Xu, Y. Jiang, Y. Wang, T. Zhou, Z. Shi, H. Omachi, H. Shinohara, B. Sun and Z. Wang, *Inorg. Chem.*, 2019, **58**, 14325–14330.
185 H. Nikawa, T. Yamada, B. Cao, N. Mizorogi, Z. Slanina, T. Tsuchiya, T. Akasaka, K. Yoza and S. Nagase, *J. Am. Chem. Soc.*, 2009, **131**, 10950–10954.
186 X. Han, J. Xin, Y. Yao, Z. Liang, Y. Qiu, M. Chen and S. Yang, *Nanomaterials*, 2022, **12**, 3291.
187 Y. Takano, A. Yomogida, H. Nikawa, M. Yamada, T. Wakahara, T. Tsuchiya, M. O. Ishitsuka, Y. Maeda, T. Akasaka and T. Kato, *J. Am. Chem. Soc.*, 2008, **130**, 16224–16230.
188 L. Feng, T. Nakahodo, T. Wakahara, T. Tsuchiya, Y. Maeda, T. Akasaka, T. Kato, E. Horn, K. Yoza and N. Mizorogi, *J. Am. Chem. Soc.*, 2005, **127**, 17136–17137.
189 H. Huang, L. Zhang, X. J. Gao, X. Guo, R. Cui, B. Xu, J. Dong, Y. Li, L. Gan and F. Chang, *Chem. Mater.*, 2018, **30**, 64–68.
190 J. C. Hummelen, B. Knight, J. Pavlovich, R. González and F. Wudl, *Science*, 1995, **269**, 1554–1556.
191 T. Akasaka, S. Okubo, T. Wakahara, K. Yamamoto, K. Kobayashi, S. Nagase, T. Kato, M. Kako, Y. Nakadaira and Y. Kitayama, *Chem. Lett.*, 1999, 945–946.
192 M. Briganti, E. Lucaccini, L. Chelazzi, S. Ciattini, L. Sorace, R. Sessoli, F. Totti and M. Perfetti, *J. Am. Chem. Soc.*, 2021, **143**, 8108–8115.
193 C. A. Gould, K. R. McClain, J. M. Yu, T. J. Groshens, F. Furche, B. G. Harvey and J. R. Long, *J. Am. Chem. Soc.*, 2019, **141**, 12967–12973.
194 J. C. Vanjak, B. O. Wilkins, V. Vieru, N. S. Bhuvanesh, J. H. Reibenspies, C. D. Martin, L. F. Chibotaru and M. Nippe, *J. Am. Chem. Soc.*, 2022, **144**, 17743–17747.
195 C. A. P. Goodwin, F. Ortu, D. Reta, N. F. Chilton and D. P. Mills, *Nature*, 2017, **548**, 439–442.
196 E. Moreno-Pineda, M. Damjanović, O. Fuhr, W. Wernsdorfer and M. Ruben, *Angew. Chem., Int. Ed.*, 2017, **56**, 9915–9919.
197 S.-G. Wu, Z.-Y. Ruan, G.-Z. Huang, J.-Y. Zheng, V. Vieru, G. Taran, J. Wang, Y.-C. Chen, J.-L. Liu and L. F. Chibotaru, *Chem*, 2021, **7**, 982–992.
198 J. D. Rinehart, M. Fang, W. J. Evans and J. R. Long, *Nat. Chem.*, 2011, **3**, 538–542.
199 S. Demir, M. I. Gonzalez, L. E. Darago, W. J. Evans and J. R. Long, *Nat. Commun.*, 2017, **8**, 2144.
200 J. D. Rinehart, M. Fang, W. J. Evans and J. R. Long, *J. Am. Chem. Soc.*, 2011, **133**, 14236–14239.
201 L. E. Darago, M. D. Boshart, B. D. Nguyen, E. Perlt, J. W. Ziller, W. W. Lukens, F. Furche, W. J. Evans and J. R. Long, *J. Am. Chem. Soc.*, 2021, **143**, 8465–8475.
202 C. A. Gould, E. Mu, V. Vieru, L. E. Darago, K. Chakarawet, M. I. Gonzalez, S. Demir and J. R. Long, *J. Am. Chem. Soc.*, 2020, **142**, 21197–21209.
203 A. A. Popov, S. M. Avdoshenko, A. M. Pendas and L. Dunsch, *Chem. Commun.*, 2012, **48**, 8031–8050.
204 W. Shen, L. Bao, Y. Wu, C. Pan, S. Zhao, H. Fang, Y. Xie, P. Jin, P. Peng, F.-F. Li and X. Lu, *J. Am. Chem. Soc.*, 2017, **139**, 9979–9984.
205 S. Hu, W. Shen, L. Yang, G. Duan, P. Jin, Y. Xie, T. Akasaka and X. Lu, *Chem. – Eur. J.*, 2019, **25**, 11538–11544.
206 Z. Wang, R. Kitaura and H. Shinohara, *J. Phys. Chem. C*, 2014, **118**, 13953–13958.
207 Y. Jiang, Z. Li, J. Zhang and Z. Wang, *J. Phys. Chem. C*, 2019, **124**, 2131–2136.
208 W. J. Evans, M. Fang, G. Zucchi, F. Furche, J. W. Ziller, R. M. Hoekstra and J. I. Zink, *J. Am. Chem. Soc.*, 2009, **131**, 11195–11202.
209 A. Mansikkamäki, A. A. Popov, Q. Deng, N. Iwahara and L. F. Chibotaru, *J. Chem. Phys.*, 2017, **147**, 124305.
210 T. Tsuchiya, M. Wielopolski, N. Sakuma, N. Mizorogi, T. Akasaka, T. Kato, D. M. Guldi and S. Nagase, *J. Am. Chem. Soc.*, 2011, **133**, 13280–13283.
211 L. Feng, S. G. Radhakrishnan, N. Mizorogi, Z. Slanina, H. Nikawa, T. Tsuchiya, T. Akasaka, S. Nagase, N. Martin and D. M. Guldi, *J. Am. Chem. Soc.*, 2011, **133**, 7608–7618.
212 M. Yamada, H. Kurihara, M. Suzuki, M. Saito, Z. Slanina, F. Uhlik, T. Aizawa, T. Kato, M. M. Olmstead, A. L. Balch,

Y. Maeda, S. Nagase, X. Lu and T. Akasaka, *J. Am. Chem. Soc.*, 2015, **137**, 232–238.
213 L. Bao, M. Chen, C. Pan, T. Yamaguchi, T. Kato, M. M. Olmstead, A. L. Balch, T. Akasaka and X. Lu, *Angew. Chem., Int. Ed.*, 2016, **55**, 4242–4246.
214 M. K. Singh, N. Yadav and G. Rajaraman, *Chem. Commun.*, 2015, **51**, 17732–17735.
215 R. B. Zaripov, Y. E. Kandrashkin, K. M. Salikhov, B. Büchner, F. Liu, M. Rosenkranz, A. A. Popov and V. Kataev, *Nanoscale*, 2020, **12**, 20513–20521.
216 Y. E. Kandrashkin, R. B. Zaripov, F. Liu, B. Büchner, V. Kataev and A. A. Popov, *Phys. Chem. Chem. Phys.*, 2021, **23**, 18206–18220.
217 W. Yang, G. Velkos, M. Rosenkranz, S. Schiemenz, F. Liu and A. A. Popov, *Adv. Sci.*, 2023, 2305190.
218 G. Velkos, D. S. Krylov, K. Kirkpatrick, X. Liu, L. Spree, A. U. B. Wolter, B. Buchner, H. C. Dorn and A. A. Popov, *Chem. Commun.*, 2018, **54**, 2902–2905.
219 M. J. Martinez-Perez, S. Cardona-Serra, C. Schlegel, F. Moro, P. J. Alonso, H. Prima-Garcia, J. M. Clemente-Juan, M. Evangelisti, A. Gaita-Arino, J. Sese, J. van Slageren, E. Coronado and F. Luis, *Phys. Rev. Lett.*, 2012, **108**, 247213.
220 M. D. Jenkins, Y. Duan, B. Diosdado, J. J. García-Ripoll, A. Gaita-Ariño, C. Giménez-Saiz, P. J. Alonso, E. Coronado and F. Luis, *Phys. Rev. B*, 2017, **95**, 064423.
221 J. Lopez-Cabrelles, L. Escalera-Moreno, Z. Hu, H. Prima-Garcia, G. M. Espallargas, A. Gaita-Arino and E. Coronado, *Inorg. Chem.*, 2021, **60**, 8575–8580.
222 F. Luis, P. J. Alonso, O. Roubeau, V. Velasco, D. Zueco, D. Aguilà, J. I. Martínez, L. A. Barrios and G. Aromí, *Commun. Chem.*, 2020, **3**, 176.
223 M. N. Leuenberger and D. Loss, *Nature*, 2001, **410**, 789.
224 C. Godfrin, A. Ferhat, R. Ballou, S. Klyatskaya, M. Ruben, W. Wernsdorfer and F. Balestro, *Phys. Rev. Lett.*, 2017, **119**, 187702.
225 W. Xiang, Z. Hu, J. Xin, H. Jin, Z. Jiang, X. Han, M. Chen, Y.-R. Yao and S. Yang, *J. Am. Chem. Soc.*, 2023, **145**, 22599–22608.
226 M. Nie, L. Yang, C. Zhao, H. Meng, L. Feng, P. Jin, C. Wang and T. Wang, *Nanoscale*, 2019, **11**, 18612–18618.
227 A. Moreno-Vicente, Y. Roselló, N. Chen, L. Echegoyen, P. W. Dunk, A. Rodríguez-Fortea, C. de Graaf and J. M. Poblet, *J. Am. Chem. Soc.*, 2023, **145**, 6710–6718.
228 X. Zhang, Y. Wang, R. Morales-Martinez, J. Zhong, C. de Graaf, A. Rodriguez-Fortea, J. M. Poblet, L. Echegoyen, L. Feng and N. Chen, *J. Am. Chem. Soc.*, 2018, **140**, 3907–3915.
229 S. Dey and G. Rajaraman, *Chem. Sci.*, 2021, **12**, 14207–14216.
230 K. Suenaga, M. Tence, C. Mory, C. Colliex, H. Kato, T. Okazaki, H. Shinohara, K. Hirahara, S. Bandow and S. Iijima, *Science*, 2000, **290**, 2280–2282.
231 K. Hirahara, K. Suenaga, S. Bandow, H. Kato, T. Okazaki, H. Shinohara and S. Iijima, *Phys. Rev. Lett.*, 2000, **85**, 5384.
232 L. Guan, K. Suenaga, S. Okubo, T. Okazaki and S. Iijima, *J. Am. Chem. Soc.*, 2008, **130**, 2162–2163.
233 M. Urdampilleta, S. Klyatskaya, J.-P. Cleuziou, M. Ruben and W. Wernsdorfer, *Nat. Mater.*, 2011, **10**, 502–506.
234 K. Katoh, S. Yamashita, N. Yasuda, Y. Kitagawa, B. K. Breedlove, Y. Nakazawa and M. Yamashita, *Angew. Chem., Int. Ed.*, 2018, **57**, 9262–9267.
235 C. Gimenez-Lopez Mdel, F. Moro, A. La Torre, C. J. Gomez-Garcia, P. D. Brown, J. van Slageren and A. N. Khlobystov, *Nat. Commun.*, 2011, **2**, 407.
236 R. Nakanishi, J. Satoh, K. Katoh, H. Zhang, B. K. Breedlove, M. Nishijima, Y. Nakanishi, H. Omachi, H. Shinohara and M. Yamashita, *J. Am. Chem. Soc.*, 2018, **140**, 10955–10959.
237 S. M. Avdoshenko, F. Fritz, C. Schlesier, A. Kostanyan, J. Dreiser, M. Luysberg, A. A. Popov, C. Meyer and R. Westerström, *Nanoscale*, 2018, **10**, 18153–18160.
238 N. Domingo, E. Bellido and D. Ruiz-Molina, *Chem. Soc. Rev.*, 2012, **41**, 258–302.
239 A. Cornia, M. Mannini, P. Sainctavit and R. Sessoli, *Chem. Soc. Rev.*, 2011, **40**, 3076–3091.
240 R. J. Holmberg and M. Murugesu, *J. Mater. Chem. C*, 2015, **3**, 11986–11998.
241 M. Clemente-León, H. Soyer, E. Coronado, C. Mingotaud, C. J. Gómez-García and P. Delhaès, *Angew. Chem., Int. Ed.*, 1998, **37**, 2842–2845.
242 M. Mannini, F. Pineider, P. Sainctavit, C. Danieli, E. Otero, C. Sciancalepore, A. M. Talarico, M.-A. Arrio, A. Cornia and D. Gatteschi, *Nat. Mater.*, 2009, **8**, 194–197.
243 G. Serrano, L. Poggini, M. Briganti, A. L. Sorrentino, G. Cucinotta, L. Malavolti, B. Cortigiani, E. Otero, P. Sainctavit and S. Loth, *Nat. Mater.*, 2020, **19**, 546–551.
244 M. Mannini, F. Pineider, C. Danieli, F. Totti, L. Sorace, P. Sainctavit, M.-A. Arrio, E. Otero, L. Joly and J. C. Cezar, *Nature*, 2010, **468**, 417–421.
245 L. Margheriti, D. Chiappe, M. Mannini, P. E. Car, P. Sainctavit, M. A. Arrio, F. B. de Mongeot, J. C. Cezar, F. M. Piras and A. Magnani, *Adv. Mater.*, 2010, **22**, 5488–5493.
246 C. Wäckerlin, F. Donati, A. Singha, R. Baltic, S. Rusponi, K. Diller, F. Patthey, M. Pivetta, Y. Lan and S. Klyatskaya, *Adv. Mater.*, 2016, **28**, 5195–5199.
247 C. F. Hermanns, M. Bernien, A. Krüger, C. Schmidt, S. T. Waßerroth, G. Ahmadi, B. W. Heinrich, M. Schneider, P. W. Brouwer and K. J. Franke, *Phys. Rev. Lett.*, 2013, **111**, 167203.
248 D. S. Krylov, S. Schimmel, V. Dubrovin, F. Liu, T. T. N. Nguyen, L. Spree, C. H. Chen, G. Velkos, C. Bulbucan, R. Westerstrom, M. Studniarek, J. Dreiser, C. Hess, B. Buchner, S. M. Avdoshenko and A. A. Popov, *Angew. Chem., Int. Ed.*, 2020, **59**, 5756–5764.
249 C. H. Chen, D. S. Krylov, S. M. Avdoshenko, F. Liu, L. Spree, R. Westerstrom, C. Bulbucan, M. Studniarek, J. Dreiser, A. U. B. Wolter, B. Buchner and A. A. Popov, *Nanoscale*, 2018, **10**, 11287–11292.
250 R. Westerstrom, A. C. Uldry, R. Stania, J. Dreiser, C. Piamonteze, M. Muntwiler, F. Matsui, S. Rusponi, H. Brune, S. Yang, A. Popov, B. Buchner, B. Delley and T. Greber, *Phys. Rev. Lett.*, 2015, **114**, 087201.

251 T. Greber, A. P. Seitsonen, A. Hemmi, J. Dreiser, R. Stania, F. Matsui, M. Muntwiler, A. Popov and R. Westerström, *Phys. Rev. Mater.*, 2019, **3**, 014409.
252 R. Sagehashi, W. C. Lee, F. Liu, A. A. Popov, M. Muntwiler, B. Delley, P. Krüger and T. Greber, *Phys. Rev. Mater.*, 2023, **7**, 086001.
253 C. H. Chen, L. Spree, E. Koutsouflakis, D. S. Krylov, F. Liu, A. Brandenburg, G. Velkos, S. Schimmel, S. M. Avdoshenko and A. Fedorov, *Adv. Sci.*, 2021, **8**, 2000777.
254 F. Paschke, T. Birk, S. M. Avdoshenko, F. Liu, A. A. Popov and M. Fonin, *Small*, 2022, **18**, 2105667.
255 G. M. Espallargas and E. Coronado, *Chem. Soc. Rev.*, 2018, **47**, 533–557.
256 D. Aulakh, J. B. Pyser, X. Zhang, A. A. Yakovenko, K. R. Dunbar and M. Wriedt, *J. Am. Chem. Soc.*, 2015, **137**, 9254–9257.
257 Y. Feng, T. Wang, Y. Li, J. Li, J. Wu, B. Wu, L. Jiang and C. Wang, *J. Am. Chem. Soc.*, 2015, **137**, 15055–15060.
258 H. Meng, C. Zhao, M. Nie, C. Wang and T. Wang, *J. Phys. Chem. C*, 2019, **123**, 6265–6269.
259 J. Zhang, L. Liu, C. Zheng, W. Li, C. Wang and T. Wang, *Nat. Commun.*, 2023, **14**, 4922.
260 Y. Li, T. Wang, H. Meng, C. Zhao, M. Nie, L. Jiang and C. Wang, *Dalton Trans.*, 2016, **45**, 19226–19229.
261 H. Meng, C. Zhao, M. Nie, C. Wang and T. Wang, *ACS Appl. Mater. Interfaces*, 2018, **10**, 32607–32612.